

**Machine-Learning and Design of Experiments-based  
Optimization of Organic Solar Cells**

by

Aaron Kirkey

A thesis submitted in partial fulfillment of the requirements for the degree of

**Master of Science**

Department of Chemistry

**University of Alberta**

# Abstract

Over the coming decades, global population and energy consumption are projected to increase dramatically, with the latter doubling by 2050 as per the most conservative estimates. Much of this demand is likely to be met with increased use of fossil fuels. The burning of fossil fuels is a major contributor to the ever-increasing CO<sub>2</sub> concentration in the atmosphere, a major driver of climate change. In order for countries and companies to meet their climate targets, they must undergo a transition to low or CO<sub>2</sub>-free energy sources (wind, solar, hydroelectric, for example). Solar power, typically harvested using photovoltaic and solar thermal devices, is considered one of the most promising renewable energy technologies due to the sheer quantity of solar irradiation impinging upon terrestrial earth. Organic photovoltaics (OPVs) are a subset of PV technology that are thin, lightweight, printable using roll-to-roll and spray coating technologies, flexible, and can be made semi-transparent. These features enable this class of photovoltaics to be considered in markets and locales otherwise inaccessible to traditional silicon devices, which are heavy and cumbersome. Organic photovoltaics comprise many layers that need to be manufactured with great care in order to yield devices capable of producing substantial power, in a reproducible fashion. The central layer in this stack is the critical light absorbing layer that consists of two or three, and occasionally more, different organic molecules.

The work described within this dissertation looks at the application of Design of Experiments (DOE) and machine learning (ML) for optimizing OPV device bulk heterojunctions (BHJs) that are based on small-molecule components. Typically in an academic setting, researchers are directed to optimize any given system via a one-variable-at-a-time (OVAT) approach in order to discern the effect of that one variable on the desired output. However, given the complexity and number of variables in the manufacturing of OPV devices, this approach is often too lengthy and expensive to implement robustly across more than a couple of variables. In addition, the variables are typically co-dependent, interrelated, and convoluted, and thus independent optimization of each variable is not possible, resulting in unsatisfactory optimization. In addition to the design of experiments (DOE), we then apply machine learning (ML) methods to further optimize device manufacturing processing parameters to provide the equivalent of a topological map that aids researchers in determining the best next steps for arriving at optimum performance. DOE is a sampling method that reduces the number of experiments required to investigate a large parameter space. As a result, wider ranges or more variables can be investigated simultaneously. With experimental data derived from DOE, the ML approach is used to interpolate device efficiencies across the entire parameter space investigated. The combination of DOE and ML enables the identification of the values that truly matter with respect to arriving at the highest efficiency devices, with a fraction of the material and time required via OVAT optimization.

# Preface

Chapter 1 serves as an introduction to photovoltaics, their place relative to other energy technologies and an explanation of organic photovoltaics in particular.

Chapter 2 is based on a manuscript titled “Bulk-heterojunction Optimization of All Small-molecule Organic Photovoltaic Devices Using Design of Experiment and Machine Learning Approaches” authored by Aaron Kirkey, Erik J. Lubber, Brian C. Olsen and Jillian M. Buriak. I carried out the manufacturing, testing and characterization of the photovoltaic devices. Erik Lubber aided with the analysis of the results obtained and formulating working theories of systems investigated. Erik Lubber and Brian C. Olsen oversaw the use of the optimization method with Brian C. Olsen wrote the code required to implement the machine learning algorithm. Jillian M. Buriak and Erik J. Lubber helped prepare and edit the manuscript and Jillian M. Buriak supervised the entire project.

Chapter 3 will conclude the findings from Chapter 2 and propose future directions and projects stemming from this work.

# Acknowledgements

I would firstly like to thank the group members from the Buriak research group for always being inspiring, kind and fantastic to talk to. They helped me on a wide range of topics both professional and personal and I'll remember my time spent with them all fondly. I would like to thank Dr. Jillian Buriak for always being honest and candid with her support, supervision and advice throughout my degree. She was integral in helping me develop confidence in professional settings and a stepping stone identifying a career wherever I may end up. She is a role model of how a professor should interact with their students. I would like to thank Dr. Erik Luber and Brian Olsen for always welcoming drop-in meetings to talk about all things science related. Without them I would have struggled to understand aspects of this work that were integral. Beyond that, they make great friends. I would like to thank Dr. Bing Cao and Tate Hauger for being maestros at what they do. Bing is a wealth of knowledge with regards to the fabrication of organic solar cells. She taught me so much and I'm glad to have been her student! Tate Hauger has never met a lab instrument he couldn't fix. Tate was also incredibly knowledgeable of organic photovoltaic manufacturing. I would like to thank Future Energy Systems, NSERC and Alberta Innovates for their generous funding. I would like to thank the Alberta/Technical University of Munich International Graduate School for Hybrid Functional Materials (ATUMS) program and MITACS for funding that enabled

my exchange at the Technical University of Munich. I would like to thank the Chemistry Graduate Student Society and the University of Alberta for opportunities to grow and meet wonderful people. Last and most importantly, I would like to thank my family and especially my mother for their constant never-ending support and encouragement.

# Contents

<b>1</b>	<b>Introduction</b>	<b>1</b>
1.1	Overview . . . . .	1
1.2	The Case for Photovoltaics . . . . .	2
1.3	Organic Photovoltaics . . . . .	4
1.4	Working Principles of a Solar Cell . . . . .	6
1.5	Organic Solar Cell Architecture . . . . .	8
1.6	Bulk Heterojunction Components . . . . .	10
1.7	Design of Experiments . . . . .	13
<b>2</b>	<b>Optimization of OPV device bulk heterojunctions</b>	<b>15</b>
2.1	DRCN5T/ITIC-based BHJs . . . . .	18
2.2	DRCN5T/IT-M-based BHJs . . . . .	24

2.3	DRCN5T/IT-4F-based BHJs . . . . .	27
2.4	Experimental . . . . .	33
2.4.1	Device Fabrication . . . . .	33
2.4.2	Characterization . . . . .	34
2.4.3	Machine learning approaches . . . . .	35
<b>3</b>	<b>Conclusion and Future Work</b>	<b>36</b>
3.1	Conclusion . . . . .	36
3.2	Future Work . . . . .	37
	<b>Bibliography</b>	<b>39</b>
<b>A</b>	<b>Appendix</b>	<b>52</b>
A.1	Explanation of the integer reduction of the GSD. . . . .	52
A.2	Additional Figures . . . . .	53

# List of Figures

1.1	Global primary energy consumption in 2018 and the projected total in 2050 in the IEA reference case, by source. IEA International Energy Outlook 2019. All rights reserved. <sup>2</sup> . . . . .	3
1.2	LCOE of renewable energy source in 2010 and 2019. Data point values and colored rectangles represent the mean price and range of prices from installations that year, respectively. Copyright © IRENA. <sup>10</sup> . . . . .	4
1.3	NREL record laboratory solar cell efficiency chart by technology type, accessed June 27, 2020 from <a href="https://www.nrel.gov/pv/cell-efficiency.html">https://www.nrel.gov/pv/cell-efficiency.html</a> . . . . .	5
1.4	Simplified equivalent circuits model of a solar cell, accessed on June 29, 2020 from <a href="https://pvpmc.sandia.gov/modeling-steps/2-dc-module-iv/diode-equivalent-circuit-models/">https://pvpmc.sandia.gov/modeling-steps/2-dc-module-iv/diode-equivalent-circuit-models/</a> , where $I_L$ is the light-generated current, $I_D$ is the current loss from recombination, $I_{sh}$ is the current loss from shunt resistance, $R_{sh}$ is the shunt resistance, $R_s$ is the series resistance, and $I$ and $V$ are the current and voltage produced by the cell. . . . .	7

1.5	Typical J-V curve for a photovoltaic device and inset shows the equation for fill factor. <sup>20</sup> . . . . .	7
1.6	a) Structure of a bilayer and a bulk heterojunction <sup>25</sup> and b) Major processes involved in current production in an OPV: 1) photoexcitation, 2) exciton diffusion, 3) exciton dissociation, 4) carrier migration and 5) charge extraction. . . . .	9
1.7	Structures of various non-fullerene acceptors that have replaced fullerene derivatives in popularity and performance. <sup>38</sup> . . . . .	11
1.8	Structures of the donor material, DRCN5T and the three acceptor materials ITIC, IT-M and IT-4F, that constitute the BHJ mixtures in this work. . . . .	12
2.1	a) Structures of the donor (DRCN5T) and acceptor molecules (ITIC, IT-M and IT-4F), b) OPV device flatband diagram aligned at vacuum level. Values for the HOMO and LUMO levels are derived from the following references: DRCN5T, <sup>67</sup> ITIC, <sup>68</sup> IT-M, <sup>69</sup> IT-4F, <sup>70</sup> and all other materials. <sup>71</sup> . . . . .	17
2.2	ANOVA plot from the first round of optimization of the BHJ comprising DRN5T/ITIC, revealing the relative contribution of each processing parameter on the resulting PCE. In the range tested, the annealing temperature has little influence on PCE. . . . .	21
2.3	ML-generated PCE maps for the first round of optimization of the DRCN5T/ITIC BHJ devices. This set of maps shows the effect of all four processing parameters on PCE, with areas of higher PCE represented by yellow, and lower by blue. . . . .	22

2.4 ML-generated PCE maps for the second round of optimization of the devices based on a BHJ composed of DRCN5T/ITIC. These maps are acquired at a higher sampling resolution in a narrower range of parameter space than the first round of optimization, shown in figure 2.3. . . . . 23

2.5 Maps of PCEs as generated *via* ML methods for the first round of optimization for the devices comprising a BHJ of composition of DRCN5T/IT-M. A fixed annealing time of 8 min reduces the dimensionality of this round of optimization to 3 processing parameters, reducing the parameter space and increasing data point density. . . . . 25

2.6 Maps of PCEs as generated *via* ML methods for the second round of optimization of DRCN5T/IT-M-based devices. An optimal annealing temperature of 160 °C was identified, leaving two processing parameters to optimize, the donor fraction and total concentration. . . . . 26

2.7 Maps of PCEs as generated *via* ML methods for the first round of optimization of the devices with BHJs comprising DRCN5T/IT-4F. This set of maps shows the effect of all 4 processing parameters on PCE, with higher areas of PCE represented by yellow, and lower by blue. . . . . 29

2.8 ML-generated PCE maps for the second round of optimization of devices with BHJs comprising DRCN5T/IT-4F BHJ. This set of maps shows the effect of all 4 processing parameters on PCE with higher PCE areas represented by yellow and lower PCE by blue. . . . . 30

2.9	JV curves of the champion devices for all 3 small-molecule donors that were investigated in this work, ITIC, IT-M, and IT-4F, with the donor DRCN5T. The experimental conditions used to fabricate these champion devices were identified after two rounds of the DOE and ML optimization for each composition. . . . .	32
A.1	Device fabrication flowchart. Care was taken to ensure the cleanliness of the substrates prior to and following deposition of all layers. As shown in the following figure, imperfections in the BHJ were often noted (BHJ on the left with slight streaking), which necessitated fabrication of duplicates. . . . .	53
A.2	BHJ films with the same concentration spin-cast onto a layer of ZnO/ITO from chloroform and from 1,2-dichlorobenzene, left and right respectively. Films cast from 1,2-dichlorobenzene show poor wettability and thus chloroform was chosen as the spin-casting solvent throughout this work. . . . .	54
A.3	Tabulation of the processing parameter levels, number of experiments at each level and list of experiments for the first and second round of optimization of the DRCN5T/ITIC BHJ blend. . . . .	55
A.4	Plots the performance of devices that were accepted (green) and rejected (red), and the standard deviation of devices and the number of devices accepted for each experimental condition for the first round of DRCN5T/ITIC BHJ blend optimization. . . . .	55
A.5	Plots showing performance of devices that were accepted (green) and rejected (red), and the standard deviation of devices and the number of devices accepted for each experimental condition for the second round of DRCN5T/ITIC BHJ blend optimization. . . . .	56

A.6	ANOVAs of the relative contribution of the processing parameters on PCE, FF, $J_{sc}$ , $V_{oc}$ , $R_{sh}$ and $R_{sr}$ for the first round of DRCN5T/ITIC BHJ blend optimization. . . . .	57
A.7	ANOVAs of the relative contribution of the processing parameters on PCE, FF, $J_{sc}$ , $V_{oc}$ , $R_{sh}$ and $R_{sr}$ for the second round of DRCN5T/ITIC BHJ blend optimization. . . . .	58
A.8	Pair plots comparing processing parameters to PCE, $J_{sc}$ , FF or $V_{oc}$ , for the first round of DRCN5T/ITIC BHJ blend optimization. . . . .	59
A.9	Pair plots comparing processing parameters to PCE, $J_{sc}$ , FF or $V_{oc}$ , for the second round of DRCN5T/ITIC BHJ blend optimization. . . . .	59
A.10	ML-generated $J_{sc}$ map for the first round of DRCN5T/ITIC BHJ blend optimization.	60
A.11	ML-generated map of FFs for the first round of DRCN5T/ITIC BHJ blend optimization. . . . .	61
A.12	ML-generated $V_{oc}$ map for the first round of DRCN5T/ITIC BHJ blend optimization.	62
A.13	ML-generated $J_{sc}$ map for the second round of DRCN5T/ITIC BHJ blend optimization. . . . .	63
A.14	ML-generated map of FFs for the second round of DRCN5T/ITIC BHJ blend optimization. . . . .	64
A.15	ML-generated $V_{oc}$ map for the second round of DRCN5T/ITIC BHJ blend optimization. . . . .	65

A.16	Tabulation of the processing parameter levels, number of experiments at each level, and list of experiments for the first and second round of DRCN5T/IT-M BHJ blend optimization. All experiments in the second round of optimization were replaced by the same experiments except with an annealing temperature of 160 °C and combined with the experiments outlined in round three. . . . .	66
A.17	Plots displaying the performance of devices that were accepted (green) and rejected (red), the standard deviation of devices and the number of devices accepted for each experimental condition for the first round of DRCN5T/IT-M BHJ blend optimization.	66
A.18	Plots displaying the performance of devices that were accepted (green) and rejected (red), the standard deviation of devices and the number of devices accepted for each experimental condition for the second round of DRCN5T/IT-M BHJ blend optimization. Experiments 2, 6 and 8 were all annealed at 200 °C and were rejected by the data filter. This round of optimization was repeated with a fixed annealing temperature of 160 °C, with some supplemental experiments. . . . .	67
A.19	Plots displaying the performance of devices that were accepted (green) and rejected (red), the standard deviation of devices and the number of devices accepted for each experimental condition for the second round of DRCN5T/IT-M BHJ blend optimization. . . . .	67
A.20	ANOVAs of the relative contribution of the processing parameters on PCE, FF, $J_{sc}$ , $V_{oc}$ , $R_{sh}$ and $R_{sr}$ for the first round of DRCN5T/IT-M BHJ blend optimization. . . .	68
A.21	ANOVAs of the relative contribution of the processing parameters on PCE, FF, $J_{sc}$ , $V_{oc}$ , $R_{sh}$ and $R_{sr}$ for the second round of DRCN5T/IT-M BHJ blend optimization. . .	69

A.22	Pair plots comparing processing parameters to PCE, $J_{sc}$ , FF or $V_{oc}$ , for the first round of DRCN5T/IT-M BHJ blend optimization. . . . .	70
A.23	Pair plots comparing processing parameters to PCE, $J_{sc}$ , FF or $V_{oc}$ , for the second round of DRCN5T/IT-M BHJ blend optimization showing the low PCE of samples annealed at 180 °C, in box g) in the top right corner. . . . .	70
A.24	Pair plots comparing processing parameters to PCE, $J_{sc}$ , FF or $V_{oc}$ , for the second (at 160 °C) and third round of DRCN5T/IT-M BHJ blend optimization. . . . .	71
A.25	ML-generated $J_{sc}$ map for the first round of DRCN5T/IT-M BHJ blend optimization.	71
A.26	ML-generated FF map for the first round of DRCN5T/IT-M BHJ blend optimization.	72
A.27	ML-generated $V_{oc}$ map for the first round of DRCN5T/IT-M BHJ blend optimization.	72
A.28	ML-generated PCE map for the second round of DRCN5T/IT-M BHJ blend optimization. This map served as the skeleton for higher resolution sampling of the parameter space. . . . .	72
A.29	ML-generated $J_{sc}$ map for the second round of DRCN5T/IT-M BHJ blend optimization. . . . .	73
A.30	ML-generated FF map for the second round of DRCN5T/IT-M BHJ blend optimization. . . . .	73
A.31	ML-generated $V_{oc}$ map for the second round of DRCN5T/IT-M BHJ blend optimization. . . . .	74

A.32	Tabulation of the processing parameter levels, number of experiments at each level for the first and list of experiments for the first and second round of DRCN5T/IT-4F BHJ blend optimization. . . . .	74
A.33	ANOVAs of the relative contribution of the processing parameters on PCE, FF, $J_{sc}$ , $V_{oc}$ , $R_{sh}$ and $R_{sr}$ for the first round of DRCN5T/IT-4F BHJ blend optimization. . . . .	75
A.34	ANOVAs of the relative contribution of the processing parameters on PCE, FF, $J_{sc}$ , $V_{oc}$ , $R_{sh}$ and $R_{sr}$ for the second round of DRCN5T/IT-4F BHJ blend optimization. . . . .	76
A.35	Plots displaying the performance of devices that were accepted (green) and rejected (red), and the standard deviation of devices and the number of devices accepted for each experimental condition for the first round of DRCN5T/IT-4F BHJ blend optimization. . . . .	77
A.36	Plots displaying the performance of devices that were accepted (green) and rejected (red), and the standard deviation of devices and the number of devices accepted for each experimental condition for the second round of DRCN5T/IT-4F BHJ blend optimization. . . . .	77
A.37	Pair plots comparing processing parameters to PCE, $J_{sc}$ , FF or $V_{oc}$ , for the first round of DRCN5T/IT-4F BHJ blend optimization. . . . .	78
A.38	Pair plots comparing processing parameters to PCE, $J_{sc}$ , FF or $V_{oc}$ , for the second round of DRCN5T/IT-4F BHJ blend optimization. . . . .	78
A.39	ML-generated $J_{sc}$ map for the first round of DRCN5T/IT-4F BHJ blend optimization.	79
A.40	ML-generated FF map for the first round of DRCN5T/IT-4F BHJ blend optimization.	80
A.41	ML-generated $V_{oc}$ map for the first round of DRCN5T/IT-4F BHJ blend optimization.	81

A.42 ML-generated $J_{sc}$ map for the second round of DRCN5T/IT-4F BHJ blend optimization. . . . .	82
A.43 ML-generated FF map for the second round of DRCN5T/IT-4F BHJ blend optimization. . . . .	82
A.44 ML-generated $V_{oc}$ map for the second round of DRCN5T/IT-4F BHJ blend optimization. . . . .	83
A.45 ML-derived predictions of fit for the first round of DRCN5T/ITIC BHJ blend optimization. Gamma (or compliance) values were reduced until a device deviated from the linear trendline. This gamma value represents the least accommodating fit that is capable of producing a topology that tracks to the experimental data. . . .	84
A.46 ML-derived predictions of fit for the second round of DRCN5T/ITIC BHJ blend optimization. Gamma (or compliance) values are reduced until a device deviates from the linear trendline. This gamma value represents the least accommodating fit that is capable of producing a topology that tracks to the experimental data. . . .	85
A.47 ML-derived predictions of fit for the first round of DRCN5T/IT-M BHJ blend optimization. Gamma (or compliance) values are reduced until a device deviates from the linear trendline. This gamma value represents the least accommodating fit that is capable of producing a topology that tracks to the experimental data. . . .	86
A.48 ML-derived predictions of fit for the second round of DRCN5T/IT-M BHJ blend optimization. Gamma (or compliance) values are reduced until a device deviates from the linear trendline. This gamma value represents the least accommodating fit that is capable of producing a topology that tracks to the experimental data. . . .	87

A.49 ML-derived predictions of fit for the first round of DRCN5T/IT-4F BHJ blend optimization. Gamma (or compliance) values are reduced until a device deviates from the linear trendline. This gamma value represents the least accommodating fit that is capable of producing a topology that tracks to the experimental data. . . . 88

A.50 ML-derived predictions of fit for the second round of DRCN5T/IT-4F BHJ blend optimization. Gamma (or compliance) values are reduced until a device deviates from the linear trendline. This gamma value represents the least accommodating fit that is capable of producing a topology that tracks to the experimental data. . . . 89

# List of Tables

2.1	Parameters, ranges and levels for the first round of Design of Experiment optimization of DRCN5T/ITIC cells. . . . .	18
2.1	Parameters, ranges and levels for the first round of Design of Experiment optimization of DRCN5T/ITIC cells. . . . .	19
2.2	Photovoltaic metrics of champion devices after 2 rounds of optimization. Average PCE values and standard deviation in brackets. Averages based on 10, 43 and 35 devices for ITIC, IT-M and IT-4F, respectively. . . . .	31
2.3	Compliance values for each round of optimization. Higher values mean more compliant fitting. . . . .	35

A.1 Processing parameters yielding champion devices after two rounds of optimization.

\*ITIC-containing BHJs were prepared from concentrated solutions of DRCN5T (24 mg/mL) and ITIC (11 mg/mL), BHJ spin speed = 4000 rpm; \*\* BHJ spin speed 4000 rpm; †BHJ spin speed = 2000 rpm. Champion average thicknesses of ITIC = 133 nm, IT-M = 148 nm, IT-4F = 89 nm. . . . . 54

Abbreviation	Meaning
AM1.5G	Air mass 1.5 global
ANOVA	Analysis of variance
BHJ	Bulk heterojunction
CdTe	Cadmium telluride
CIGS	Copper indium gallium selenide
DOE	Design of Experiments
DRCN5T	2,2'-[(3,3',3'',4'-tetraoctyl-[2,2':5',2''-5',2''':5'',2''''-quinquethiophene]-5,5''''-diyl)bis[(Z)-methylidyne (3-ethyl-4-oxo-5,2-thiazolidinediylidene)]]bis-propanedinitrile
FF	Fill factor
GaAs	Gallium arsenide
HOMO	Highest occupied molecular orbital
IT-2F	3,9-bis(2-methylene-((3-(1,1-dicyanomethylene)-6,7-difluoro)-indanone))-5,5,11,11-tetrakis(4-hexylphenyl)-dithieno[2,3-d:2',3'-d']-s-indaceno[1,2-b:5,6-b']dithiophene
IT-M	3,9-bis(2-methylene-((3-(1,1-dicyanomethylene)-6/7-methyl)-indanone))-5,5,11,11-tetrakis(4-hexylphenyl)-dithieno[2,3-d:2',3'-d']-s-indaceno[1,2-b:5,6-b']dithiophene

Abbreviation	Meaning
ITIC	3,9-bis(2-methylene-(3-(1,1-dicyanomethylene)-indanone))-5,5,11,11-tetrakis(4-hexylphenyl)-dithieno[2,3-d:2',3'-d']-s-indaceno[1,2-b:5,6-b']dithiophene
ITO	Indium tin oxide
$J_{sc}$	Short circuit current
LED	Light emitting diode
LUMO	Lowest unoccupied molecular orbital
ML	Machine learning
MPP	Maximum power point
NFA	Non-fullerene acceptor
OPV	Organic photovoltaic
OVAT	One-variable-at-a-time
P3HT	Poly(3-hexylthiophene-2,5-diyl)
PC <sub>n</sub> BM	[6,6]-Phenyl-C <sub>n</sub> -butyric acid methyl ester
PCE	Power conversion efficiency
PTFE	Poly(tetrafluoroethylene)
$R_{sh}$	Shunt resistance
$R_{sr}$	Series resistance
SMD	Small-molecule donor
SVA	Solvent vapour annealing
TW	Terawatt
$V_{oc}$	Open-circuit potential
ZnO	Zinc oxide

# 1

## Introduction

### 1.1 Overview

This thesis explores the application of Design of Experiment to the optimization of the bulk heterojunction (BHJ) of three organic photovoltaic (OPV) architectures via commonly employed manufacturing processing parameters. Chapter 1 will provide the necessary background in photovoltaics. It will start with the case for photovoltaics, and will be followed by a brief history

of photovoltaic research and an introduction to the different families of photovoltaics. This chapter will also explain more thoroughly the structure and working principles of OPVs and, in particular, the nuanced details about the components within the light absorbing layer in these devices.

## **1.2 The Case for Photovoltaics**

The world's population is on pace to grow from 7.6 billion in 2018 to 9.7 billion by 2050,<sup>1</sup> and the world's energy consumption is projected to grow along with it, from 20 TW in 2018<sup>2</sup> to 28-30 TW in 2050, assuming steady increases in energy efficiency, population and GDP growth.<sup>2</sup> Meeting this growing energy demand will be difficult, particularly with the additional constraint of meeting Paris Climate Agreement targets.<sup>4</sup> After ratification, the Paris Agreement was signed by 197 parties that agreed to dramatically curtail their CO<sub>2</sub> emissions as soon as possible. CO<sub>2</sub> is a major driver of anthropogenic climate change,<sup>5,6</sup> and is largely produced through fossil fuel-based generation of electricity and transportation.<sup>7</sup> In 2018, fossil fuels and renewables (wind, solar and hydroelectric) accounted for 80% and 15% of global primary energy sources,<sup>2</sup> respectively, and by 2050 the International Energy Agency expects the share of fossil fuels to fall to 69% and renewables to nearly double to 28%, as shown in figure 1.1.<sup>2</sup>

This shift in energy sources will require unprecedented growth of renewable energy production. Fortunately, photovoltaics seem poised to meet this increase in production. More solar energy strikes the terrestrial earth in 1.5 hours than is globally consumed in a year.<sup>8</sup> This means that the resource base for solar energy is orders of magnitude larger than all other renewable energy sources combined.<sup>9</sup> Additionally, in recent years utilities-scale photovoltaics have reached grid parity with conventional fossil fuel power plants, as shown in figure 1.2. This drop in price is largely due the reduction in photovoltaic module costs over that same time period.<sup>10</sup>

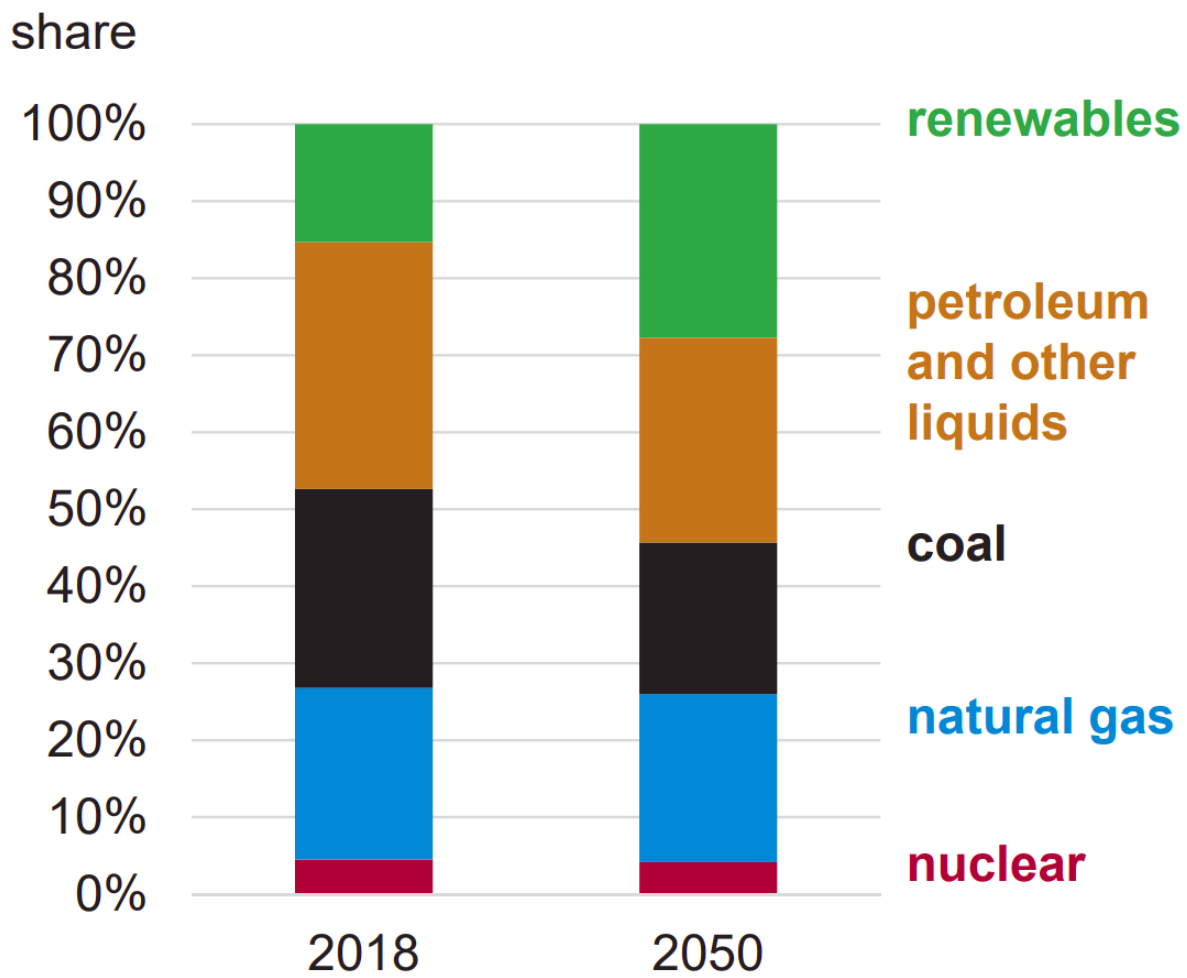


**Figure 1.1:** Global primary energy consumption in 2018 and the projected total in 2050 in the IEA reference case, by source. IEA International Energy Outlook 2019. All rights reserved.<sup>2</sup>

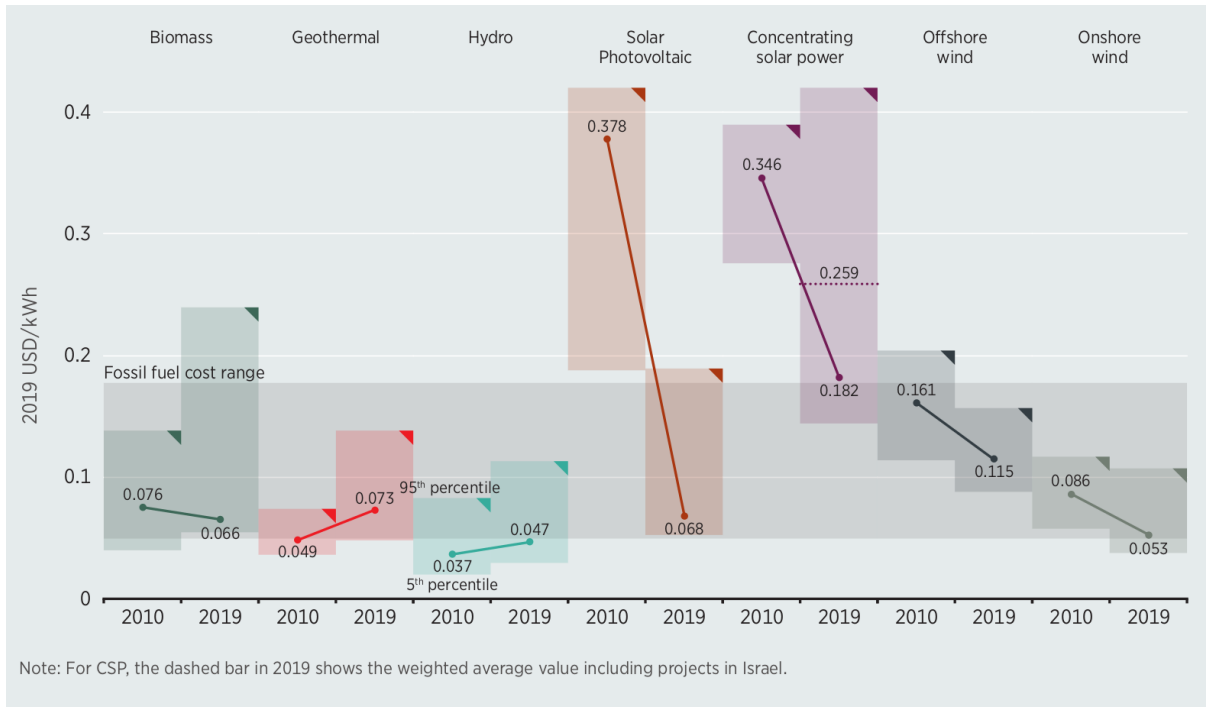


**Figure 1.2:** LCOE of renewable energy source in 2010 and 2019. Data point values and colored rectangles represent the mean price and range of prices from installations that year, respectively. Copyright © IRENA.<sup>10</sup>

### 1.3 Organic Photovoltaics

The photovoltaic effect was discovered in 1839 by french physicist Edmon Becquerel at the age of 19. However, it wasn't until the 1950s that a practical photovoltaic device was manufactured at Bell Labs.<sup>11</sup> Since then, the types of photovoltaic technologies have proliferated and major advancements have been made in the device efficiencies as shown in the iconic National Renewable Energy Laboratory (NREL) solar efficiency chart, shown in figure 1.3.

Solar cells can be loosely grouped into three generations. The first generation consists of mono- and poly-crystalline silicon-based devices. These devices are stable (demonstrating little degradation over 25 years) and efficient, and as a result make up 90% of the global PV market.<sup>12</sup> While costs have dropped impressively over the past two decades, silicon PV modules remain thick and heavy due to silicon's poor absorptivity of silicon caused by it's indirect bandgap. Module

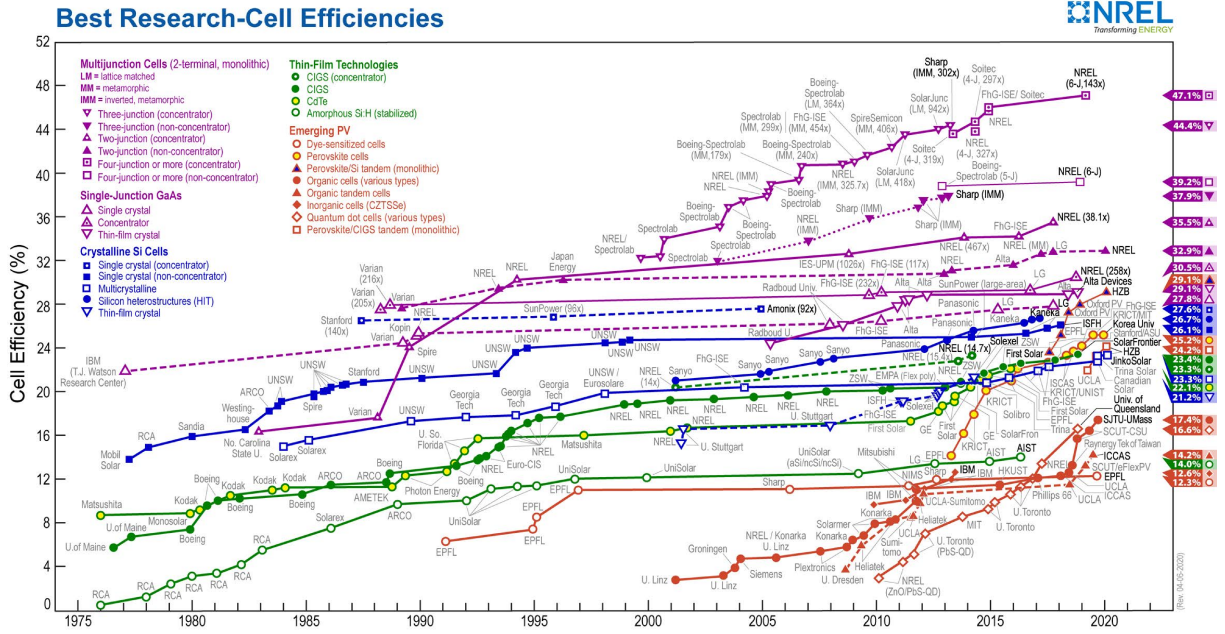


**Figure 1.3:** NREL record laboratory solar cell efficiency chart by technology type, accessed June 27, 2020 from <https://www.nrel.gov/pv/cell-efficiency.html>.

thickness limits silicon PV energy payback times and overall costs. The second generation devices consist mainly of thin film technologies such as copper indium gallium selenide (CIGS), cadmium telluride (CdTe), and gallium arsenide (GaAs). Although these second-generation devices can be made thin since they are direct bandgap compounds, they comprise scarce and toxic elements. Perovskite, organic, dye-sensitized and quantum dot solar cells, constitute the third and more experimental generation of photovoltaics. Some technologies have carved out their own sections of the market that make use of their specific advantages. For example, gallium arsenide (GaAs) solar cells are typically used for space applications where materials cost is considerably less important than weight. Organic photovoltaics (OPVs) are one of the youngest families of photovoltaic devices that are unique because they use organic semiconductors rather than inorganic semiconductors to produce electricity. As of 2020, the OPV device efficiency record stands at 17.4%,<sup>13</sup> as shown by red circles in figure 1.3. This result highlights how quickly these devices are becoming competitive from an efficiency standpoint. Additionally, these devices can be manufactured to be thin, flexible,

lightweight and semi-transparent, and may have energy payback times as short as 24 hours (at least in theory), compared to the time scale of 1-3 years for silicon.<sup>14-18</sup> They can also be manufactured with high-throughput techniques like roll-to-roll printing and spray coating.<sup>19</sup> This promise of inexpensive manufacturing makes OPVs very promising for widespread adoption.

## 1.4 Working Principles of a Solar Cell

Solar cells convert incident light into power. Power conversion efficiency (PCE) is the measure used to quantify and compare their effectiveness. In the dark, a solar cell acts as a diode, allowing current to flow easily in one direction while restricting flow in the opposite direction. Under illumination, a solar cell acts as both a diode and a current source that generates current that travels with the diode direction. An ideal cell can be modelled mathematically using the following equation:

$$I = I_L - I_0(e^{\frac{qV}{kT}} - 1) \quad (1.4.1)$$

where  $I$  is the total current,  $I_L$  is the current produced under illumination,  $I_0$  is the saturation current,  $q$  is the elementary charge of  $1.6 \times 10^{-19}$  coulombs,  $V$  is the voltage produced by the cell,  $k$  is the Boltzmann constant with a value of  $1.38 \times 10^{-23}$  J/K and  $T$  is the temperature in Kelvin. In practice, however, devices contain material defects and sources of resistive losses that result in a deviation from this behaviour, and thus a solar cell can be more accurately represented by the simplified equivalent circuits diagram in figure 1.4.

Power conversion efficiency (PCE) is the measure of a solar cell's ability to convert light into electricity and is obtained typically via a J-V test. Standard J-V tests are carried out at room

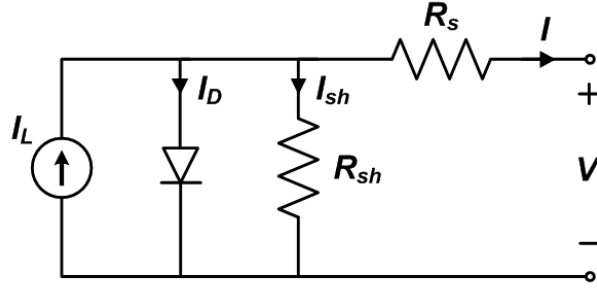


**Figure 1.4:** Simplified equivalent circuit model of a solar cell, accessed on June 29, 2020 from <https://pvpmc.sandia.gov/modeling-steps/2-dc-module-iv/diode-equivalent-circuit-models/>, where  $I_L$  is the light-generated current,  $I_D$  is the current loss from recombination,  $I_{sh}$  is the current loss from shunt resistance,  $R_{sh}$  is the shunt resistance,  $R_s$  is the series resistance, and  $I$  and  $V$  are the current and voltage produced by the cell.

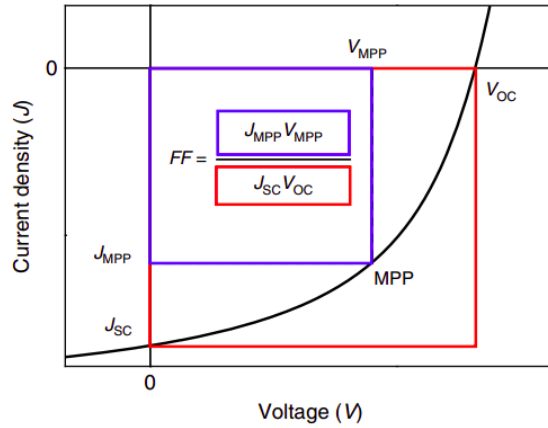


**Figure 1.5:** Typical J-V curve for a photovoltaic device and inset shows the equation for fill factor.<sup>20</sup>

temperature in ambient humidity (not always a fixed humidity) while the device is illuminated under simulated light termed air mass 1.5 global (AM1.5G). This light matches the average spectral composition and intensity of sunlight at  $48.2^\circ$  from the equator (which is closest to most population centers). Under these conditions, it's possible to extract useful photovoltaic metrics such as PCE,  $J_{sc}$ ,  $V_{oc}$  from a device. A typical J-V is shown in figure 1.5.

$$PCE = \frac{P_{max}}{P_{in}} = \frac{FF \cdot J_{sc} \cdot V_{oc}}{P_{in}} \quad (1.4.2)$$

The other factor that needs to be considered for a high efficiency solar cell is the fill factor, which is a measure of the quality of the junction. It represents the ratio of the maximum power generated by the solar cell (area of blue outline) to the product of the short circuit and open circuit voltages (area of red outline), the equation is shown inset in figure 1.5. With these variables measured, PCE of a device can be calculated as shown in equation 1.4.2.

## 1.5 Organic Solar Cell Architecture

Organic solar cells get their name from the fact that they are assembled from organic semiconductors with sufficient bandgaps to capture light and produce current. In an OPV, there are five main steps in the production of current: 1) photoexcitation, 2) exciton diffusion, 3) exciton dissociation, 4) carrier migration and 5) charge extraction. All five steps are shown below in figure 1.6. Inside a silicon solar cell, photoexcited electrons produced from absorption of light have enough thermal energy at room temperature to become freed from their corresponding nucleus and thus can contribute to current in a device. This is due to silicon's inherently large relative permittivity of 11.7,<sup>21</sup> which allows electrons to be electronically isolated from the hole that is left at their initial energy level. Organic semiconductors on the other hand have lower relative permittivities of 2 - 4.<sup>22</sup> This means that when light is absorbed by organic semiconductors, electrons are excited to higher energy levels from the HOMO to the LUMO (lower and upper edges of bands in figure 1.6, respectively) but remain bound to the molecule itself as their thermal energy is not sufficient to free them in any meaningful abundance. Photon absorption and the resulting photoexcitation is shown in figure 1.6b) labelled (1). Additionally, as an electron is promoted from the HOMO to the LUMO, a vacancy is formed at the energy level previously occupied by the electron. This is referred to as a hole, a positively-charged quasiparticle and charge carrier. Being that the electron has a negative charge and the hole the absence of a negative charge (thus a positive

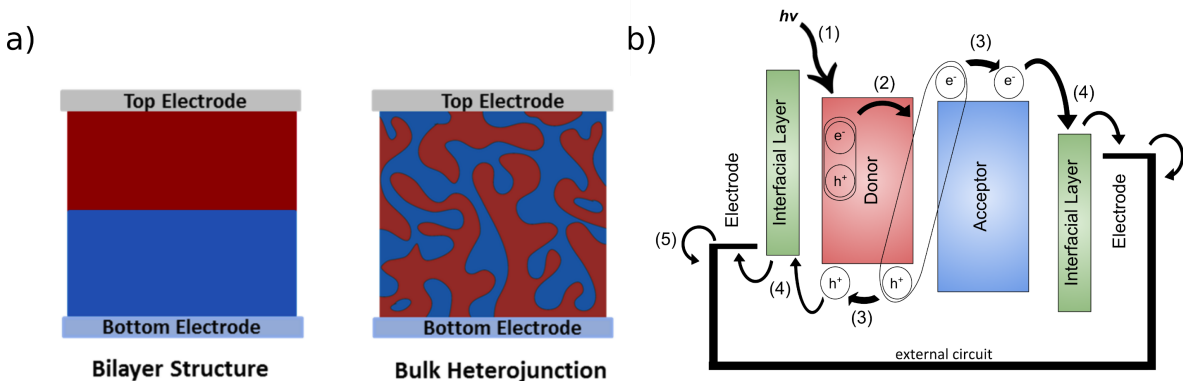


**Figure 1.6:** a) Structure of a bilayer and a bulk heterojunction<sup>25</sup> and b) Major processes involved in current production in an OPV: 1) photoexcitation, 2) exciton diffusion, 3) exciton dissociation, 4) carrier migration and 5) charge extraction.

charge), the two carriers are attracted to one another. This electrostatic binding of an electron and a hole is referred to as an exciton, which is an inherently unstable quasiparticle. Excitons themselves are not charge carriers capable of producing current but if they overcome the exciton binding energy holding them together and split, two charge carriers are formed, an electron and a hole. In an organic solar cell, this splitting is accomplished by migration of an exciton to an interface with different material (step 2) and the transfer of either the electron or the hole to an adjacent molecule (step 3). As a result, OPV devices contain at least two light-absorbing organic semiconductors, one that donates an electron (donor material) and one that accepts them (acceptor material). At this point, electrons and holes are free to travel to their respective electrodes (step 4). However, current losses can still occur as a result of defects in the donor or acceptor material and/or interfaces with the interfacial layers and/or electrodes. Very nuanced discussions in charge losses can be found in various good reviews on the topic.<sup>23</sup> If charge carriers reach the electrode, charge extraction (step 5) can occur and current is produced.

In 1995, A.J. Heeger et al. produced the first OPV device with a bulk heterojunction (BHJ).<sup>26</sup> A BHJ is a single layer containing an intimate mixture of the donor and acceptor materials. This morphology dramatically increases the interfacial area between donor and acceptor molecules and

thus increases likelihood of exciton dissociation and current generation. A simplified comparison of a bilayer photoactive layer and a BHJ are shown in figure 1.6a). This concept proved so useful that in current research nearly all OPV devices contain BHJs.

## 1.6 Bulk Heterojunction Components

Historically, BHJs comprised a polymer donor such as P3HT (poly(3-hexylthiophene-2,3-diyl)) and a fullerene derivative such as PC<sub>71</sub>BM ([6,6]-Phenyl-C<sub>71</sub>-butyric acid methyl ester).<sup>27,28</sup> Low bandgap polymers are widely used as the donor however and an array of such donors have been used in research for over a decade.<sup>29</sup> Small molecule donors (SMDs) have garnered significant interest in the past few years,<sup>30-34</sup> largely because SMDs are free from problems that commonly afflict polymers such as batch-to-batch variability of molecular weight and challenges of purification.<sup>35,36</sup> Fullerenes, the most commonly used acceptor component of the BHJ, exhibit weak absorptivities in the visible range and their energy levels are not easily modulated.<sup>37</sup>

Non-fullerene acceptors (NFAs) overcome these challenges by offering chemical tunability, absorption profiles complementary to most donor materials, and easily tuned HOMO and LUMO levels.<sup>34,39-41</sup> As a result, NFAs have surged in popularity and now feature in nearly all high PCE devices. NFAs are organized into a few chemically related families such as: PDI,<sup>42</sup> and A-D-A-style acceptors with former being the most popular. A-D-A acceptors are composed of an electron-rich moiety (donor) in the center with electron-poor moieties (acceptors) on either end. Y6 (2,2'-((2Z,2'Z)-((12,13-bis(2-ethylhexyl)-3,9-diundecyl-12,13-dihydro-[1,2,5]thiadiazolo[3,4-e]thieno[2'',3'':4',5'])thieno[2',3':4,5]pyrrolo[3,2-g]thieno[2',3':4,5]thieno[3,2-b]indole-2,10-diyl)bis(methanylylidene))bis(5,6-difluoro-3-oxo-2,3-dihydro-1H-indene-2,1-diylidene))dimalononitrile) and ITIC (3,9-bis(2-methylene-(3-(1,1-dicyanomethylene)-indanone))-5,5,11,11-tetrakis(4-hexylphenyl)-dithieno[2,3-d:2',3'-d']-s-

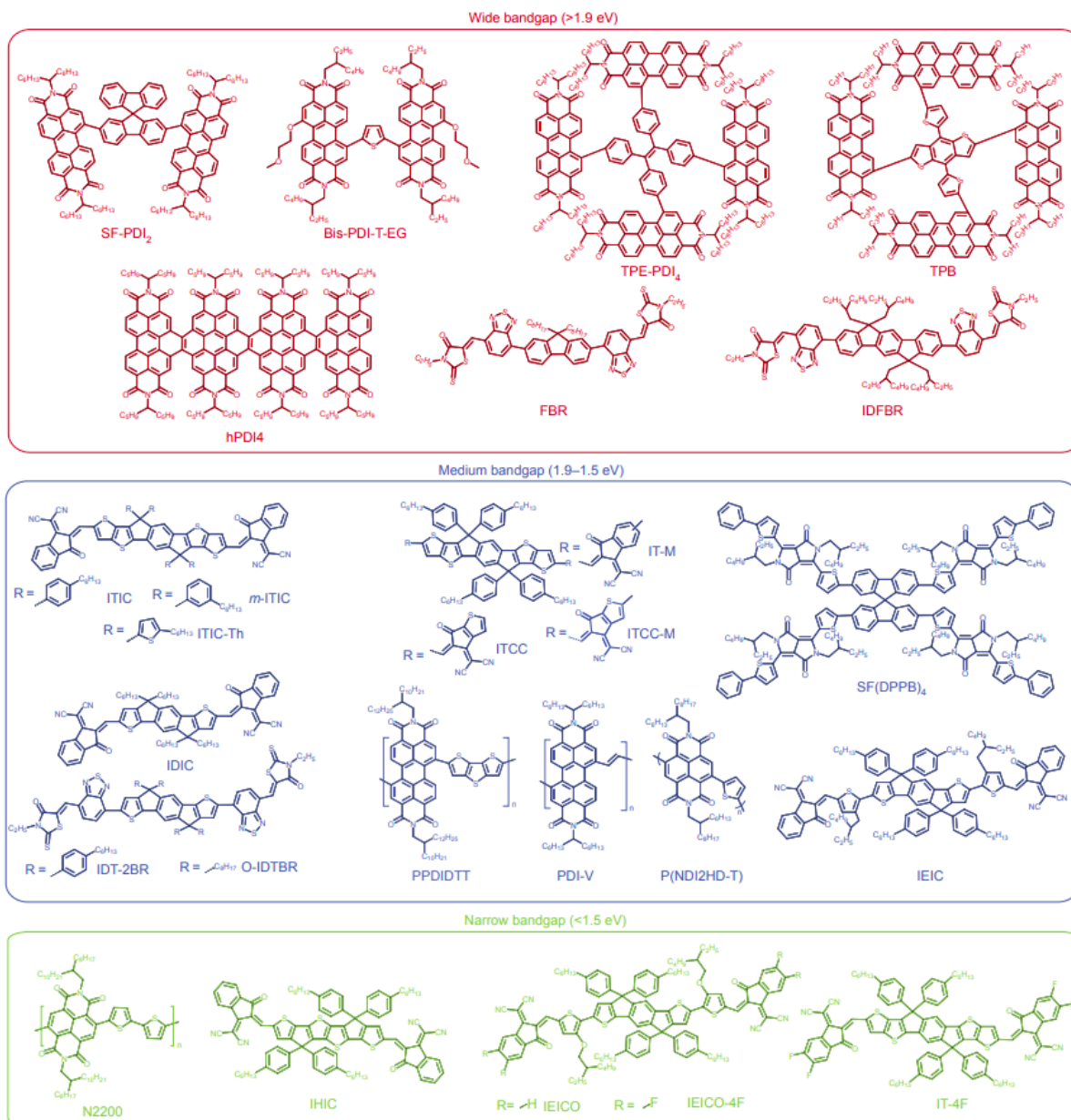


**Figure 1.7:** Structures of various non-fullerene acceptors that have replaced fullerene derivatives in popularity and performance.<sup>38</sup>

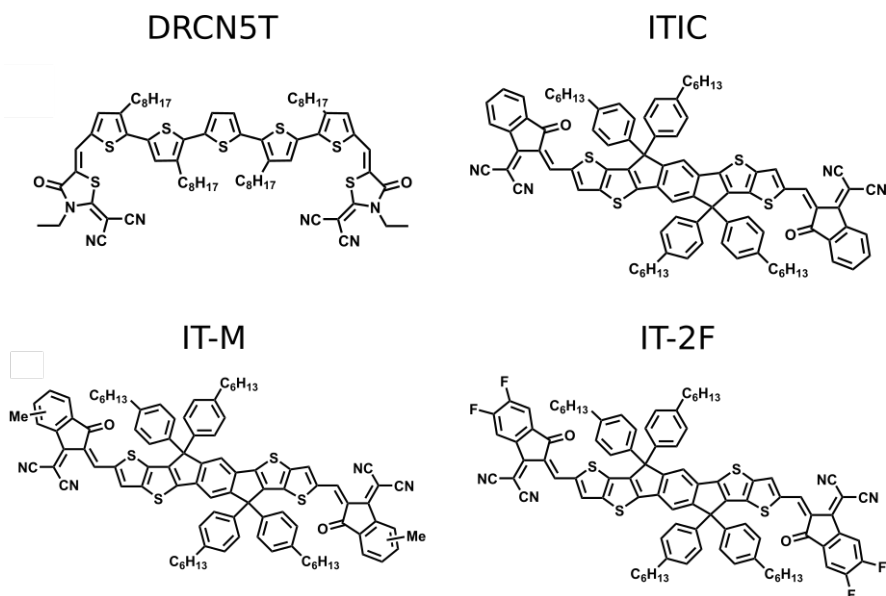


**Figure 1.8:** Structures of the donor material, DRCN5T and the three acceptor materials ITIC, IT-M and IT-4F, that constitute the BHJ mixtures in this work.

indaceno[1,2-b:5,6-b']dithiophene) as well as its many related derivatives<sup>38,43,44</sup> are the most widely used in as shown in figure 1.7 (ITIC-Th, m-ITIC, IT-M, ITCC, IT-2F).

These acceptors offer the possibility of excellent tunability of absorption properties through versatile organic syntheses.<sup>45,46</sup> Despite these advantages, achieving an ideal nanoscale morphology in a BHJ comprising both small molecule donors and acceptors is challenging. The fine balance between the interconnected and competing factors that promote crystallization of both molecular components in the blend, the kinetics of self-assembly of the nanostructured BHJ, as well as physical factors such as solvent evaporation during film casting and thermal annealing, renders this process difficult to optimize.<sup>47-49</sup>

## 1.7 Design of Experiments

In spite of the wide range of combinations of processing parameters, BHJs are typically optimized in a one-variable-at-a-time (OVAT) fashion, resulting in lengthy and often incomplete or unsatisfactory device optimization. In addition, the actual process of optimization of OPV devices is often not described in any real detail in the literature, and thus little is known about combinations that did not work. It is therefore difficult to ascertain whether OVAT optimization has indeed led to the “best” possible performance for a given set and range of variables tested as these parameters are often interconnected and convoluted—varying one could affect others simultaneously.<sup>50</sup> In addition, anthropogenic biases can influence decision-making in a negative manner.<sup>51</sup> An optimization method previously introduced by our research group for OPVs combines Design of Experiment (DOE) and machine learning (ML) approaches to (i) reduce the time required to optimize an OPV system, and (ii) increase the probability of discovering a true optimum.<sup>52</sup> DOE is a rational method that samples large parameter spaces in a sparse but mathematically deliberate fashion that minimizes bias. ML-based algorithms are then combined with the DOE methodology to visually interpret the results and provide guidance for future experimental optimization conditions.

Much of the landscape of the ML literature in the area of OPV uses computational methods to screen candidate molecules for high power conversion efficiencies (PCEs)<sup>53–56</sup> to accelerate materials discovery.<sup>57</sup> In the broader space of materials for clean energy applications, the combining of (sparse) experimental data with ML approaches is growing as the methods become more accessible, widely known and demonstrated. A very recent example is the concept of autonomous self-driving laboratories that perform experimentation *and* analysis, and even suggesting next steps, as shown for thin film materials for perovskite-based PV and other electronic devices.<sup>58</sup> Another example describes the application of a response-surface methodology to tailor the phase and size

of Ni<sub>2</sub>P nanoparticles, which are used as catalysts for hydrogen evolution reactions.<sup>59</sup> Machine-learning-in-the-loop has been used to optimize the synthesis of PbS colloidal quantum dots for solar cells.<sup>60</sup> An iterative ML approach enabled the optimization of transparent conductive oxides that serve as the basis for OPV and other optoelectronic devices.<sup>61</sup> In terms of method development, Aspuru-Guzik's Phoenix algorithm demonstrates a generalizable Bayesian approach for systems and devices with scant sampling (such as OPV devices) that are "black-box unknown objective functions."<sup>62</sup>

In this work, all-small molecule OPV devices containing the donor molecule DRCN5T and one of three NFAs ITIC, IT-M or IT-4F, whose structures shown in figure 1.8, were optimized using an ML and DOE based approach. This work aims to explore the efficacy of the DOE+ML methodology for optimizing new BHJs based upon combinations of small molecules that have not seen much prior exploration. We show how this approach can be used to explore a large parameter space with little prior knowledge in an iterative fashion. The optimization of multiple processing parameters simultaneously, reducing the number of experiments required to explore such a parameter space to a fraction of what is required for OVAT optimization.

# 2

## Optimization of OPV device bulk heterojunctions

The OPV devices in this study had an inverted device architecture with ZnO and MoO<sub>x</sub> interfacial layers and ITO and Mg/Al as the electrodes, as shown in figure 2.1. In normal architecture devices, holes are collected at the ITO and electrons at the metal back electrode and in inverted architecture devices either charge carrier is collected at the opposite electrode. In practice, some BHJ blends

perform better with normal or inverted architecture for a multitude of reasons.<sup>63</sup> The BHJs consisted of the small-molecule donor DRCN5T and one of 3 non-fullerene acceptors, ITIC, IT-M or IT-4F. The flatband HOMO and LUMO levels as well as the chemical structures of the donor and acceptor materials are shown in figure 2.1.

DOE is more effectively implemented with some preliminary information since the variable space for a new material or device is often so vast—the first step of choosing a starting point may be difficult. Preliminary exploration can provide useful insights into simple questions of solubility of the components being studied, their thermal stability, and other specifics of the system being evaluated. Since little was known of these combinations of compounds for formulating an optimal BHJ, preliminary cells were prepared to evaluate three fundamental parameters: (i) exploration of three of the most typically used chlorinated solvents to determine which, if any, would result in uniform films of the small-molecules comprising the BHJ, (ii) whether thermal annealing was linked to efficiency,<sup>64–66</sup> and (iii) a rough range of ratios of the two components in the BHJ that would result in OPVs with efficiencies greater than ~1%. An initial screening of commonly used chlorinated solvents, chloroform, 1,2-dichlorobenzene and chlorobenzene, showed that only layers comprising the components of the BHJ cast from chloroform yielded continuous films when spin-cast onto the ZnO layer, as shown in figure A.2. Thermal annealing was deemed essential as all devices fabricated without thermal annealing had PCEs less than 0.5%. Lastly, BHJs with donor fractions less than 0.5 generally showed low (< 0.5%) power conversion efficiencies, thus providing a lower boundary for optimization. These preliminary exploratory devices also revealed that the BHJ films often appeared non-uniform by visual inspection and were accompanied by particulates and streaks (even with filtration through a 0.22  $\mu\text{m}$  PTFE filter prior to spin-casting); preparation of devices in duplicate was especially important to account for experimental variability.

With the preliminary exploration complete, the DOE approach centered on the optimization of 4 BHJ processing parameters: total solution concentration of the donor and acceptor, the ratio

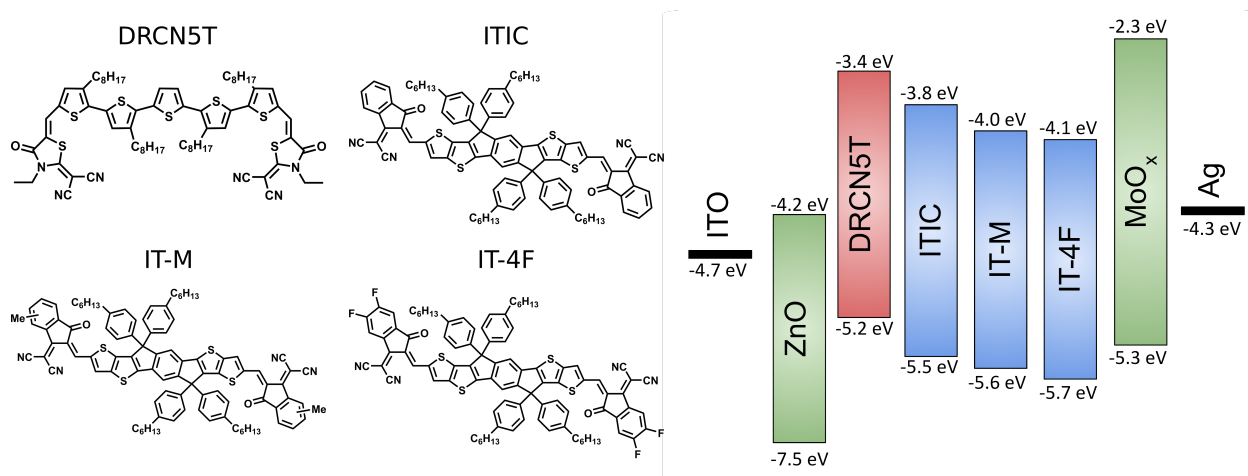


**Figure 2.1:** a) Structures of the donor (DRCN5T) and acceptor molecules (ITIC, IT-M and IT-4F), b) OPV device flatband diagram aligned at vacuum level. Values for the HOMO and LUMO levels are derived from the following references: DRCN5T,<sup>67</sup> ITIC,<sup>68</sup> IT-M,<sup>69</sup> IT-4F,<sup>70</sup> and all other materials.<sup>71</sup>

of donor:acceptor (represented by the donor fraction), the thermal annealing temperature, and the duration of the thermal annealing. Layer thickness is in part dictated by the viscosity of the BHJ solution used for spin-casting and thus solution concentration is a proxy for layer thickness.<sup>72</sup> Total concentration refers to the total weight of donor and acceptor dissolved in a known volume of chloroform. Donor fraction refers to the weight fraction of the donor material to the total weight of donor and acceptor dissolved in solution.

The goal of the first round of DOE optimization is to sample a parameter space sufficiently wide to try to encompass all performance maxima (in this case, the PCE) within the range of chosen processing parameters. It is not feasible to investigate the entire parameter space of any given system, and larger ranges will require a larger number of levels (sampling points in a range) in order to capture sharper features of the response landscape. If for example, a donor fraction range of 0.1–0.9 is chosen, the number of levels (different values of donor fractions tested) required to attain useful resolution of this parameter range would require a burdensome number of devices. The information presented in table 2.1 displays the processing parameters, ranges, and levels investigated in the first round of optimization for the DRCN5T/ITIC BHJ

combination. A full factorial design (*i.e.* testing every possible combination of levels for each parameter) of this parameter space would consist of a total of  $4^2 \times 3^2 = 144$  experiments/devices. The production of 6-device batches of OPVs, takes  $\sim 6$  hours in our case, meaning that a full factorial design would require roughly 144 hours of hands-on experimental time. Even without accounting for the necessity of preparing devices in duplicate, this first round of exploratory DOE quickly becomes experimentally prohibitive. Given this fact, the number, range and/or levels of processing parameters could be reduced in order to decrease the number of devices manufactured, or one could apply a different sampling method. Employing the latter, a generalized subset design (GSD) would reduce the DOE array to a more tractable number of experiments, where the number of experiments is reduced by an integer fraction of the full factorial amount.<sup>73</sup> The degree of integer reduction is chosen to be as large as possible while still realizing close to the same number of experiments at each parameter level (See the Appendix for a more detailed description of integer reduction).

## 2.1 DRCN5T/ITIC-based BHJs

**Table 2.1:** Parameters, ranges and levels for the first round of Design of Experiment optimization of DRCN5T/ITIC cells.

<b>BHJ concentrations (mg/ml)</b>	5.0	7.5	10.0	12.5
<b>Number of experiments</b>	4	6	6	4
<b>Donor Fractions</b>	0.6	0.7	0.8	0.9
<b>Number of experiments</b>	4	6	6	4
<b>Annealing Temperatures (°C)</b>	120	140	160	

**Table 2.1:** Parameters, ranges and levels for the first round of Design of Experiment optimization of DRCN5T/ITIC cells.

<b>Number of experiments</b>	7	6	7
<b>Annealing Time (seconds)</b>	100	200	300
<b>Number of experiments</b>	7	6	7

Through implementation of integer reduction of the DOE array using the GSD algorithm, the total number of experiments was reduced from 144 reduced to 20, with a close to equal number of experiments performed at each different parameter level. A detailed list of each of the parameter levels for each of the 20 experiments can be found in figure A.3. For all experimental conditions, at least two chips comprising 5 cells each (10 cells total) were fabricated and tested.

Before analysis, the data is passed through a filter that excludes non-representative data (statistical outliers) that would otherwise skew the analyses. Devices exhibiting anomalous metrics compared to others made under the same experimental conditions can be systematically identified and excluded according to precise rejection criteria. Examples of devices with anomalous metrics include those with shorts in the device, and thus should be rejected as non-representative. Here we apply a universal rejection of  $V_{oc} < 0.65$  V, which is likely to result from a device defect. On average, 8 devices from each experiment will pass the data filter but some combinations of processing parameters lead to devices that are more likely to be rejected. The data that does pass this filter comprises the dataset analyzed in the following steps.

An analysis of variance (ANOVA) is then conducted in order to quantify the relative contribution of each processing parameter.<sup>52</sup> A lower percent contribution means that the

processing parameter has little impact, relative to the other parameters within the range tested. The ANOVA in figure 2.2 shows the contribution of all 4 processing parameters, total concentration, donor fraction, annealing temperature, and annealing duration on the PCE from the first round of DRCN5T/ITIC optimization. The ANOVA reflects the data acquired from the 20 experiments outlined in figure A.3. Donor fraction and total concentration influence the PCE to the greatest degree over the ranges tested with annealing temperature contributing very little. It is important to note that the small contribution from annealing temperature does not mean that annealing temperature is an insignificant processing parameter, but rather that the range tested was too narrow to have a major effect on performance. Each processing parameter influences PCE as noted by the variance of the  $J_{sc}$ ,  $V_{oc}$ , FF,  $R_{sh}$ , or  $R_{sr}$  to different degrees; a set of ANOVA for each round of optimization is provided in the Appendix, as well as pair plots for each processing parameter and photovoltaic metric ( $J_{sc}$ ,  $V_{oc}$ , *etc.*). A pair plot is simply a scatter plot of any two studied metrics (*e.g.*  $J_{sc}$  vs total concentration) that can be used to graphically assess any correlations between any two parameters/metrics of interest. The pair plots for every pair of parameters/metrics are shown in figure A.8. From these pair plots, it becomes clear that PCE is most heavily influenced by donor fraction (as previously concluded from the ANOVA). Subplots of figure A.8 e,m show that devices with a donor fraction of 0.8 had dramatically higher PCE and  $J_{sc}$  than other donor fractions.

The topographic-style maps shown in figure 2.3 are a digestible and succinct representation of the data from the experiments outlined in figure A.3, of the first round of DRCN5T/ITIC blend optimization. The maps relate an output (in this case PCE, but in other cases  $J_{sc}$  or FF) to the processing parameters. Each data point represents the champion device from every one of the prescribed devices in the experimental list in figure A.3. The entire array of PCE plots for the first round of DRCN5T/ITIC optimization includes all 4 processing parameters. In this figure, within a row, every map has the same annealing duration [*e.g.* maps (a), (b) and (c) contain data points of devices that had annealing durations of 300 s] and within a column, every map has the same

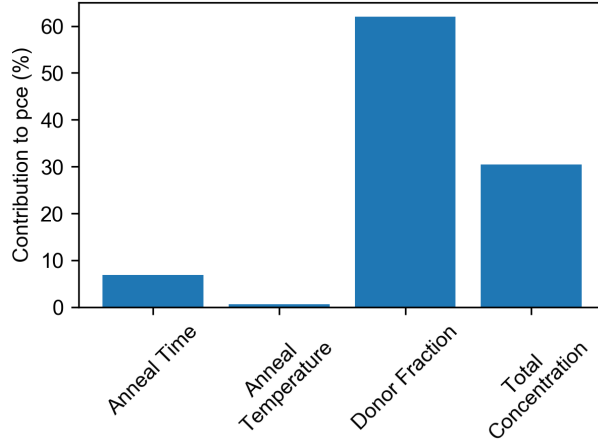


**Figure 2.2:** ANOVA plot from the first round of optimization of the BHJ comprising DRN5T/ITIC, revealing the relative contribution of each processing parameter on the resulting PCE. In the range tested, the annealing temperature has little influence on PCE.

annealing temperature [*e.g.* maps (a), (d) and (g) contain data points of devices that were annealed at 120 °C].

As previously mentioned,  $J_{sc}$  and PCE are highly correlated and this observation is corroborated by the similarity between the  $J_{sc}$  ML maps in figure A.10 and the PCE maps in figure 2.3. Devices produced at a total concentration <8 mg/mL displayed relatively low PCE (figure 2.3) and  $J_{sc}$  (figure A.10), independent of donor concentration and annealing temperature. Films spin-cast from solutions of lower concentrations would be expected to lead to thinner films and thus to lower short-circuit currents as fewer photons can be absorbed.

The most promising region of the parameter space for producing high efficiency devices in figure 2.3 is found at total concentrations >10 mg/ml, donor concentrations of ~0.75–0.8, and an annealing temperature of ~140 °C. This information from the first round of optimization was then used to inform the new parameter ranges for the second round of optimization. 4 total concentrations of 8, 11, 14 and 17 mg/mL, 3 donor fractions of 0.65, 0.75, and 0.85, 3 annealing temperatures of 130, 140 and 150 °C, and 3 annealing times of 1.5, 4 and 6.5 min were selected

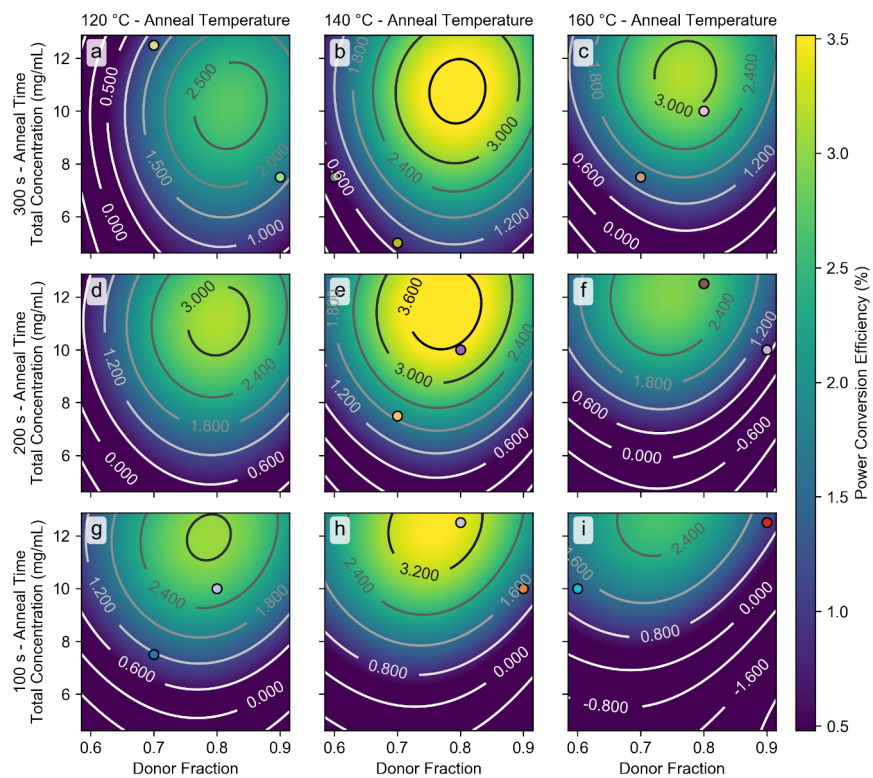


**Figure 2.3:** ML-generated PCE maps for the first round of optimization of the DRCN5T/ITIC BHJ devices. This set of maps shows the effect of all four processing parameters on PCE, with areas of higher PCE represented by yellow, and lower by blue.

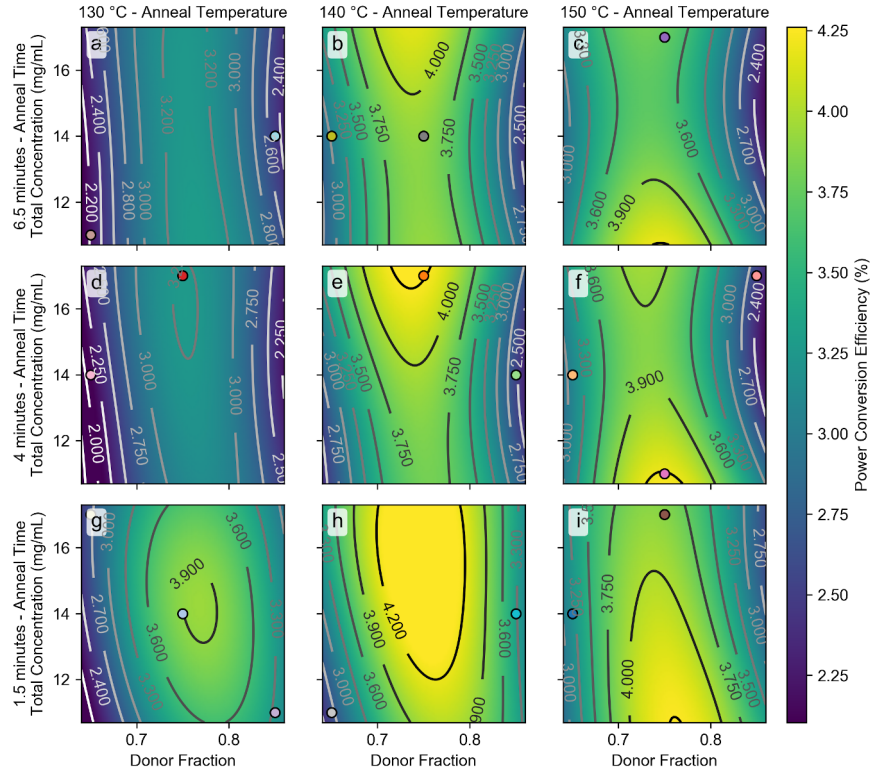


**Figure 2.4:** ML-generated PCE maps for the second round of optimization of the devices based on a BHJ composed of DRCN5T/ITIC. These maps are acquired at a higher sampling resolution in a narrower range of parameter space than the first round of optimization, shown in figure 2.3.

for the second round of optimization. The number of experiments of a full factorial design of 108 was reduced to 20 by using the integer reduction method explained earlier and are enumerated in figure A.3, labelled ITIC Round 2. The corresponding maps for the second round of DRCN5T/ITIC BHJ mixtures are shown below in figure 2.4.

From the plots in figure 2.4, it is clear that the optimum donor fraction appears to be captured within the studied range, suggesting that a maximum PCE is achieved at value of  $\sim 0.76$ . The PCE is influenced dramatically by donor fraction in this round of optimization, and the effect of annealing temperature is small, as shown in figure A.7. The chosen range for the donor fraction in this round of optimization (0.65–0.85) may simply be wider than the other processing parameters. As an extreme example, if a range of annealing temperatures from 10–1000 °C had been chosen, the ANOVA

would certainly have shown that temperature would have a much larger effect on PCE than donor fraction; here, such a narrow temperature range would be expected to be less significant. Devices manufactured with a donor fraction of 0.75 displayed the highest PCE and were accompanied by maximization of the  $J_{sc}$ , as shown in figure A.9m. PCE varies little across total concentration, annealing temperature, and annealing time, as shown in figure A.9 f,g,h, respectively.

Lastly, it is important to note the sparsity of data points in certain individual maps. When reducing the number of experiments used to explore a parameter space, there is always an inherent trade-off between sampling resolution and number of devices fabricated. Comparing the champion device from the first and second rounds of optimization, the PCE increased from 3.5% to 4.3%, the  $J_{sc}$  from 9.2 mA/cm<sup>2</sup> to 10.2 mA/cm<sup>2</sup>,  $V_{oc}$  from 0.89 V to 0.96 V, while the FF remained unchanged at 0.43. This increase in PCE from round one to round two of optimization highlights the iterative power of this approach. It allows researchers to narrow ranges of processing parameters or to exclude certain parameters altogether in order to investigate more promising (higher PCE) areas identified in the first round of optimization.

## 2.2 DRCN5T/IT-M-based BHJs

The related derivative, IT-M, varies only by the addition of two methyl groups on the extreme ends of the ITIC molecule, and has similar HOMO/LUMO levels to that of the parent ITIC, as shown in figure 2.1. As described earlier for the parent ITIC derivative, preliminary screens of DRCN5T/IT-M devices showed that thermal annealing is required to achieve a PCE greater than 0.5%. These tests also showed that at an annealing temperature of 140 °C and increasing annealing time from 8 min to 32 min had no effect on PCE. Device PCEs increased with annealing times up to 8 mins and plateaued. As a result, for the first round of optimization, a fixed annealing time of 8 min was chosen, thereby eliminating time as a variable to optimize. The processing parameters optimized

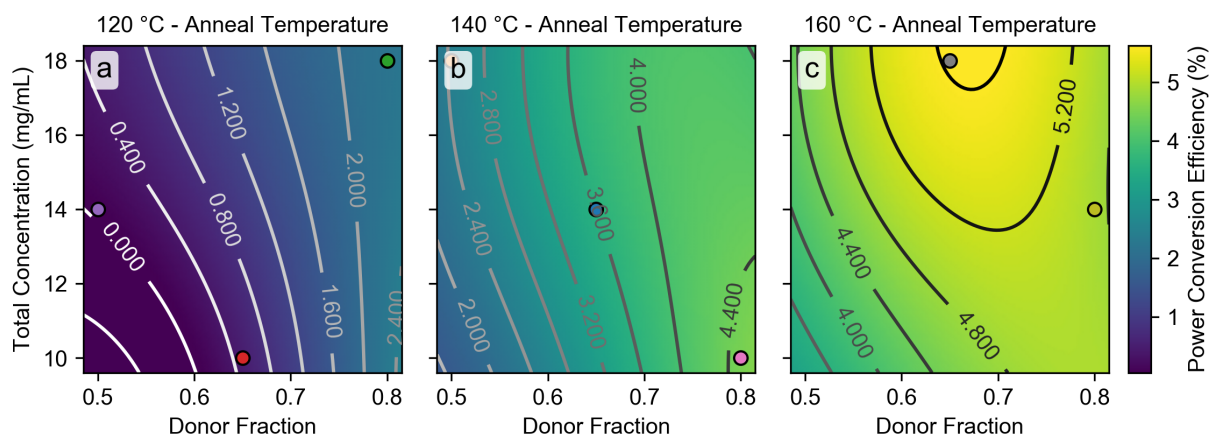


**Figure 2.5:** Maps of PCEs as generated *via* ML methods for the first round of optimization for the devices comprising a BHJ of composition of DRCN5T/IT-M. A fixed annealing time of 8 min reduces the dimensionality of this round of optimization to 3 processing parameters, reducing the parameter space and increasing data point density.

in the first round included (i) BHJ solution total concentration, (ii) BHJ solution donor fraction, and (iii) annealing temperature at a fixed annealing time of 8 min. Having reduced the number of processing parameters from 4 to 3, if each parameter has 3 levels, the full factorial design would have 27 distinct experimental conditions that can be reduced to just 9 experiments using GSD sampling. The table of processing parameters levels for the first round of optimization as well as the experiment list can be found in the Appendix, in figure A.16. The resulting PCE maps from the first round of DRCN5T/IT-M optimization along with the corresponding ANOVA plots, are presented below in figure 2.5.

The plots in figure 2.5 a,b,c show the effect of annealing at temperatures of 120, 140 and 160 °C, respectively. Scanning the plots from left to right reveals that devices annealed at higher temperatures exhibit higher PCEs. This observation is corroborated by the ANOVA for PCE in figure A.21, which highlights the contribution that annealing temperature plays on the PCE. The linkage between temperature and PCE is the focus of the next round of optimization. Annealing devices at 160 °C increased the PCE primarily through an increase in the FF of figure A.26b. Given the shallower LUMO level of IT-M (-3.98 eV),<sup>69</sup> compared to ITIC (-3.83 eV),<sup>68</sup> the

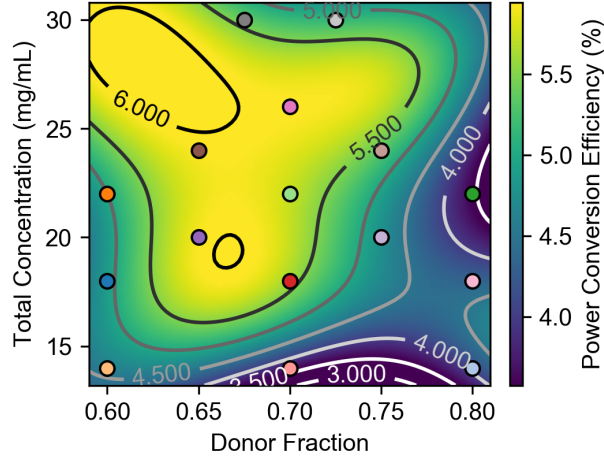


**Figure 2.6:** Maps of PCEs as generated *via* ML methods for the second round of optimization of DRCN5T/IT-M-based devices. An optimal annealing temperature of 160 °C was identified, leaving two processing parameters to optimize, the donor fraction and total concentration.

observed decrease in  $V_{oc}$  shown in figure A.27 is expected.<sup>74,75</sup> As shown in figure A.20, the total concentration of the BHJ solutions influences PCE and  $J_{sc}$  very little and as such the range was extended substantially for the second round of optimization.

In the second round of optimization of the DRCN5T/IT-M combination, higher annealing temperatures of 160, 180 and 200 °C were chosen, as well as a narrower range of BHJ solution donor fractions of 0.6, 0.7 and 0.8. With 3 levels per parameters, this yields a full factorial design of 27 unique experimental conditions that were reduced to just 9 after GSD integer reduction. The table of processing parameters for the second round of optimization and corresponding list of experiments can be found in the Appendix, figure A.16. Devices annealed at 200 °C had substantially lowered  $V_{oc}$ s, dropping from roughly 0.9 V to values ranging from 0.7–0.2 V. Figure A.18a shows the distribution of PCEs for devices made under each set of experimental conditions; experimental labels match those assigned in figure A.16 for round 2. Figure A.18c displays the number of devices from each experimental condition to pass the data filter; it shows that devices that were annealed at 200 °C were all rejected by the data filter based on low  $V_{oc}$ s (experiment #2, #6 and #8). While it is important to include data from devices with high and low PCEs, it seems that annealing at 200

°C is detrimental. In some instances, devices annealed at 180 °C also showed drops in  $V_{oc}$  of up to 0.3 V, and most devices annealed at 180 °C had lower PCEs than those annealed at 160 °C, as shown in figure A.23g. At this point, instead of continuing forward as planned, devices annealed at 180 and 200 °C were omitted from this analysis as focusing on devices annealed at 160 °C seemed more fruitful, providing more consistent and reproducible results.

The experiments originally designated to be annealed at 180 or 200 °C, as per the generated list in figure A.16, were instead run at 160 °C. The resulting map can be found in the Appendix as figure A.28. This map contains some high PCE features that were deemed worthy of further exploring. As a result, specific devices were prepared in order to increase the density of data points in this promising parameter space. The map derived from this more granular data for the DRCN5T/IT-M BHJ composition is shown in figure 2.6, and it shows a rather flat PCE landscape. In the range tested, the total solution concentration of BHJ components and the donor fraction had equal contributions on the resulting PCE, as shown in PCE ANOVA in figure A.21. PCE did not vary with a total concentration of 20-26 mg/mL and donor fractions of 0.65–0.70. After this second round of optimization, the champion device had a PCE of 5.9%,  $J_{sc} = 12.2 \text{ mA/cm}^2$ ,  $FF = 0.53$  and a  $V_{oc} = 0.93 \text{ V}$ . This champion device shows little improvement from the first round of DRCN5T/IT-M optimization whose champion had a PCE of 5.7%. The fact that no further improvement in PCE was noted in generation two suggests that a maximum has been reached and that further optimization of these parameters will probably not be fruitful, which is useful information.

## 2.3 DRCN5T/IT-4F-based BHJs

The IT-4F derivative has two pairs of fluorines on the extreme ends of the ITIC molecule, further lowering the HOMO and LUMO levels compared to the two acceptors described thus

far. Preliminary devices demonstrated the need to optimize all 4 processing parameters. Three levels were chosen for every parameter except for annealing temperature where two levels were chosen. This yields 81 possible combinations that were reduced using GSD sampling to a list of 13 experiments, that can be found in figure A.32. Based upon the results with ITIC and IT-M, narrower windows of BHJ solution donor fraction (0.6–0.8) and annealing temperatures (150 and 170 °C) were chosen. Figure 2.7 below displays the results from the first round of optimization.

Comparing the columns of subplots in figure 2.7, devices annealed at 150 °C exhibit substantially higher PCEs than devices annealed at 170 °C. This finding is corroborated by the pair plots in figure A.37. The maps in figure A.39 display similar topologies, suggesting that an increased  $J_{sc}$  for devices annealed at 150 °C is the main driver of increased PCE. Figure A.33a shows that annealing temperature most heavily influences PCE within this range.

Devices prepared with lower total concentrations (representing the bottom half of each map in figure 2.7) exhibited higher PCEs. Figure A.37 f,h demonstrate that lower total concentrations and longer annealing times result in devices with higher PCE. The device with the highest PCE (experiment #11 figure A.32) had a BHJ solution concentration and donor fraction of 16 mg/mL and 0.7, respectively, and was annealed at 150 °C for 12 min. The distribution of PCEs varies little with different donor fractions (figure A.37e) and as a result, a fixed donor fraction of 0.7 was chosen for all devices in the second round of optimization.

For the second round of optimization, annealing temperatures of 130 and 150 °C, total concentrations of the BHJ solutions of 13, 16 and 19 mg/mL, and longer annealing times of 12, 20 and 28 min, were chosen. GSD sampling enabled a reduction of experimental conditions to a list of 6 experiments, which are outlined in figure A.32, titled Round 2. The resulting PCE maps are presented in figure 2.8. Since the BHJ solution donor fraction was not optimized in this round, the axes for these maps are different from the earlier maps. The x- and y-axes of each plot correspond to

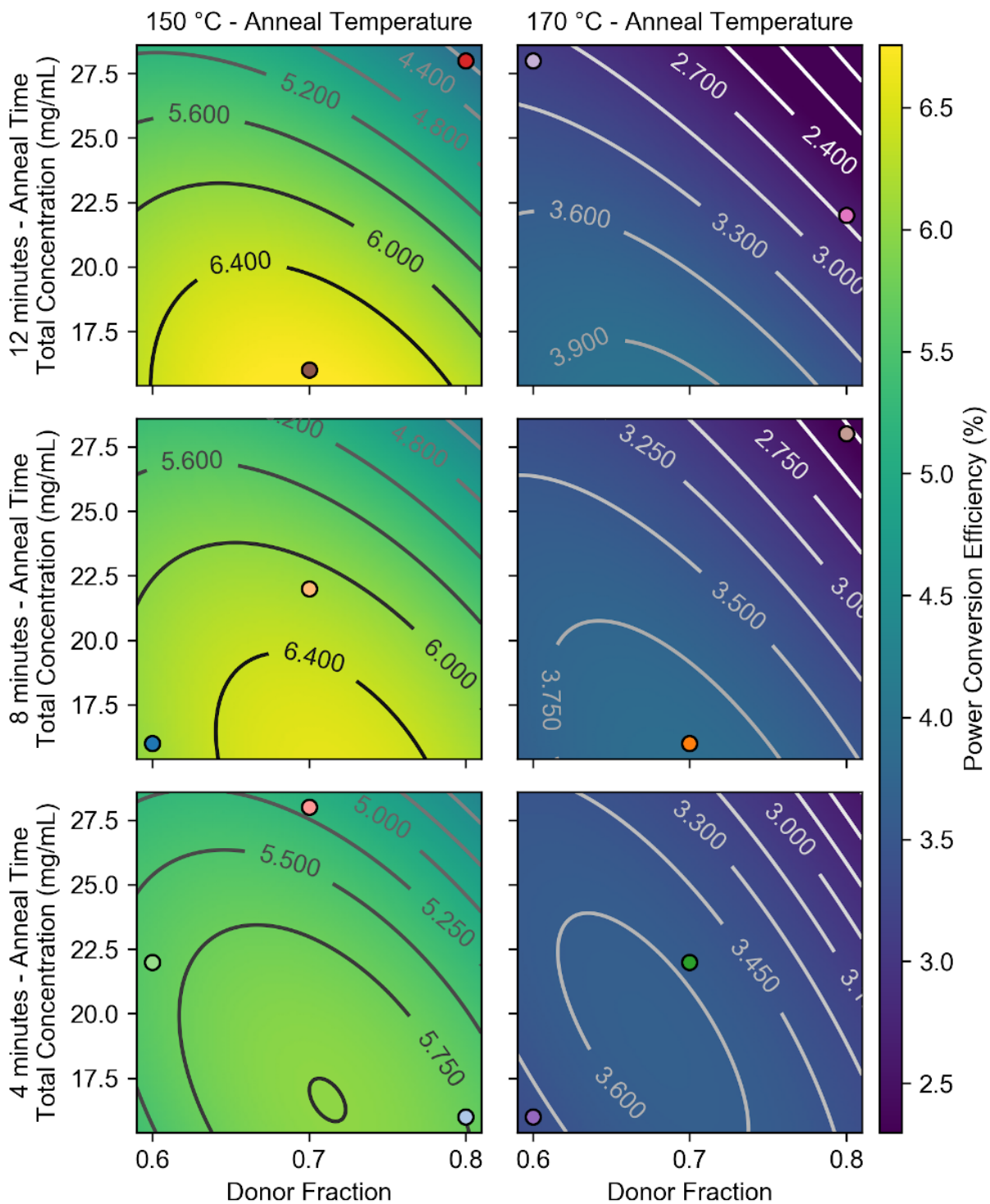


**Figure 2.7:** Maps of PCEs as generated *via* ML methods for the first round of optimization of the devices with BHJs comprising DRCN5T/IT-4F. This set of maps shows the effect of all 4 processing parameters on PCE, with higher areas of PCE represented by yellow, and lower by blue.

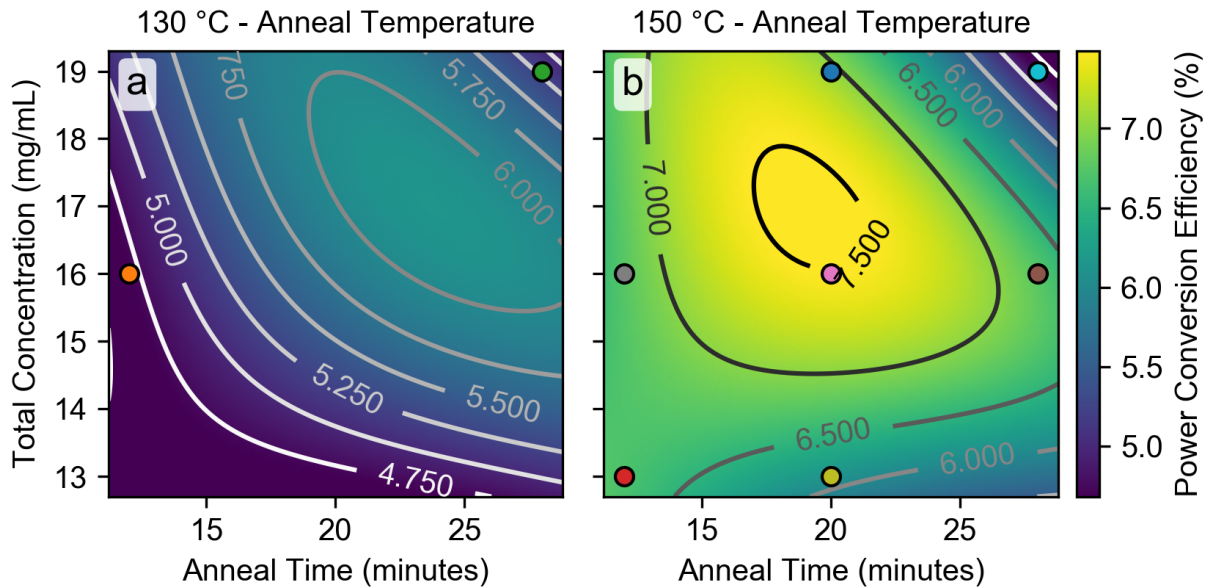


**Figure 2.8:** ML-generated PCE maps for the second round of optimization of devices with BHJs comprising DRCN5T/IT-4F BHJ. This set of maps shows the effect of all 4 processing parameters on PCE with higher PCE areas represented by yellow and lower PCE by blue.

annealing temperature and total concentration of the BHJ precursor solution, respectively. The plots differ in their annealing times, as indicated on each panel. Comparing the two plots in figure 2.8, it is clear that annealing devices at 150 °C resulted in higher efficiency devices than annealing at 130 °C. The ANOVA in figure A.34 labelled PCE shows that annealing temperature indeed has the largest effect on the PCEs, followed by annealing time, and finally by the total concentration of the BHJ solution. Figure A.38 e,g show that both annealing time and total concentration had little effect on the PCE over the ranges tested. Interestingly, an annealing temperature of 150 °C seems required in order to achieve a high shunt resistance in these parameter ranges (figure A.34  $R_{sh}$ ). A similar effect was found for non-optimal donor fractions in the first round of ITIC device optimization (figure A.6  $R_{sh}$ ). The second round of IT-4F optimization yielded the best performing device in this study with a PCE = 7.5%,  $J_{sc}$  = 15.2 mA/cm<sup>2</sup>, FF = 0.62 and a  $V_{oc}$  = 0.80 V. ## What was learned about optimization of OPVs comprising these 3 ITIC derivatives? {#sec:results-learned}

All three of the ITIC derivative-based BHJs exhibited the highest observed performance with a donor-rich BHJ, in the range of 0.7–0.8. It is possible that without a systematic screening process that allows for the exploration of such large parameter spaces, the compositions of BHJs might have been too narrow to have found the islands of higher PCEs greater than a few percent. It has been reported that the donor molecule DRCN5T readily crystallizes upon annealing at 120 °C, which is thought to promote phase segregation and the formation of percolated pathways.<sup>67</sup> ITIC, on the other hand, requires higher temperatures to induce crystallization,<sup>76</sup> and thus higher ideal annealing temperatures, in the range of 160 °C, are considered essential for optimum performance (table A.1).<sup>77</sup> A compromise would be needed when combining these two components, and thus the optimal annealing conditions would be difficult to predict. The identification of different conditions to arrive at optimal performance of these three combinations of BHJs highlights the lack of generality when one embarks upon the optimization of a new BHJ, even when the molecules are structurally related.

**Table 2.2:** Photovoltaic metrics of champion devices after 2 rounds of optimization. Average PCE values and standard deviation in brackets. Averages based on 10, 43 and 35 devices for ITIC, IT-M and IT-4F, respectively.

<b>Acceptor</b>				
<b>Molecule</b>	<b>PCE (%)</b>	<b>J<sub>sc</sub> (mA/cm<sup>2</sup>)</b>	<b>FF</b>	<b>V<sub>oc</sub> (V)</b>
ITIC	4.3 (3.9 ± 0.39)	10.3 (9.9 ± 0.48)	0.43 (0.42 ± 0.022)	0.96 (0.94 ± 0.012)
IT-M	5.9 (5.4 ± 0.69)	12.2 (11.5 ± 0.77)	0.53 (0.50 ± 0.043)	0.93 (0.92 ± 0.024)
IT-4F	7.5 (6.2 ± 0.85)	15.2 (13.5 ± 0.78)	0.62 (0.58 ± 0.049)	0.80 (0.78 ± 0.016)

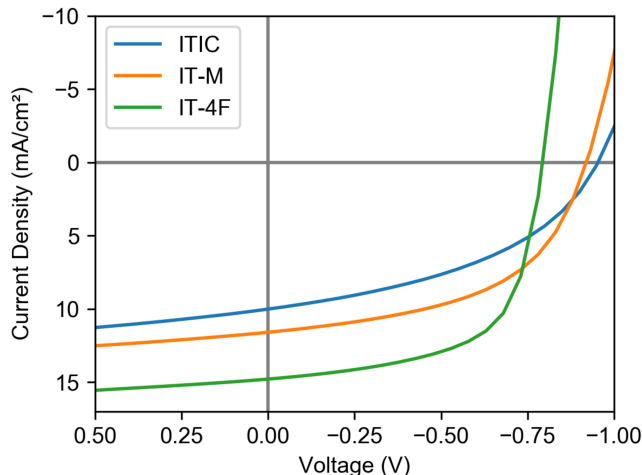


**Figure 2.9:** JV curves of the champion devices for all 3 small-molecule donors that were investigated in this work, ITIC, IT-M, and IT-4F, with the donor DRCN5T. The experimental conditions used to fabricate these champion devices were identified after two rounds of the DOE and ML optimization for each composition.

As expected from their previously measured LUMO levels,<sup>68–70</sup> the  $V_{oc}$  values of champion devices decrease in the order of ITIC ( $\sim 0.98$  V) > IT-M ( $\sim 0.93$  V) > IT-4F ( $\sim 0.80$  V). This admittedly small dataset seems to suggest a trade-off between  $V_{oc}$  and  $J_{sc}$  and FF; similar trade-offs have been previously identified with other small-molecule acceptors by Cheyns *et al.*<sup>75</sup> Additionally, Ma *et al.* found that matching the crystallinity of the donor and acceptor polymers improved device efficiency,<sup>78</sup> and the same phenomenon is likely to hold for small-molecule OPVs as well.

Given that we have very little in the way of mechanistic rationale to link processing parameters with device properties, it is very difficult to know *a priori* what ranges of parameters could lead to the highest device parameters, especially since there is often a non-linear output from a set of multi-dimensional input parameters that have varying degrees of correlation. Moreover, despite small changes in the donor molecular structure, the range of optimal processing conditions changes in unpredictable ways given that these factors are so intertwined and convoluted. These conclusions highlight one of the strengths of this approach to device optimization: while traditional methods

typically sample only a handful of parameters over smaller ranges and test these parameters independently, the DOE-based analyses enable investigation of a broad swath of variables, enabling rational exploration of novel systems with only scant prior knowledge.

## 2.4 Experimental

### 2.4.1 Device Fabrication

The donor and acceptor materials, DRCN5T, ITIC, IT-M and IT-4F were purchased from Ossila, and solvents were purchased from Sigma-Aldrich. All materials and solvents were used as received without further treatment unless otherwise stated. ITO coated glass substrates were purchased from Delta Technologies (8–12  $\Omega$ /sq). ITO glass was sequentially sonicated in dichloromethane, deionized water, and 2-propanol each for 10 min and then dried with an Ar gun (99.998% Ar). The ITO substrates were then cleaned for 10 min in an air plasma with a Harrick plasma cleaner (1.0 torr, PDC 32G, 18W). Zinc acetate dihydrate, ethanolamine and 2-methoxyethanol were purchased from Sigma-Aldrich. ZnO sols were prepared according to prior literature,<sup>79</sup> and the ZnO solution left for 12 hours before the first use. The age of ZnO precursor solution varied from one day to two weeks and within this time frame, no discernible differences in device performance were noted. Both ZnO and BHJ layers were cast using static dispensing from a pipetter with sufficient solution to wet the entire substrate (100  $\mu$ L), followed by spin-casting. After plasma cleaning, the substrates were again cleaned with a stream of Ar and the ZnO layer was then immediately deposited. 120  $\mu$ L of ZnO sol was spin-cast in air for 60 s at a spin speed of 4000 rpm and an acceleration of 900 rpm/s. The cast films were then annealed in air at 200 °C for at least 30 minutes.<sup>79</sup> BHJ precursor solutions (chloroform solvent) containing the donor and acceptor components were prepared in an Ar atmosphere glovebox and heated overnight at 40 °C in sealed amber glass vials with a

teflon cap. The DRCN5T/ITIC BHJ precursor solutions were formulated from concentrated stock solutions of DRCN5T and ITIC in chloroform and diluted to arrive at chloroform solutions of the desired concentration and donor fraction. The DRCN5T/IT-M and DRCN5T/IT-4F solutions used to fabricate were, however, individually prepared by dissolution in chloroform directly (no stock solutions). Before spin-casting, the chloroform solutions were filtered through a 0.22  $\mu\text{m}$  PTFE filter. BHJ films were prepared by spin-casting 100  $\mu\text{L}$  of BHJ solution at 4000 rpm and an acceleration of 900 rpm/s for 30 s onto Ar-cleaned ZnO-coated ITO sheets and were immediately transferred to a glovebox for thermal annealing in an  $\text{N}_2$  atmosphere. Annealing was carried out on a hotplate topped by an aluminum block with a thermocouple insert to ensure accurate temperature and uniform heat distribution. The top electrodes were then deposited as follows: a hole blocking layer of molybdenum oxide (8 nm) and top electrodes comprising Ag (20 nm) and Al (60 nm) were deposited at 0.1, 2.0 and 2.5  $\text{\AA}/\text{s}$ , respectively using thermal evaporation under high-vacuum conditions ( $\sim 5 \times 10^{-6}$  Pa). Device areas were  $0.155 \pm 0.01 \text{ cm}^2$ .

### **2.4.2 Characterization**

Thickness measurements of the BHJ films were performed using a Digital Instruments/Veeco multimode AFM in tapping mode and the resulting data were processed using Gwyddion.<sup>80</sup> PV characteristics were measured at  $\sim 25$   $^\circ\text{C}$  in air under AM 1.5G simulated light (Pico Variable LED source from G2V Optics Inc. at 100  $\text{mW}/\text{cm}^2$  equivalent intensity from 400 nm to 1100 nm) with a light source calibrated as previously described.<sup>52</sup>

### 2.4.3 Machine learning approaches

The machine learning algorithm used was implemented using Scikit-learn, where a standard scalar and a support vector machine (VSM) using a radial basis function (RBF) kernel with an epsilon of  $10^{-5}$ , a tolerance of  $10^{-5}$ , a regularization parameter (C) of 1.0 and gamma values as indicated in (table 2.3).<sup>52</sup>

**Table 2.3:** Compliance values for each round of optimization. Higher values mean more compliant fitting.

Acceptor Molecule	Round 1	Round 2
ITIC	0.08	0.08
IT-M	0.06	0.33
IT-4F	0.03	0.08

# 3

## Conclusion and Future Work

### 3.1 Conclusion

A machine learning based approach was used to optimize devices with small-molecule donor DRCN5T and one of the NFAs, ITIC, IT-M and IT-4F. This method enabled the sampling of large parameter spaces of systems with little to no prior information. The effects of donor fraction, BHJ solution concentration, thermal annealing time and temperature on device performance were

elucidated. Each mixture was very heavy in donor fraction (0.7-0.8) and required thermal annealing in order to exhibit diode behaviour. Thermal annealing at temperatures greater than 120 °C were required in all cases to produce devices with PCEs > 1%. It seems the crystallization of the donor material DRCN5T was critical to the performance of devices. The chemical similarity of the donor and acceptor materials appear to form a highly-intermixed phase whose de-mixing is driven primarily by the crystallization of the donor. This limited device photocurrents and fill factors despite strong absorption of the films. Champion devices for each acceptor material are 4.3, 5.9 and 7.5% for ITIC, IT-M and IT-4F respectively. Higher PCEs for all three mixtures were achieved in the second round of optimization, highlighting the strength of this method when used iteratively.

## 3.2 Future Work

This work serves as an example of this approach to optimizing novel OPV BHJ systems. Given the complexity of an OPV device, there are numerous other parameters that should be optimized, including the interfacial layers and electrodes. This optimization approach can also be considered for most aspects of OPV development, with directions that range from from molecular synthesis to global cost/efficiency relationships.

In this work, standard interfacial layers of MoO<sub>x</sub> and ZnO were used, but there is, however, a growing list of materials that can be used as electron transporting and hole transporting interfacial layers.<sup>81-83</sup> Additionally, there are many different experimental methods for modulating and inducing the ideal nanoscale morphology of the BHJ layers. Solvent vapour annealing (SVA) is heavily employed for this task for BHJs comprising small molecules.<sup>36,70</sup> Typically, the exact experimental parameters for SVA are reported very inconsistently and with significant lack of detail. This situation presents an excellent setting to implement this DOE and ML-based approach method as the parameter space is large and there is some prior knowledge, but none that is

systematic. For example, authors typically only comment on the duration of the SVA step and the solvent used, but the exposure of the BHJ films to the solvent vapour is dependent on (obvious) variables such as the vapour pressure in the chamber, which in turn would depend on a multitude of factors, including surface area of solvent reservoir, volume of the chamber, temperature to name a few. A solvent-flow system<sup>84</sup> would most easily render SVA a reproducible and reliable method for BHJ modification.

Finally, a ML- and DOE-based approach would be useful in matching donor and acceptor materials that have already been synthesized. In light of the amount of resources (including time) and effort directed at designing new materials, testing existing materials with a wider range of components seems promising and easier. Since not all promising donor or acceptor materials prove fruitful in all BHJs, such an approach is important to make such a determination. When the acceptor used in this work, ITIC was paired with the small molecule donor, NDTSR, only devices with PCEs <2.0 % were obtained while devices with the same donor and the ITIC derivative IDIC achieved a PCE > 8.0%.<sup>76</sup> On the other hand, when mixed with other donor materials ITIC can achieve PCEs >11.0% with other donors.<sup>85</sup> Given the wide range of donor and acceptor materials present in the literature, the matching of donor and acceptor components could prove much more useful than synthesizing new materials. Matching materials seem to involve many variables, including the HOMO/LUMO levels, the propensity to crystallize, the solubility, and the absorption ranges all play important roles. Additionally, it is unlikely that all of these variables are independent of one another, and such convolution means that OVAT optimization is likely to miss the true maximum of the system.

# Bibliography

- (1) United Nations. *World Population Prospects Highlights, 2019 Revision Highlights, 2019 Revision*; 2019.
- (2) IEA. *International Energy Outlook 2019*. **2019**, 85.
- (3) Nocera, D. G. On the Future of Global Energy. *Daedalus* **2006**, *135* (4), 112–115. <https://doi.org/10.1162/daed.2006.135.4.112>.
- (4) United Nations. 2015 UN Paris Agreement [https://unfccc.int/files/essential\\_background/convention/application/pdf/english\\_paris\\_agreement.pdf](https://unfccc.int/files/essential_background/convention/application/pdf/english_paris_agreement.pdf) (accessed Jun 18, 2020).
- (5) Solomon, S.; Plattner, G.-K.; Knutti, R.; Friedlingstein, P. Irreversible Climate Change Due to Carbon Dioxide Emissions. *PNAS* **2009**, *106* (6), 1704–1709. <https://doi.org/10.1073/pnas.0812721106>.
- (6) Hofmann, D. J.; Butler, J. H.; Dlugokencky, E. J.; Elkins, J. W.; Masarie, K.; Montzka, S. A.; Tans, P. The Role of Carbon Dioxide in Climate Forcing from 1979 to 2004: Introduction of the Annual Greenhouse Gas Index. *Tellus B: Chemical and Physical Meteorology* **2006**, 58

- (5), 614–619. <https://doi.org/10.1111/j.1600-0889.2006.00201.x>.
- (7) *Climate Change 2014: Mitigation of Climate Change: Working Group III Contribution to the Fifth Assessment Report of the Intergovernmental Panel on Climate Change*; Climate Change, I. P. on, Edenhofer, O., Eds.; Cambridge University Press: New York, NY, 2014.
- (8) Tsao, J.; Lewis, N.; Crabtree, G. Solar FAQs <https://www.sandia.gov/~jytsao/Solar%20FAQs.pdf> (accessed Jun 27, 2020).
- (9) Perez, M.; Perez, R. A Fundamental Look at Supply Side Energy Reserves for the Planet – Update 2015. **2015**, *62*, 4.
- (10) IRENA. *Renewable Power Generation Costs in 2019*; International Renewable Energy Agency: Abu Dhabi, 2020.
- (11) Chapin, D. M.; Fuller, C. S.; Pearson, G. L. A New Silicon P-N Junction Photocell for Converting Solar Radiation into Electrical Power. *Journal of Applied Physics* **1954**, *25* (5), 676–677. <https://doi.org/10.1063/1.1721711>.
- (12) Fraunhofer. Fraunhofer ISE Annual Report 2019/2020 [https://www.ise.fraunhofer.de/content/dam/ise/en/documents/annual\\_reports/fraunhofer-ise-annual-report-2019-2020.pdf](https://www.ise.fraunhofer.de/content/dam/ise/en/documents/annual_reports/fraunhofer-ise-annual-report-2019-2020.pdf) (accessed Jun 28, 2020).
- (13) Meng, L.; Zhang, Y.; Wan, X.; Li, C.; Zhang, X.; Wang, Y.; Ke, X.; Xiao, Z.; Ding, L.; Xia, R.; Yip, H.-L.; Cao, Y.; Chen, Y. Organic and Solution-Processed Tandem Solar Cells with 17.3% Efficiency. *Science* **2018**, eaat2612. <https://doi.org/10.1126/science.aat2612>.
- (14) Yan, T.; Song, W.; Huang, J.; Peng, R.; Huang, L.; Ge, Z. 16.67% Rigid and 14.06% Flexible Organic Solar Cells Enabled by Ternary Heterojunction Strategy. *Adv. Mater.* **2019**, *31* (39), 1902210. <https://doi.org/10.1002/adma.201902210>.
- (15) Graetzel, M.; Janssen, R. A. J.; Mitzi, D. B.; Sargent, E. H. Materials Interface Engineering

- for Solution-Processed Photovoltaics. *Nature* **2012**, 488 (7411, 7411), 304–312. <https://doi.org/10.1038/nature11476>.
- (16) Heeger, A. J. 25th Anniversary Article: Bulk Heterojunction Solar Cells: Understanding the Mechanism of Operation. *Adv. Mater.* **2014**, 26 (1), 10–28. <https://doi.org/10.1002/adma.201304373>.
- (17) Pascual-San-José, E.; Sadoughi, G.; Lucera, L.; Stella, M.; Martínez-Ferrero, E.; Edward Morse, G.; Campoy-Quiles, M.; Burgués-Ceballos, I. Towards Photovoltaic Windows: Scalable Fabrication of Semitransparent Modules Based on Non-Fullerene Acceptors via Laser-Patterning. *J. Mater. Chem. A* **2020**, 8 (19), 9882–9895. <https://doi.org/10.1039/D0TA02994G>.
- (18) Espinosa, N.; Hösel, M.; Angmo, D.; Krebs, F. C. Solar Cells with One-Day Energy Payback for the Factories of the Future. *Energy Environ. Sci.* **2012**, 5 (1), 5117–5132. <https://doi.org/10.1039/C1EE02728J>.
- (19) dos Reis Benatto, G. A.; Roth, B.; Corazza, M.; Søndergaard, R. R.; Gevorgyan, S. A.; Jørgensen, M.; Krebs, F. C. Roll-to-Roll Printed Silver Nanowires for Increased Stability of Flexible ITO-Free Organic Solar Cell Modules. *Nanoscale* **2016**, 8 (1), 318–326. <https://doi.org/10.1039/C5NR07426F>.
- (20) Bartesaghi, D.; Pérez, I. del C.; Kniepert, J.; Roland, S.; Turbiez, M.; Neher, D.; Koster, L. J. A. Competition Between Recombination and Extraction of Free Charges Determines the Fill Factor of Organic Solar Cells. *Nat. Commun.* **2015**, 6 (1), 7083. <https://doi.org/10.1038/ncomms8083>.
- (21) Edwards, T.; Steer, M. Appendix B: Material Properties. In *Foundations for Microstrip Circuit Design*; John Wiley & Sons, Ltd, 2016; pp 635–642. <https://doi.org/10.1002/9781118936160.app2>.

- (22) Hill, I. G.; Kahn, A.; Soos, Z. G.; Pascal, J., R. A. Charge-Separation Energy in Films of  $\pi$ -Conjugated Organic Molecules. *Chemical Physics Letters* **2000**, *327* (3), 181–188. [https://doi.org/10.1016/S0009-2614\(00\)00882-4](https://doi.org/10.1016/S0009-2614(00)00882-4).
- (23) Menke, S. M.; Ran, N. A.; Bazan, G. C.; Friend, R. H. Understanding Energy Loss in Organic Solar Cells: Toward a New Efficiency Regime. *Joule* **2018**, *2* (1), 25–35. <https://doi.org/10.1016/j.joule.2017.09.020>.
- (24) Linderl, T.; Zechel, T.; Brendel, M.; González, D. M.; Müller-Buschbaum, P.; Pflaum, J.; Brütting, W. Energy Losses in Small-Molecule Organic Photovoltaics. *Adv. Energy Mater.* **2017**, *7* (16), 1700237. <https://doi.org/10.1002/aenm.201700237>.
- (25) Wang, H.-J.; Chen, C.-P.; Jeng, R.-J. Polythiophenes Comprising Conjugated Pendants for Polymer Solar Cells: A Review. *Materials* **2014**, *7* (4), 2411–2439. <https://doi.org/10.3390/ma7042411>.
- (26) Yu, G.; Gao, J.; Hummelen, J. C.; Wudl, F.; Heeger, A. J. Polymer Photovoltaic Cells: Enhanced Efficiencies via a Network of Internal Donor-Acceptor Heterojunctions. *Science* **1995**, *270* (5243), 1789–1791. <https://doi.org/10.1126/science.270.5243.1789>.
- (27) Günes, S.; Neugebauer, H.; Sariciftci, N. S. Conjugated Polymer-Based Organic Solar Cells. *Chem. Rev.* **2007**, *107* (4), 1324–1338. <https://doi.org/10.1021/cr050149z>.
- (28) Thompson, B. C.; Fréchet, J. M. J. Polymer–Fullerene Composite Solar Cells. *Angew. Chem. Int. Ed.* **2008**, *47* (1), 58–77. <https://doi.org/10.1002/anie.200702506>.
- (29) Nelson, J. Polymer:Fullerene Bulk Heterojunction Solar Cells. *Materials Today* **2011**, *14* (10), 462–470. [https://doi.org/10.1016/S1369-7021\(11\)70210-3](https://doi.org/10.1016/S1369-7021(11)70210-3).
- (30) Ilmi, R.; Haque, A.; Khan, M. S. High Efficiency Small Molecule-Based Donor Materials for Organic Solar Cells. *Organic Electronics* **2018**, *58*, 53–62. <https://doi.org/10.1016/j>.

orgel.2018.03.048.

- (31) Kan, B.; Zhang, Q.; Li, M.; Wan, X.; Ni, W.; Long, G.; Wang, Y.; Yang, X.; Feng, H.; Chen, Y. Solution-Processed Organic Solar Cells Based on Dialkylthiol-Substituted Benzodithiophene Unit with Efficiency Near 10%. *J. Am. Chem. Soc.* **2014**, *136* (44), 15529–15532. <https://doi.org/10.1021/ja509703k>.
- (32) Zhang, Q.; Kan, B.; Liu, F.; Long, G.; Wan, X.; Chen, X.; Zuo, Y.; Ni, W.; Zhang, H.; Li, M.; Hu, Z.; Huang, F.; Cao, Y.; Liang, Z.; Zhang, M.; Russell, T. P.; Chen, Y. Small-Molecule Solar Cells with Efficiency over 9%. *Nat. Photonics* **2015**, *9* (1), 35–41. <https://doi.org/10.1038/nphoton.2014.269>.
- (33) Li, X.; Wang, Y.; Zhu, Q.; Guo, X.; Ma, W.; Ou, X.; Zhang, M.; Li, Y. A Small Molecule Donor Containing a Non-Fused Ring Core for All-Small-Molecule Organic Solar Cells with High Efficiency over 11%. *J. Mater. Chem. A* **2019**, *7* (8), 3682–3690. <https://doi.org/10.1039/C8TA11441B>.
- (34) Deng, D.; Zhang, Y.; Zhang, J.; Wang, Z.; Zhu, L.; Fang, J.; Xia, B.; Wang, Z.; Lu, K.; Ma, W.; Wei, Z. Fluorination-Enabled Optimal Morphology Leads to over 11% Efficiency for Inverted Small-Molecule Organic Solar Cells. *Nat. Commun.* **2016**, *7* (1), 13740. <https://doi.org/10.1038/ncomms13740>.
- (35) Huo, Y.; Gong, X.-T.; Lau, T.-K.; Xiao, T.; Yan, C.; Lu, X.; Lu, G.; Zhan, X.; Zhang, H.-L. Dual-Accepting-Unit Design of Donor Material for All-Small-Molecule Organic Solar Cells with Efficiency Approaching 11%. *Chem. Mater.* **2018**, *30* (23), 8661–8668. <https://doi.org/10.1021/acs.chemmater.8b03980>.
- (36) Babics, M.; Liang, R.-Z.; Wang, K.; Cruciani, F.; Kan, Z.; Wohlfahrt, M.; Tang, M.-C.; Laquai, F.; Beaujuge, P. M. Solvent Vapor Annealing-Mediated Crystallization Directs Charge Generation, Recombination and Extraction in BHJ Solar Cells. *Chem. Mater.* **2018**,

- 30 (3), 789–798. <https://doi.org/10.1021/acs.chemmater.7b04286>.
- (37) Zhang, G.; Zhao, J.; Chow, P. C. Y.; Jiang, K.; Zhang, J.; Zhu, Z.; Zhang, J.; Huang, F.; Yan, H. Nonfullerene Acceptor Molecules for Bulk Heterojunction Organic Solar Cells. *Chem. Rev.* **2018**, *118* (7), 3447–3507. <https://doi.org/10.1021/acs.chemrev.7b00535>.
- (38) Cheng, P.; Li, G.; Zhan, X.; Yang, Y. Next-Generation Organic Photovoltaics Based on Non-Fullerene Acceptors. *Nat. Photonics* **2018**, *12* (3), 131–142. <https://doi.org/10.1038/s41566-018-0104-9>.
- (39) Luo, Z.; Bin, H.; Liu, T.; Zhang, Z.-G.; Yang, Y.; Zhong, C.; Qiu, B.; Li, G.; Gao, W.; Xie, D.; Wu, K.; Sun, Y.; Liu, F.; Li, Y.; Yang, C. Fine-Tuning of Molecular Packing and Energy Level Through Methyl Substitution Enabling Excellent Small Molecule Acceptors for Nonfullerene Polymer Solar Cells with Efficiency up to 12.54%. *Adv. Mater.* **2018**, *30* (9), 1706124. <https://doi.org/10.1002/adma.201706124>.
- (40) Qiu, B.; Chen, Z.; Qin, S.; Yao, J.; Huang, W.; Meng, L.; Zhu, H.; Yang, Y.; Zhang, Z.-G.; Li, Y. Highly Efficient All-Small-Molecule Organic Solar Cells with Appropriate Active Layer Morphology by Side Chain Engineering of Donor Molecules and Thermal Annealing. *Adv. Mater.* **2020**, *32* (21), 1908373. <https://doi.org/10.1002/adma.201908373>.
- (41) Zhang, W.; Huang, J.; Xu, J.; Han, M.; Su, D.; Wu, N.; Zhang, C.; Xu, A.; Zhan, C. Phthalimide Polymer Donor Guests Enable over 17% Efficient Organic Solar Cells via Parallel-Like Ternary and Quaternary Strategies. *Adv. Energy Mater.* **2020**, *n/a* (n/a), 2001436. <https://doi.org/10.1002/aenm.202001436>.
- (42) Duan, Y.; Xu, X.; Li, Y.; Peng, Q. Recent Development of Perylene Diimide-Based Small Molecular Non-Fullerene Acceptors in Organic Solar Cells. *Chinese Chemical Letters* **2017**, *28* (11), 2105–2115. <https://doi.org/10.1016/j.cclet.2017.08.025>.

- (43) Hou, J.; Inganäs, O.; Friend, R. H.; Gao, F. Organic Solar Cells Based on Non-Fullerene Acceptors. *Nat. Mater.* **2018**, *17* (2), 119–128. <https://doi.org/10.1038/nmat5063>.
- (44) Huo, Y.; Zhang, H.-L.; Zhan, X. Nonfullerene All-Small-Molecule Organic Solar Cells. *ACS Energy Lett.* **2019**, *4* (6), 1241–1250. <https://doi.org/10.1021/acsenergylett.9b00528>.
- (45) Baran, D.; Kirchartz, T.; Wheeler, S.; Dimitrov, S.; Abdelsamie, M.; Gorman, J.; Ashraf, R. S.; Holliday, S.; Wadsworth, A.; Gasparini, N.; Kaienburg, P.; Yan, H.; Amassian, A.; Brabec, C. J.; Durrant, J. R.; McCulloch, I. Reduced Voltage Losses Yield 10% Efficient Fullerene Free Organic Solar Cells with >1 V Open Circuit Voltages. *Energy Environ. Sci.* **2016**, *9* (12), 3783–3793. <https://doi.org/10.1039/C6EE02598F>.
- (46) Bin, H.; Zhang, Z.-G.; Gao, L.; Chen, S.; Zhong, L.; Xue, L.; Yang, C.; Li, Y. Non-Fullerene Polymer Solar Cells Based on Alkylthio and Fluorine Substituted 2D-Conjugated Polymers Reach 9.5% Efficiency. *J. Am. Chem. Soc.* **2016**, *138* (13), 4657–4664. <https://doi.org/10.1021/jacs.6b01744>.
- (47) Ge, J.; Xie, L.; Peng, R.; Fanady, B.; Huang, J.; Song, W.; Yan, T.; Zhang, W.; Ge, Z. 13.34 % Efficiency Non-Fullerene All-Small-Molecule Organic Solar Cells Enabled by Modulating the Crystallinity of Donors via a Fluorination Strategy. *Angew. Chem. Int. Ed.* **2020**, *59* (7), 2808–2815. <https://doi.org/10.1002/anie.201910297>.
- (48) He, X.; Cao, B.; Hauger, T. C.; Kang, M.; Gusarov, S.; Lubner, E. J.; Buriak, J. M. Donor–Acceptor Small Molecules for Organic Photovoltaics: Single-Atom Substitution (Se or S). *ACS Appl. Mater. Interfaces* **2015**, *7* (15), 8188–8199. <https://doi.org/10.1021/acsaami.5b01063>.
- (49) Ye, L.; Collins, B. A.; Jiao, X.; Zhao, J.; Yan, H.; Ade, H. Miscibility-Function Relations in Organic Solar Cells: Significance of Optimal Miscibility in Relation to Percolation. *Adv.*

- Energy Mater.* **2018**, *8* (28), 1703058. <https://doi.org/10.1002/aenm.201703058>.
- (50) Leardi, R. Experimental Design in Chemistry: A Tutorial. *Anal. Chim. Acta* **2009**, *652* (1), 161–172. <https://doi.org/10.1016/j.aca.2009.06.015>.
- (51) Jia, X.; Lynch, A.; Huang, Y.; Danielson, M.; Lang'at, I.; Milder, A.; Ruby, A. E.; Wang, H.; Friedler, S. A.; Norquist, A. J.; Schrier, J. Anthropogenic Biases in Chemical Reaction Data Hinder Exploratory Inorganic Synthesis. *Nature* **2019**, *573* (7773, 7773), 251–255. <https://doi.org/10.1038/s41586-019-1540-5>.
- (52) Cao, B.; Adutwum, L. A.; Oliynyk, A. O.; Lubner, E. J.; Olsen, B. C.; Mar, A.; Buriak, J. M. How to Optimize Materials and Devices *via* Design of Experiments and Machine Learning: Demonstration Using Organic Photovoltaics. *ACS Nano* **2018**, *12* (8), 7434–7444. <https://doi.org/10.1021/acsnano.8b04726>.
- (53) Lee, M.-H. Insights from Machine Learning Techniques for Predicting the Efficiency of Fullerene Derivatives-Based Ternary Organic Solar Cells at Ternary Blend Design. *Adv. Energy Mater.* **2019**, *9* (26), 1900891. <https://doi.org/10.1002/aenm.201900891>.
- (54) Sun, W.; Zheng, Y.; Yang, K.; Zhang, Q.; Shah, A. A.; Wu, Z.; Sun, Y.; Feng, L.; Chen, D.; Xiao, Z.; Lu, S.; Li, Y.; Sun, K. Machine Learning–Assisted Molecular Design and Efficiency Prediction for High-Performance Organic Photovoltaic Materials. *Sci. Adv.* **2019**, *5* (11), eaay4275. <https://doi.org/10.1126/sciadv.aay4275>.
- (55) Padula, D.; Simpson, J. D.; Troisi, A. Combining Electronic and Structural Features in Machine Learning Models to Predict Organic Solar Cells Properties. *Mater. Horiz.* **2019**, *6* (2), 343–349. <https://doi.org/10.1039/C8MH01135D>.
- (56) Lopez, S. A.; Sanchez-Lengeling, B.; Soares, J. de G.; Aspuru-Guzik, A. Design Principles and Top Non-Fullerene Acceptor Candidates for Organic Photovoltaics. *Joule* **2017**, *1* (4),

857–870. <https://doi.org/10.1016/j.joule.2017.10.006>.

- (57) Brown, K. A.; Brittan, S.; Maccaferri, N.; Jariwala, D.; Celano, U. Machine Learning in Nanoscience: Big Data at Small Scales. *Nano Lett.* **2020**, *20* (1), 2–10. <https://doi.org/10.1021/acs.nanolett.9b04090>.
- (58) MacLeod, B. P.; Parlane, F. G. L.; Morrissey, T. D.; Häse, F.; Roch, L. M.; Dettelbach, K. E.; Moreira, R.; Yunker, L. P. E.; Rooney, M. B.; Deeth, J. R.; Lai, V.; Ng, G. J.; Situ, H.; Zhang, R. H.; Elliott, M. S.; Haley, T. H.; Dvorak, D. J.; Aspuru-Guzik, A.; Hein, J. E.; Berlinguette, C. P. Self-Driving Laboratory for Accelerated Discovery of Thin-Film Materials. *Sci. Adv.* **2020**, *6* (20), eaaz8867. <https://doi.org/10.1126/sciadv.aaz8867>.
- (59) Mora-Tamez, L.; Barim, G.; Downes, C.; Williamson, E. M.; Habas, S. E.; Brutchey, R. L. Controlled Design of Phase- and Size-Tunable Monodisperse Ni<sub>2</sub>P Nanoparticles in a Phosphonium-Based Ionic Liquid Through Response Surface Methodology. *Chem. Mater.* **2019**, *31* (5), 1552–1560. <https://doi.org/10.1021/acs.chemmater.8b04518>.
- (60) Voznyy, O.; Levina, L.; Fan, J. Z.; Askerka, M.; Jain, A.; Choi, M.-J.; Ouellette, O.; Todorović, P.; Sagar, L. K.; Sargent, E. H. Machine Learning Accelerates Discovery of Optimal Colloidal Quantum Dot Synthesis. *ACS Nano* **2019**, *13* (10), 11122–11128. <https://doi.org/10.1021/acsnano.9b03864>.
- (61) Wei, L.; Xu, X.; Gurudayal; Bullock, J.; Ager, J. W. Machine Learning Optimization of P-Type Transparent Conducting Films. *Chem. Mater.* **2019**, *31* (18), 7340–7350. <https://doi.org/10.1021/acs.chemmater.9b01953>.
- (62) Häse, F.; Roch, L. M.; Kreisbeck, C.; Aspuru-Guzik, A. Phoenix: A Bayesian Optimizer for Chemistry. *ACS Cent. Sci.* **2018**, *4* (9), 1134–1145. <https://doi.org/10.1021/acscentsci.8b00307>.

- (63) Wang, K.; Liu, C.; Meng, T.; Yi, C.; Gong, X. Inverted Organic Photovoltaic Cells. *Chem. Soc. Rev.* **2016**, *45* (10), 2937–2975. <https://doi.org/10.1039/C5CS00831J>.
- (64) Ge, J.; Wei, Q.; Peng, R.; Zhou, E.; Yan, T.; Song, W.; Zhang, W.; Zhang, X.; Jiang, S.; Ge, Z. Improved Efficiency in All-Small-Molecule Organic Solar Cells with Ternary Blend of Nonfullerene Acceptor and Chlorinated and Nonchlorinated Donors. *ACS Appl. Mater. Interfaces* **2019**, *11* (47), 44528–44535. <https://doi.org/10.1021/acsami.9b16900>.
- (65) Qiu, B.; Xue, L.; Yang, Y.; Bin, H.; Zhang, Y.; Zhang, C.; Xiao, M.; Park, K.; Morrison, W.; Zhang, Z.-G.; Li, Y. All-Small-Molecule Nonfullerene Organic Solar Cells with High Fill Factor and High Efficiency over 10%. *Chem. Mater.* **2017**, *29* (17), 7543–7553. <https://doi.org/10.1021/acs.chemmater.7b02536>.
- (66) Zhou, R.; Jiang, Z.; Yang, C.; Yu, J.; Feng, J.; Adil, M. A.; Deng, D.; Zou, W.; Zhang, J.; Lu, K.; Ma, W.; Gao, F.; Wei, Z. All-Small-Molecule Organic Solar Cells with over 14% Efficiency by Optimizing Hierarchical Morphologies. *Nat. Commun.* **2019**, *10* (1), 5393. <https://doi.org/10.1038/s41467-019-13292-1>.
- (67) Kan, B.; Li, M.; Zhang, Q.; Liu, F.; Wan, X.; Wang, Y.; Ni, W.; Long, G.; Yang, X.; Feng, H.; Zuo, Y.; Zhang, M.; Huang, F.; Cao, Y.; Russell, T. P.; Chen, Y. A Series of Simple Oligomer-Like Small Molecules Based on Oligothiophenes for Solution-Processed Solar Cells with High Efficiency. *J. Am. Chem. Soc.* **2015**, *137* (11), 3886–3893. <https://doi.org/10.1021/jacs.5b00305>.
- (68) Lin, Y.; Wang, J.; Zhang, Z.-G.; Bai, H.; Li, Y.; Zhu, D.; Zhan, X. An Electron Acceptor Challenging Fullerenes for Efficient Polymer Solar Cells. *Adv. Mater.* **2015**, *27* (7), 1170–1174. <https://doi.org/10.1002/adma.201404317>.
- (69) Li, S.; Ye, L.; Zhao, W.; Zhang, S.; Mukherjee, S.; Ade, H.; Hou, J. Energy-Level Modulation of Small-Molecule Electron Acceptors to Achieve over 12% Efficiency in Polymer Solar Cells.

- Adv. Mater.* **2016**, 28 (42), 9423–9429. <https://doi.org/10.1002/adma.201602776>.
- (70) Zhao, W.; Li, S.; Yao, H.; Zhang, S.; Zhang, Y.; Yang, B.; Hou, J. Molecular Optimization Enables over 13% Efficiency in Organic Solar Cells. *J. Am. Chem. Soc.* **2017**, 139 (21), 7148–7151. <https://doi.org/10.1021/jacs.7b02677>.
- (71) Wang, J.-C.; Weng, W.-T.; Tsai, M.-Y.; Lee, M.-K.; Horng, S.-F.; Perng, T.-P.; Kei, C.-C.; Yu, C.-C.; Meng, H.-F. Highly Efficient Flexible Inverted Organic Solar Cells Using Atomic Layer Deposited ZnO as Electron Selective Layer. *J. Mater. Chem.* **2010**, 20 (5), 862–866. <https://doi.org/10.1039/B921396A>.
- (72) Daughton, W. J. An Investigation of the Thickness Variation of Spun-on Thin Films Commonly Associated with the Semiconductor Industry. *J. Electrochem. Soc.* **1982**, 129 (1), 173. <https://doi.org/10.1149/1.2123749>.
- (73) Surowiec, I.; Vikström, L.; Hector, G.; Johansson, E.; Vikström, C.; Trygg, J. Generalized Subset Designs in Analytical Chemistry. *Anal. Chem.* **2017**, 89 (12), 6491–6497. <https://doi.org/10.1021/acs.analchem.7b00506>.
- (74) Brabec, C. J.; Cravino, A.; Meissner, D.; Sariciftci, N. S.; Fromherz, T.; Rispe, M. T.; Sanchez, L.; Hummelen, J. C. Origin of the Open Circuit Voltage of Plastic Solar Cells. *Adv. Funct. Mater.* **2001**, No. 5, 7.
- (75) Cnops, K.; Zango, G.; Genoe, J.; Heremans, P.; Martinez-Diaz, M. V.; Torres, T.; Cheyns, D. Energy Level Tuning of Non-Fullerene Acceptors in Organic Solar Cells. *J. Am. Chem. Soc.* **2015**, 137 (28), 8991–8997. <https://doi.org/10.1021/jacs.5b02808>.
- (76) Li, H.; Zhao, Y.; Fang, J.; Zhu, X.; Xia, B.; Lu, K.; Wang, Z.; Zhang, J.; Guo, X.; Wei, Z. Improve the Performance of the All-Small-Molecule Nonfullerene Organic Solar Cells Through Enhancing the Crystallinity of Acceptors. *Adv. Energy Mater.* **2018**, 8 (11),

1702377. <https://doi.org/10.1002/aenm.201702377>.
- (77) Yu, L.; Qian, D.; Marina, S.; Nugroho, F. A. A.; Sharma, A.; Hultmark, S.; Hofmann, A. I.; Kroon, R.; Benduhn, J.; Smilgies, D.-M.; Vandewal, K.; Andersson, M. R.; Langhammer, C.; Martín, J.; Gao, F.; Müller, C. Diffusion-Limited Crystallization: A Rationale for the Thermal Stability of Non-Fullerene Solar Cells. *ACS Appl. Mater. Interfaces* **2019**, *11* (24), 21766–21774. <https://doi.org/10.1021/acsami.9b04554>.
- (78) Shi, S.; Yuan, J.; Ding, G.; Ford, M.; Lu, K.; Shi, G.; Sun, J.; Ling, X.; Li, Y.; Ma, W. Improved All-Polymer Solar Cell Performance by Using Matched Polymer Acceptor. *Adv. Funct. Mater.* **2016**, *26* (31), 5669–5678. <https://doi.org/10.1002/adfm.201601037>.
- (79) Sun, Y.; Seo, J. H.; Takacs, C. J.; Seifert, J.; Heeger, A. J. Inverted Polymer Solar Cells Integrated with a Low-Temperature-Annealed Sol-Gel-Derived ZnO Film as an Electron Transport Layer. *Adv. Mater.* **2011**, *23* (14), 1679–1683. <https://doi.org/10.1002/adma.201004301>.
- (80) Nečas, D.; Klapetek, P. Gwyddion: An Open-Source Software for SPM Data Analysis. *Cent. Eur. J. Phys.* **2012**, *10* (1), 181–188. <https://doi.org/10.2478/s11534-011-0096-2>.
- (81) Zhang, Z.-G.; Qi, B.; Jin, Z.; Chi, D.; Qi, Z.; Li, Y.; Wang, J. Perylene Diimides: A Thickness-Insensitive Cathode Interlayer for High Performance Polymer Solar Cells. *Energy Environ. Sci.* **2014**, *7* (6), 1966. <https://doi.org/10.1039/c4ee00022f>.
- (82) He, Z.; Zhong, C.; Huang, X.; Wong, W.-Y.; Wu, H.; Chen, L.; Su, S.; Cao, Y. Simultaneous Enhancement of Open-Circuit Voltage, Short-Circuit Current Density, and Fill Factor in Polymer Solar Cells. *Adv. Mater.* **2011**, *23* (40), 4636–4643. <https://doi.org/10.1002/adma.201103006>.
- (83) Yin, Z.; Wei, J.; Zheng, Q. Interfacial Materials for Organic Solar Cells: Recent Advances

and Perspectives. *Adv. Sci.* **2016**, 3 (8), 1500362. <https://doi.org/10.1002/adv.201500362>.

(84) Zomeran, D.; Kong, J.; McAfee, S. M.; Welch, G. C.; Kelly, T. L. Control and Characterization of Organic Solar Cell Morphology Through Variable-Pressure Solvent Vapor Annealing. *ACS Appl. Energy Mater.* **2018**, 1 (10), 5663–5674. <https://doi.org/10.1021/acsaem.8b01214>.

(85) Bin, H.; Gao, L.; Zhang, Z.-G.; Yang, Y.; Zhang, Y.; Zhang, C.; Chen, S.; Xue, L.; Yang, C.; Xiao, M.; Li, Y. 11.4% Efficiency Non-Fullerene Polymer Solar Cells with Trialkylsilyl Substituted 2D-Conjugated Polymer as Donor. *Nat. Commun.* **2016**, 7 (1, 1), 13651. <https://doi.org/10.1038/ncomms13651>.

# A

## Appendix

### **A.1 Explanation of the integer reduction of the GSD.**

If the integer reduction becomes sufficiently large, however, it is no longer possible to always have the same number of experiments done at each level. The degree of non-uniformity in sampling each level is used as a metric to help choose what integer number of experiments should be chosen. Specifically, for every level of integer reduction, the polydispersity of the levels for each parameter

is measured, which is defined as the standard deviation in the number of times a level is sampled, divided by the mean number of times a level is sampled. It was found that increasing the integer reduction in the number of experiments as much as possible, while maintaining a polydispersity of the levels for all parameters below 20%, was a generally useful cutoff that would yield a trackable number of experiments while still providing a reasonable sampling of the parameter space. The resulting list of prescribed devices is shown in figure A.3 a).

## A.2 Additional Figures

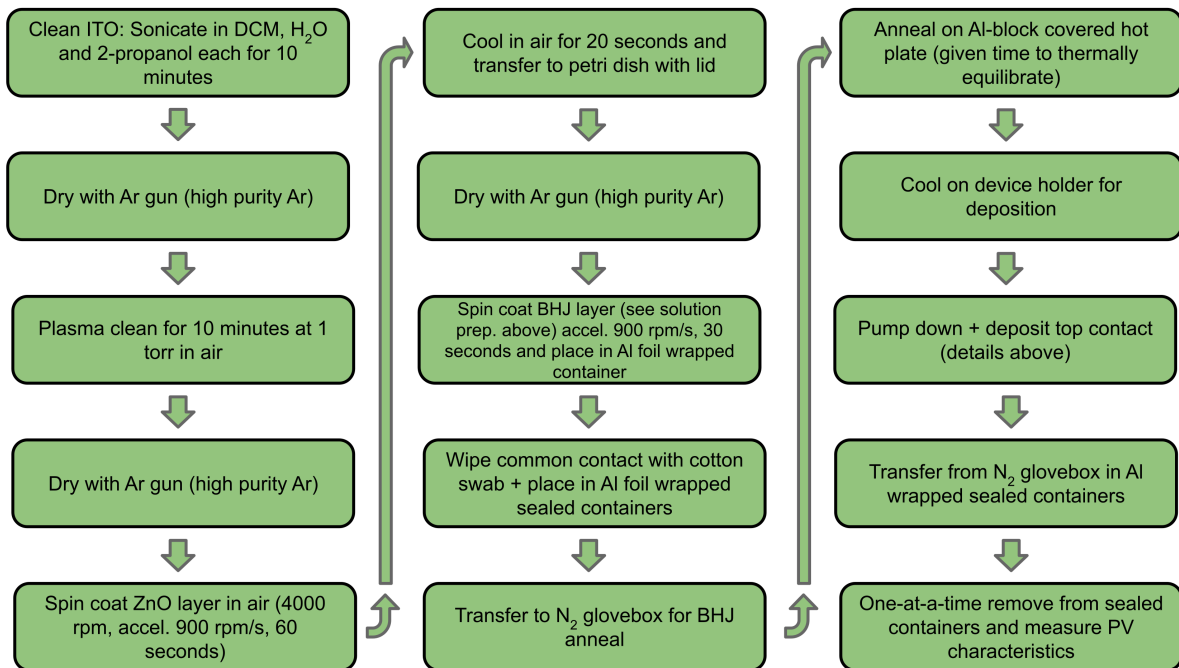


**Figure A.1:** Device fabrication flowchart. Care was taken to ensure the cleanliness of the substrates prior to and following deposition of all layers. As shown in the following figure, imperfections in the BHJ were often noted (BHJ on the left with slight streaking), which necessitated fabrication of duplicates.

**Table A.1:** Processing parameters yielding champion devices after two rounds of optimization. \*ITIC-containing BHJs were prepared from concentrated solutions of DRCN5T (24 mg/mL) and ITIC (11 mg/mL), BHJ spin speed = 4000 rpm; \*\* BHJ spin speed 4000 rpm; †BHJ spin speed = 2000 rpm. Champion average thicknesses of ITIC = 133 nm, IT-M = 148 nm, IT-4F = 89 nm.

Acceptor Molecule	Total		Annealing	
	Concentration	Donor Fraction	Temperature (°C)	Annealing Time (min)
ITIC	17*	0.75	140	4
IT-M	22**	0.7	160	8
IT-4F	16†	0.7	150	20

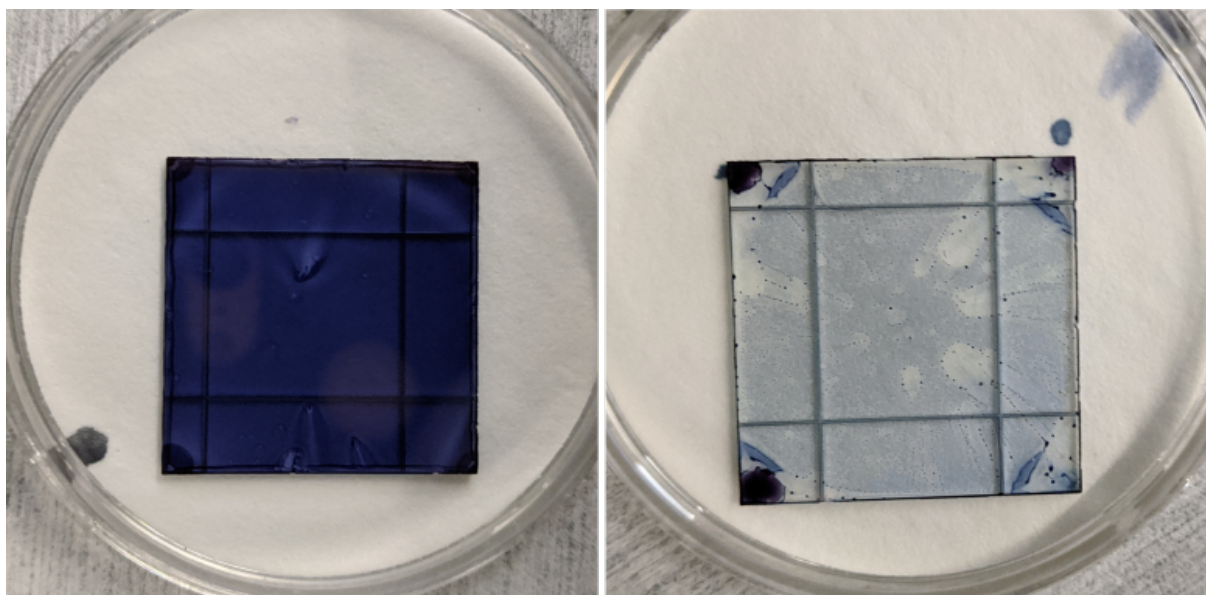


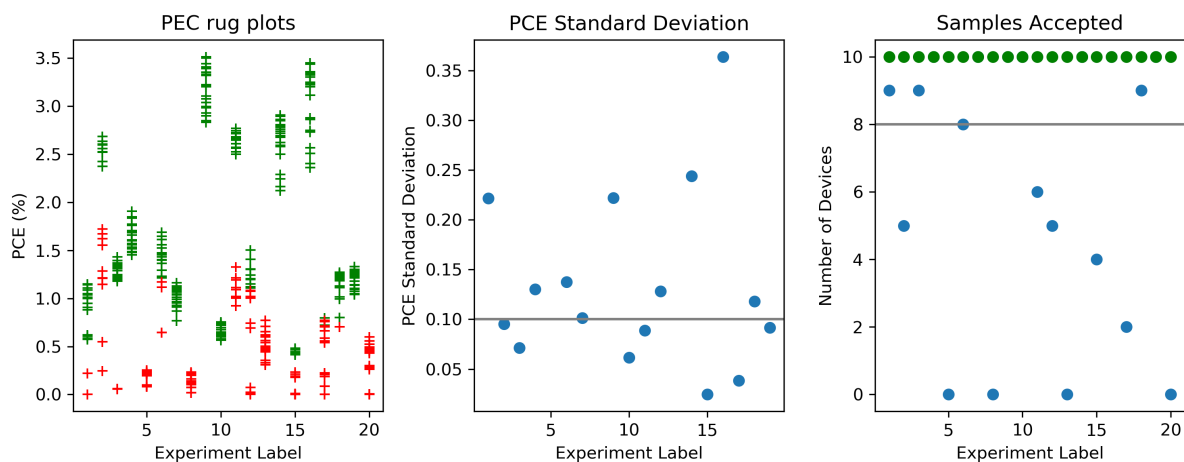
**Figure A.2:** BHJ films with the same concentration spin-cast onto a layer of ZnO/ITO from chloroform and from 1,2-dichlorobenzene, left and right respectively. Films cast from 1,2-dichlorobenzene show poor wettability and thus chloroform was chosen as the spin-casting solvent throughout this work.

ITIC Round 1					ITIC Round 2				
BHJ Conc. (mg/ml)	5	7.5	10	12.5	BHJ Conc. (mg/ml)	8	11	14	17
# of expts	4	6	6	4	# of expts	6	4	6	4
Donor Fraction	0.6	0.7	0.8	0.9	Donor Fraction	0.65	0.75	0.85	
# of expts	4	6	6	4	# of expts	7	7	6	
Annealing Temp. (°C)	120	140	160		Annealing Temp. (°C)	130	140	150	
# of expts	7	6	7		# of expts	7	6	7	
Annealing Time (sec)	100	200	300		Annealing Time (minutes)	90	240	390	
# of expts	7	6	7		# of expts	7	7	6	

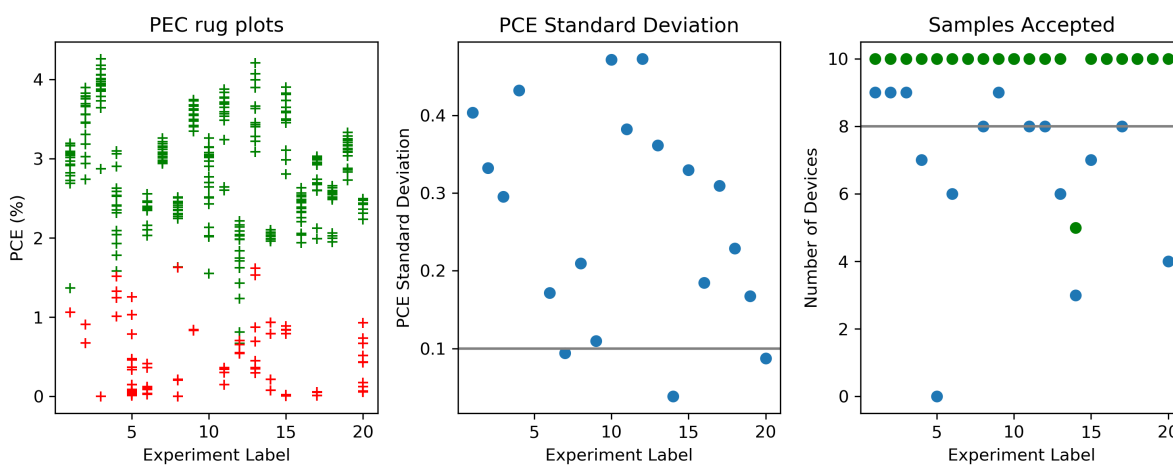
  

Exp't #	BHJ conc. mg/mL	Donor Fraction	Ann. Temp °C	Ann. Time seconds	Exp't #	BHJ conc. mg/mL	Donor Fraction	Ann. Temp °C	Ann. Time minutes
1	7.5	0.7	120	100	1	14	0.65	150	1.5
2	10	0.8	120	100	2	14	0.75	130	1.5
3	10	0.9	140	100	3	17	0.75	140	4
4	7.5	0.7	140	200	4	8	0.65	150	4
5	5	0.6	120	300	5	8	0.85	150	6.5
6	7.5	0.9	120	300	6	8	0.85	140	4
7	12.5	0.9	160	100	7	8	0.75	130	4
8	7.5	0.6	120	200	8	17	0.85	150	4
9	10	0.8	140	200	9	17	0.75	150	6.5
10	10	0.9	160	200	10	11	0.85	130	1.5
11	12.5	0.8	160	200	11	8	0.75	150	1.5
12	7.5	0.7	160	300	12	11	0.65	130	6.5
13	5	0.8	160	100	13	11	0.75	150	4
14	10	0.8	160	300	14	14	0.65	130	4
15	7.5	0.6	140	300	15	8	0.75	140	6.5
16	12.5	0.8	140	100	16	11	0.65	140	1.5
17	5	0.7	140	300	17	14	0.65	140	6.5
18	12.5	0.7	120	300	18	17	0.65	130	1.5
19	10	0.6	160	100	19	14	0.85	140	1.5
20	5	0.7	120	200	20	14	0.85	130	6.5

**Figure A.3:** Tabulation of the processing parameter levels, number of experiments at each level and list of experiments for the first and second round of optimization of the DRCN5T/ITIC BHJ blend.



**Figure A.4:** Plots the performance of devices that were accepted (green) and rejected (red), and the standard deviation of devices and the number of devices accepted for each experimental condition for the first round of DRCN5T/ITIC BHJ blend optimization.



**Figure A.5:** Plots showing performance of devices that were accepted (green) and rejected (red), and the standard deviation of devices and the number of devices accepted for each experimental condition for the second round of DRCN5T/ITIC BHJ blend optimization.

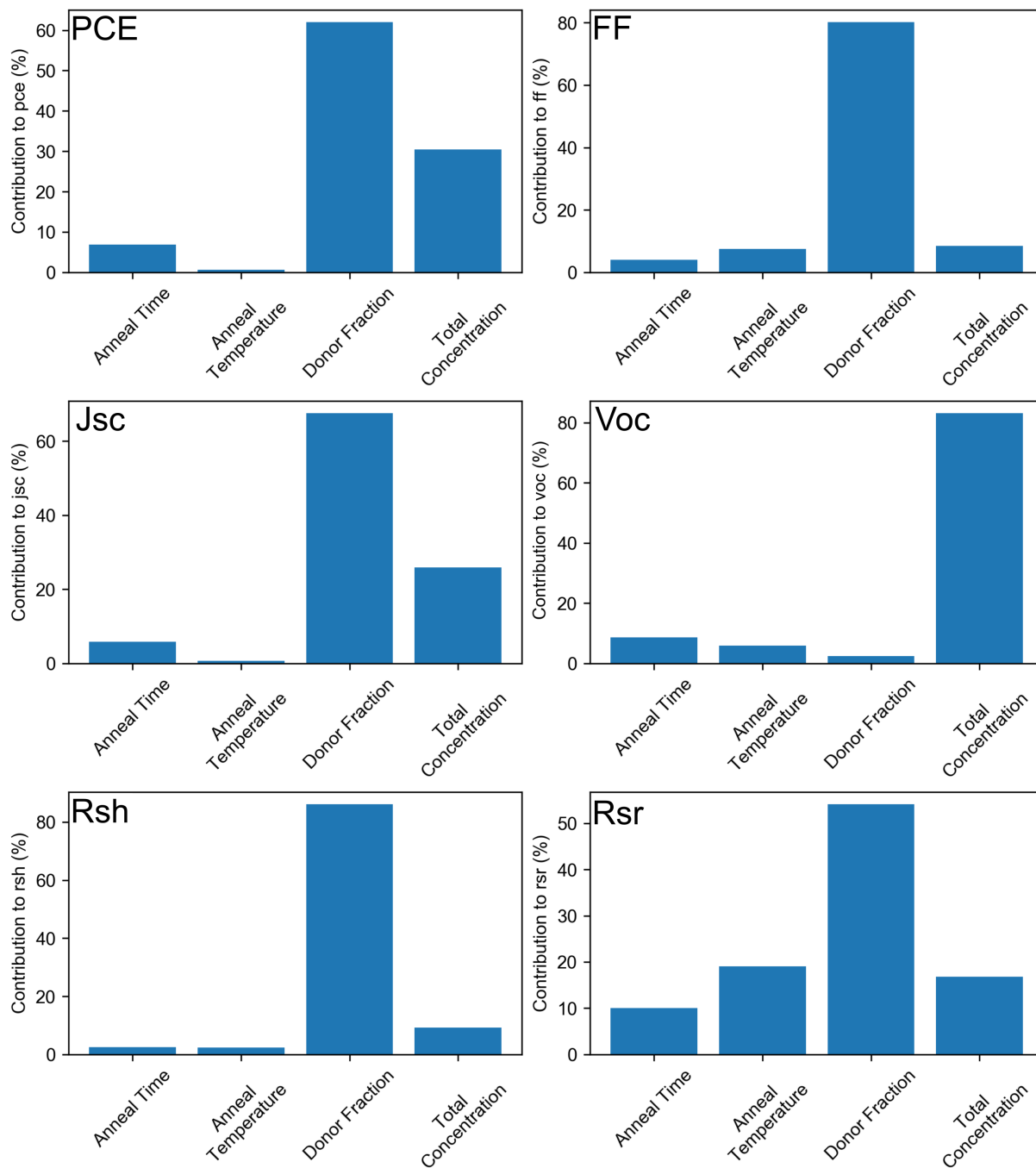


**Figure A.6:** ANOVAs of the relative contribution of the processing parameters on PCE, FF,  $J_{sc}$ ,  $V_{oc}$ ,  $R_{sh}$  and  $R_{sr}$  for the first round of DRCN5T/ITIC BHJ blend optimization.

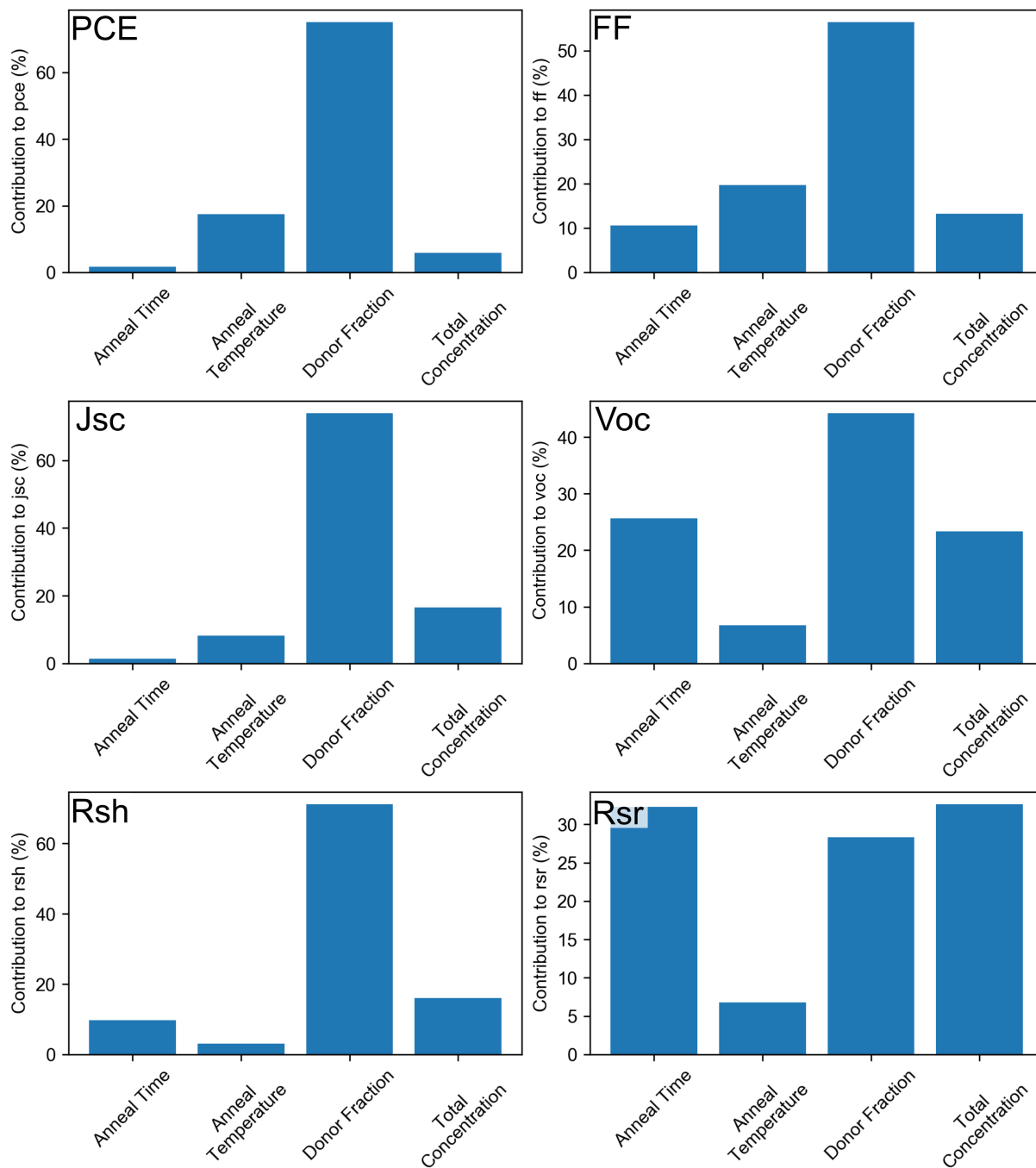


**Figure A.7:** ANOVAs of the relative contribution of the processing parameters on PCE, FF,  $J_{sc}$ ,  $V_{oc}$ ,  $R_{sh}$  and  $R_{sr}$  for the second round of DRCN5T/ITIC BHJ blend optimization.

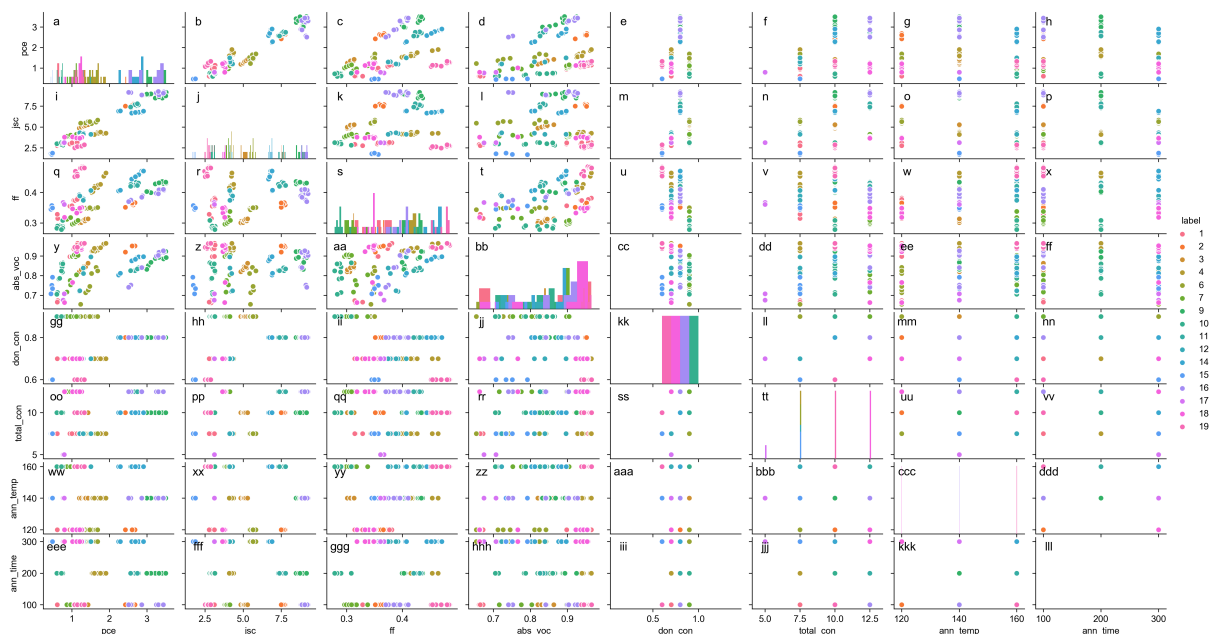


**Figure A.8:** Pair plots comparing processing parameters to PCE,  $J_{sc}$ , FF or  $V_{oc}$ , for the first round of DRCN5T/ITIC BHJ blend optimization.

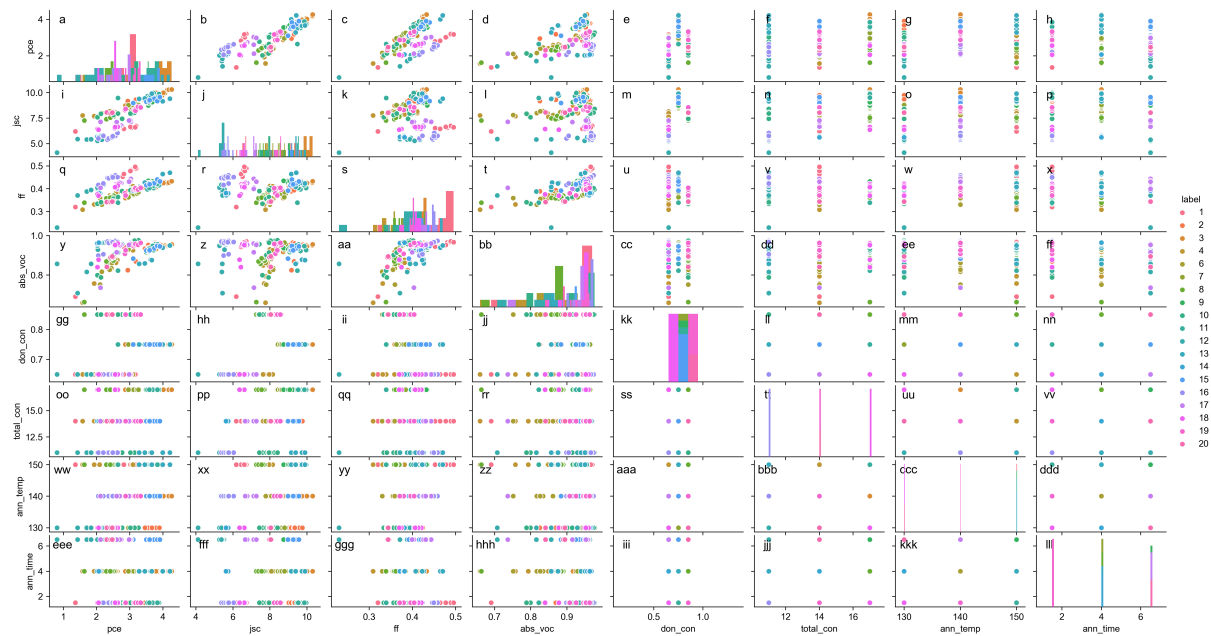


**Figure A.9:** Pair plots comparing processing parameters to PCE,  $J_{sc}$ , FF or  $V_{oc}$ , for the second round of DRCN5T/ITIC BHJ blend optimization.

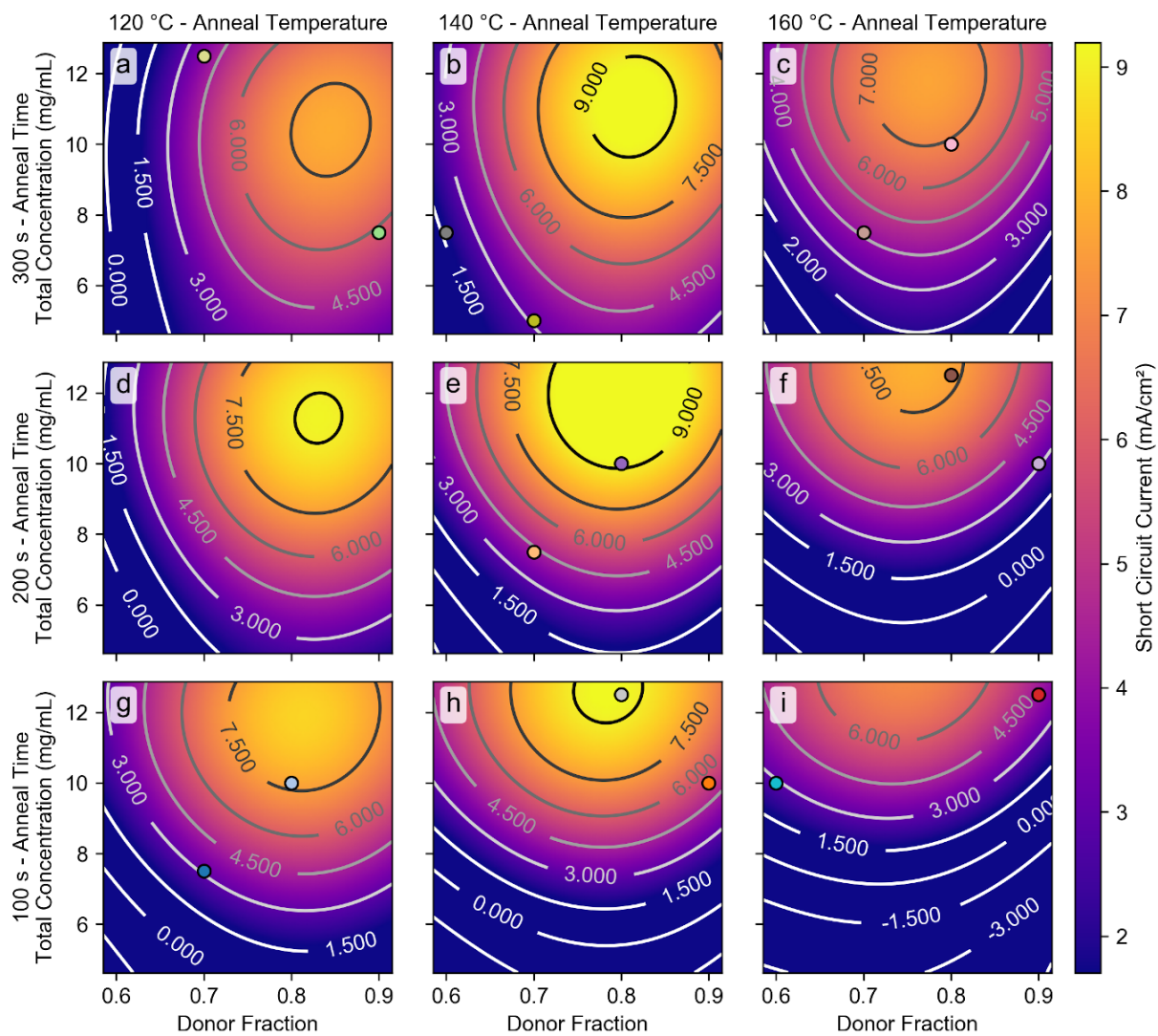


**Figure A.10:** ML-generated  $J_{sc}$  map for the first round of DRCN5T/ITIC BHJ blend optimization.



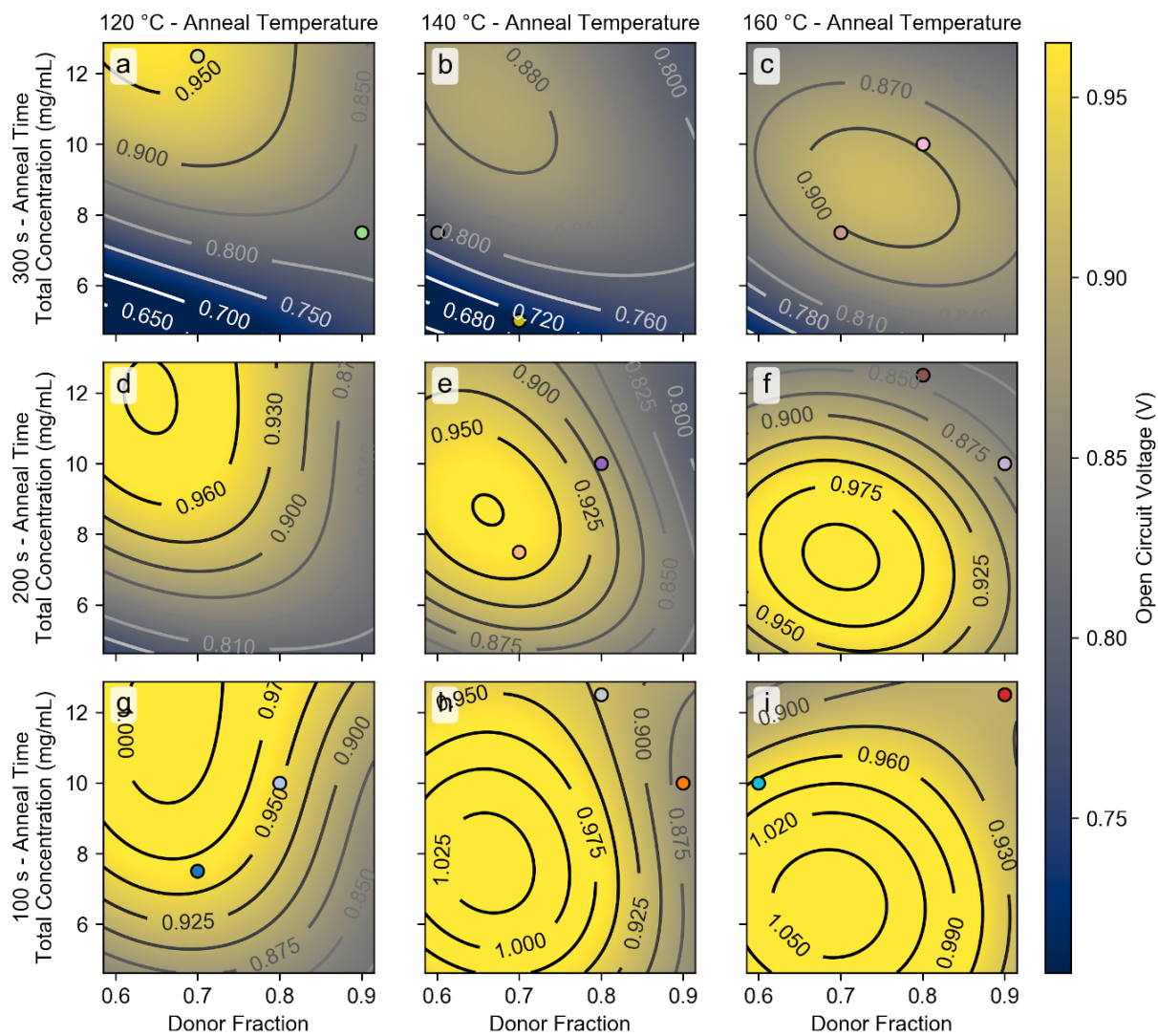


**Figure A.12:** ML-generated  $V_{oc}$  map for the first round of DRCN5T/ITIC BHJ blend optimization.

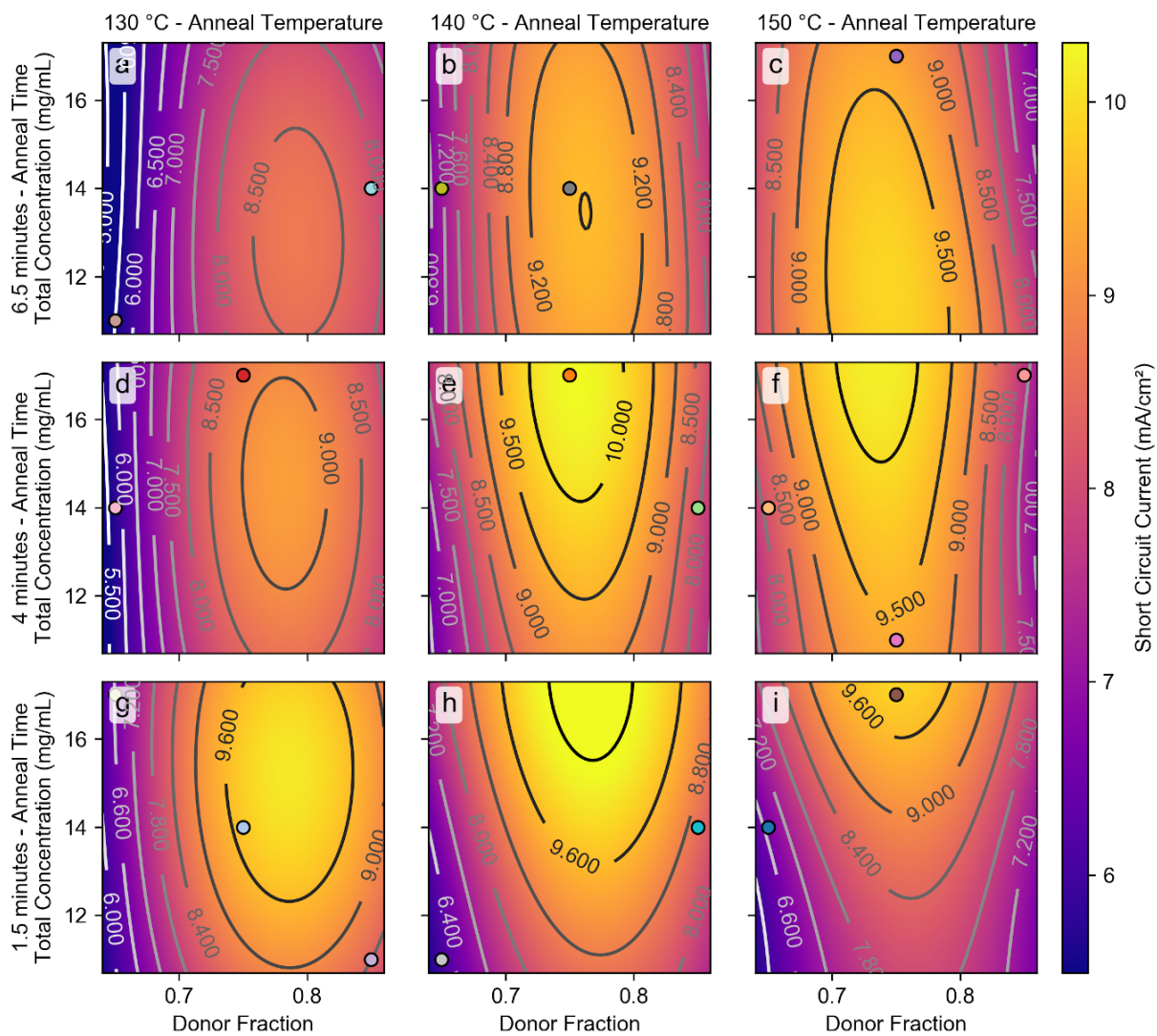


**Figure A.13:** ML-generated  $J_{sc}$  map for the second round of DRCN5T/ITIC BHJ blend optimization.

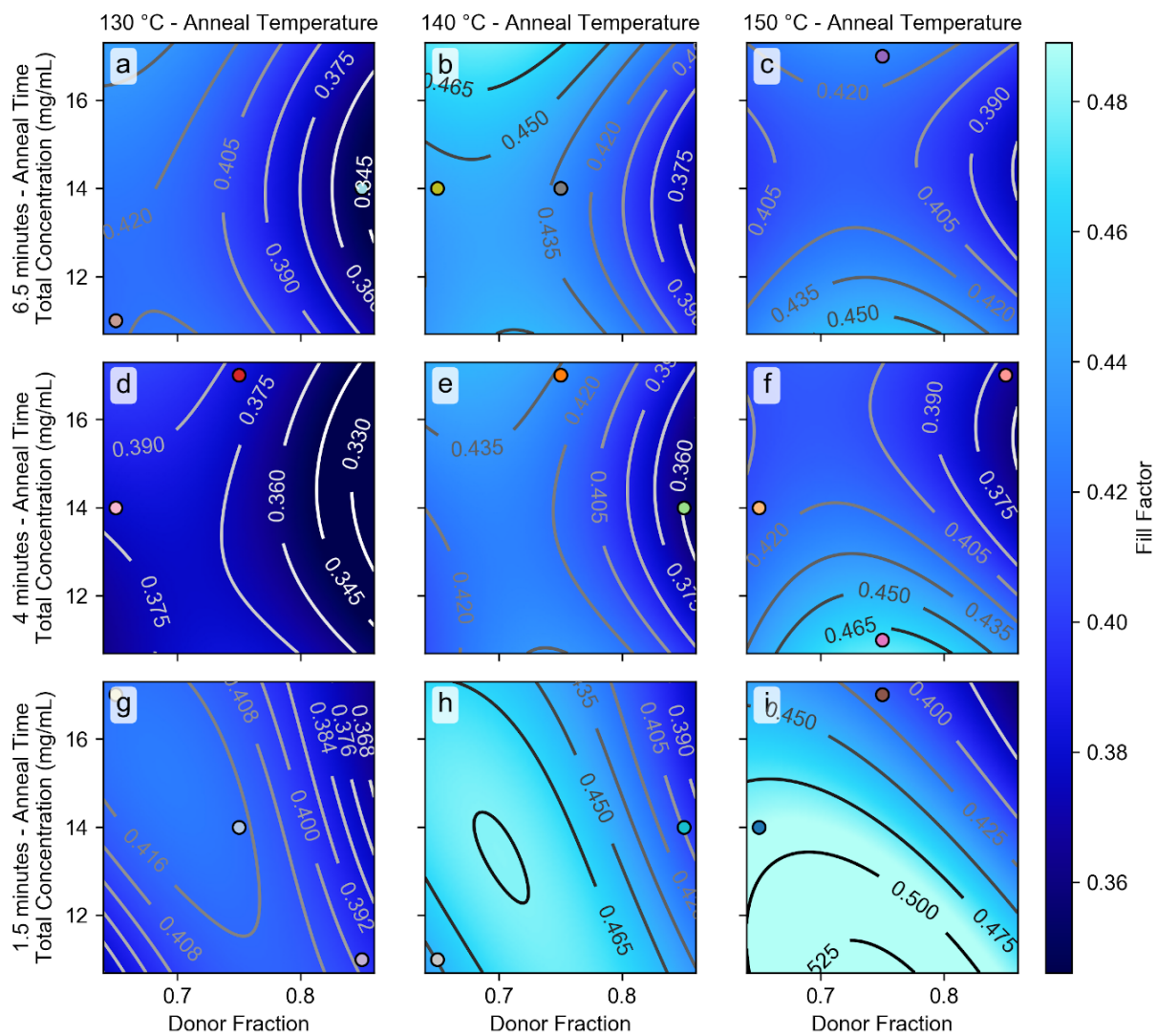


**Figure A.14:** ML-generated map of FFs for the second round of DRCN5T/ITIC BHJ blend optimization.

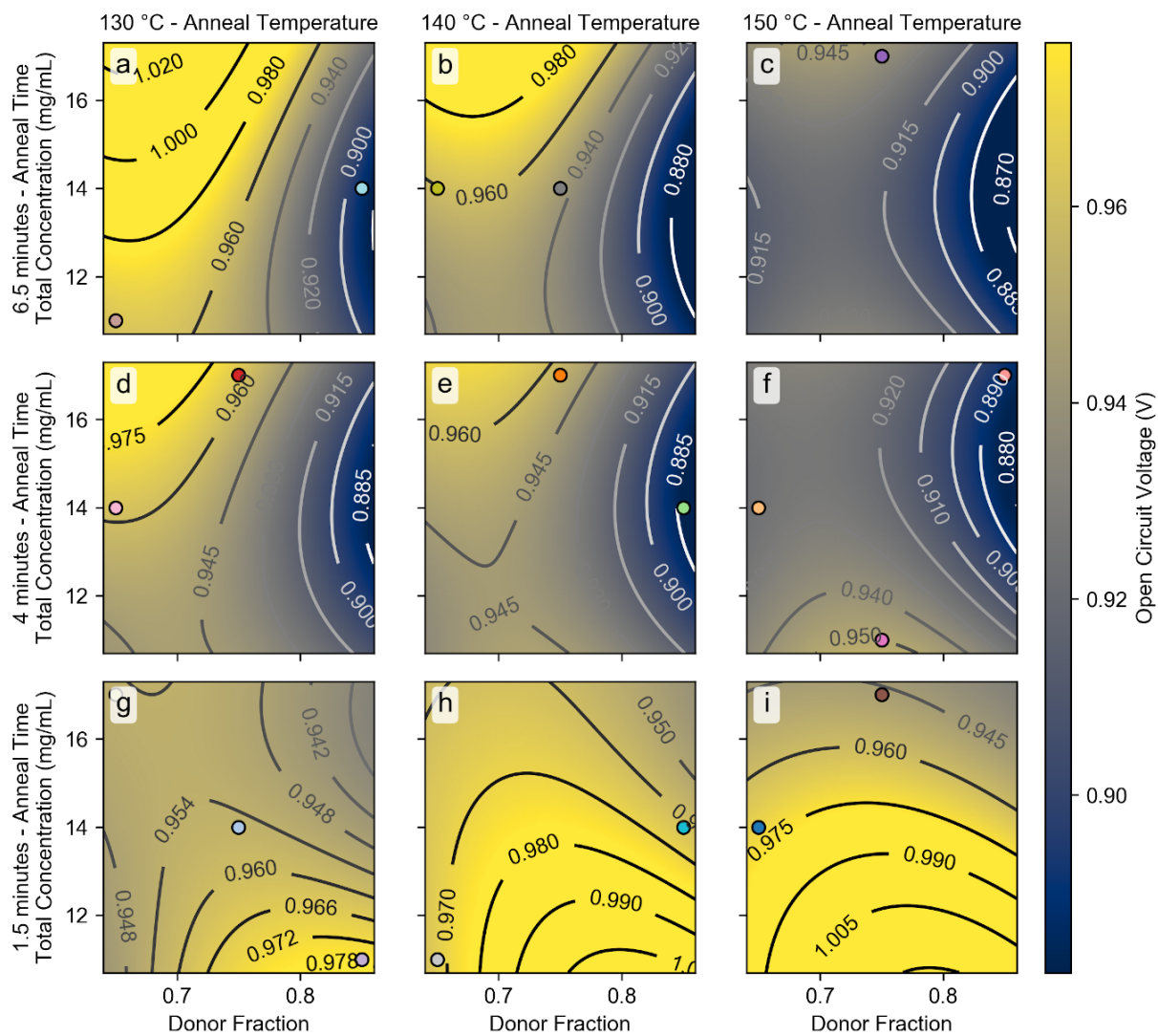


**Figure A.15:** ML-generated  $V_{oc}$  map for the second round of DRCN5T/ITIC BHJ blend optimization.

IT-M Round 1				IT-M Round 2				IT-M Round 3			
BHJ Conc. (mg/mL)	10	14	18	BHJ Conc. (mg/ml)	14	18	22	BHJ conc.		Donor Fraction	
#of expts	3	3	3	#of expts	3	3	3	mg/mL		°C	
Donor Fraction	0.5	0.65	0.8	Donor Fraction	0.6	0.7	0.8	0	20	0.65	160
#of expts	3	3	3	#of expts	3	3	3	1	20	0.75	160
Annealing Temp. (°C)	120	140	160	Annealing Temp. (°C)	160	180	200	2	24	0.65	160
#of expts	3	3	3	#of expts	3	3	3	3	24	0.75	160
								4	26	0.7	160
								5	18	0.8	160

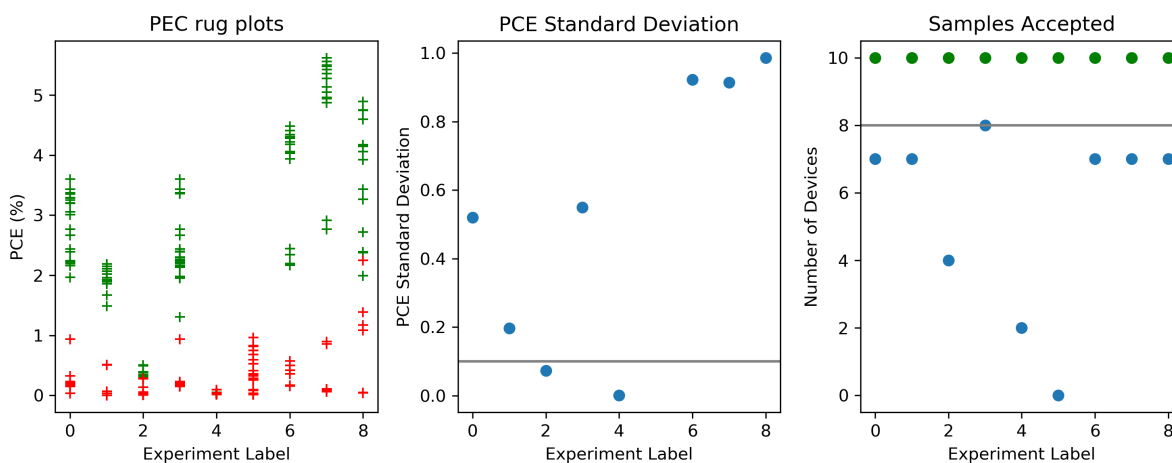
  

Expt #	BHJ conc. mg/mL	Donor Fraction	Annealing Temp. °C
0	14	0.65	140
1	18	0.8	120
2	10	0.65	120
3	18	0.5	140
4	14	0.5	120
5	10	0.5	160
6	10	0.8	140
7	18	0.65	160
8	14	0.8	160

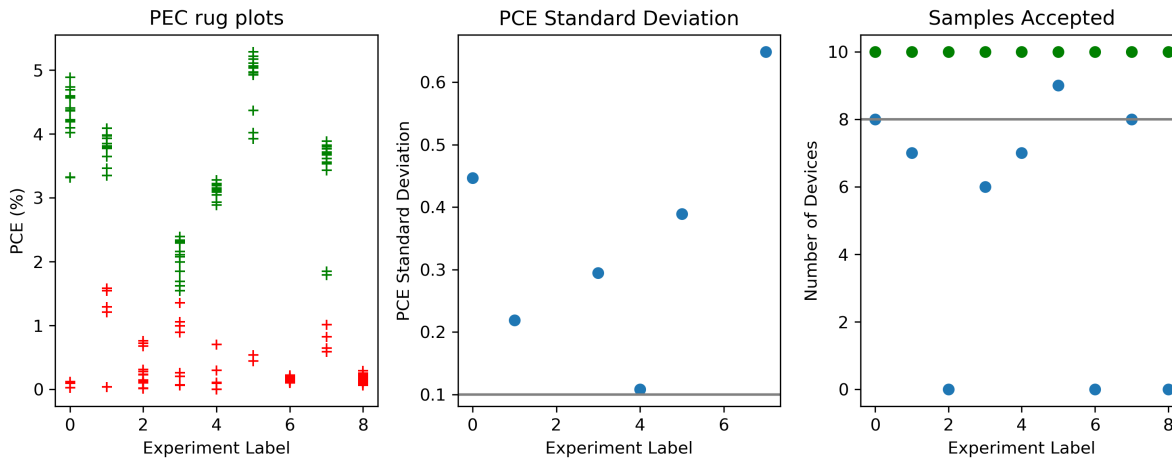
  

Expt #	total_con mg/mL	don_con	Ann_temp °C
0	18	0.6	160
1	14	0.8	160
2	22	0.6	200
3	14	0.6	180
4	22	0.8	180
5	22	0.7	160
6	18	0.8	200
7	18	0.7	180
8	14	0.7	200

**Figure A.16:** Tabulation of the processing parameter levels, number of experiments at each level, and list of experiments for the first and second round of DRCN5T/IT-M BHJ blend optimization. All experiments in the second round of optimization were replaced by the same experiments except with an annealing temperature of 160 °C and combined with the experiments outlined in round three.



**Figure A.17:** Plots displaying the performance of devices that were accepted (green) and rejected (red), the standard deviation of devices and the number of devices accepted for each experimental condition for the first round of DRCN5T/IT-M BHJ blend optimization.



**Figure A.18:** Plots displaying the performance of devices that were accepted (green) and rejected (red), the standard deviation of devices and the number of devices accepted for each experimental condition for the second round of DRCN5T/IT-M BHJ blend optimization. Experiments 2, 6 and 8 were all annealed at 200 °C and were rejected by the data filter. This round of optimization was repeated with a fixed annealing temperature of 160 °C, with some supplemental experiments.

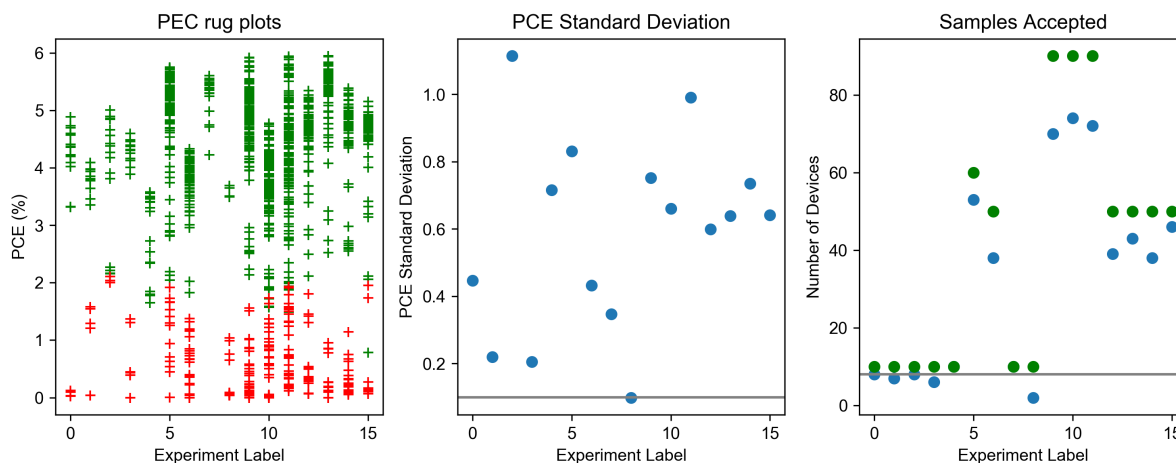


**Figure A.19:** Plots displaying the performance of devices that were accepted (green) and rejected (red), the standard deviation of devices and the number of devices accepted for each experimental condition for the second round of DRCN5T/IT-M BHJ blend optimization.

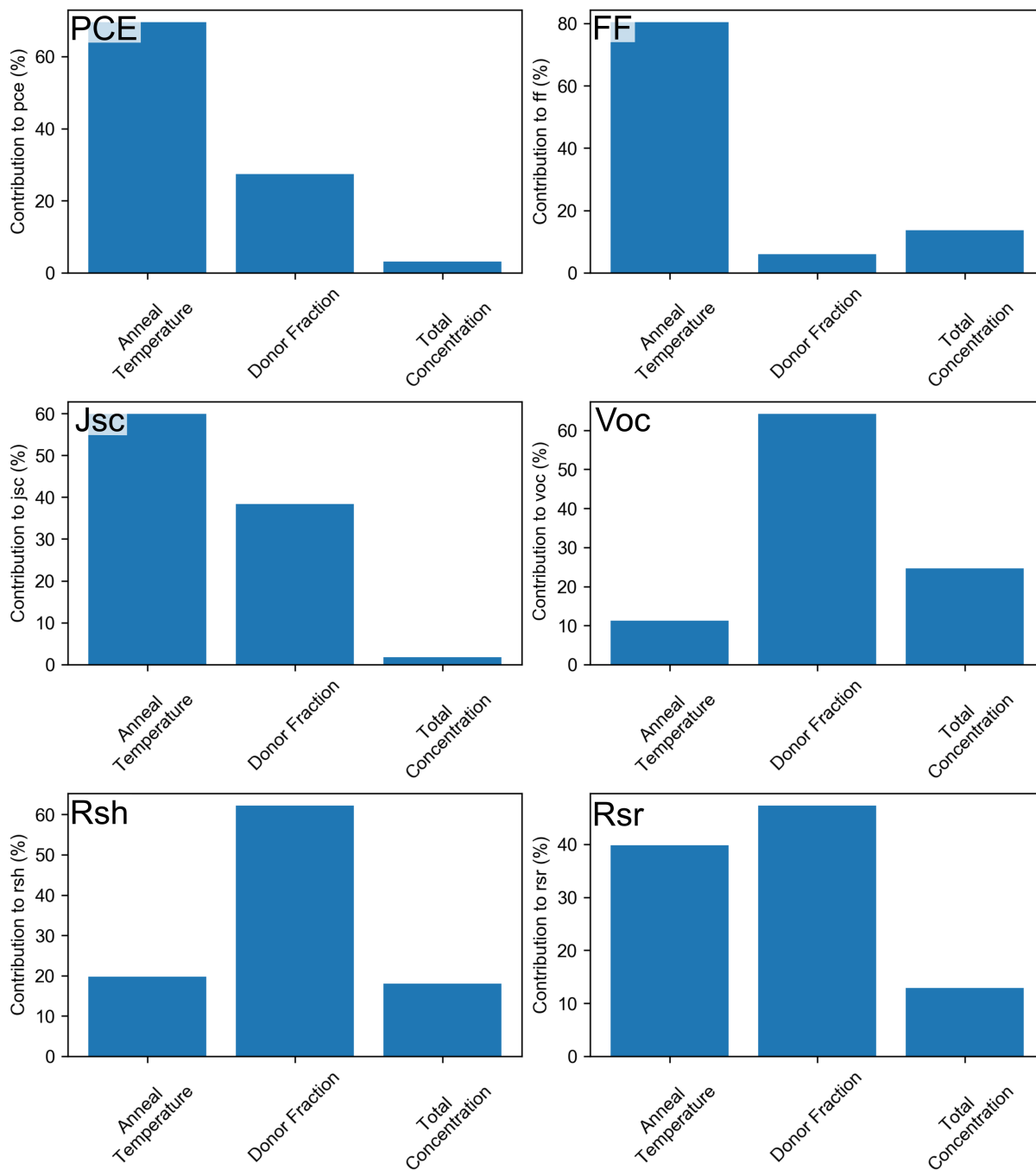


**Figure A.20:** ANOVAs of the relative contribution of the processing parameters on PCE, FF,  $J_{sc}$ ,  $V_{oc}$ ,  $R_{sh}$  and  $R_{sr}$  for the first round of DRCN5T/IT-M BHJ blend optimization.

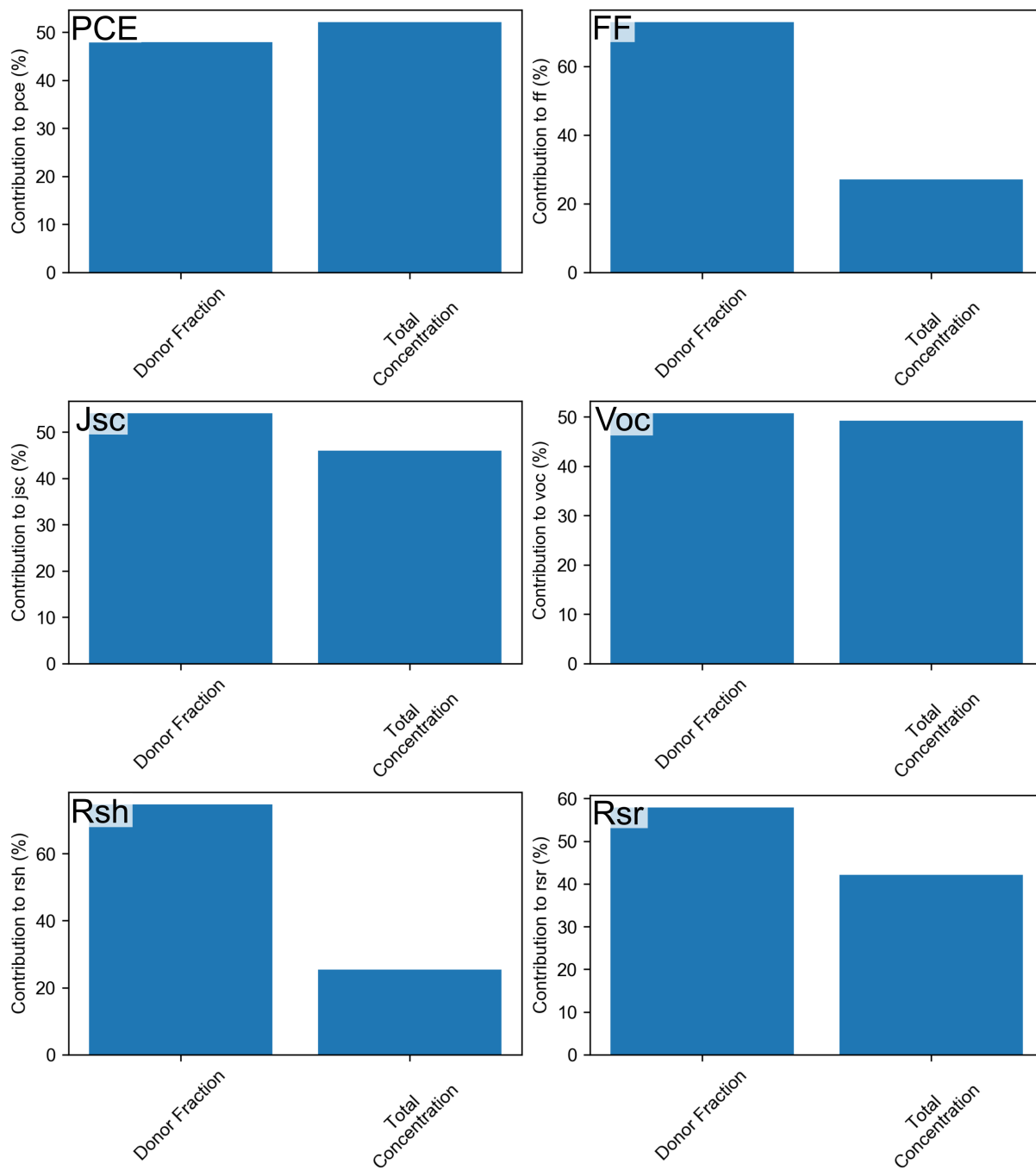


**Figure A.21:** ANOVAs of the relative contribution of the processing parameters on PCE, FF,  $J_{sc}$ ,  $V_{oc}$ ,  $R_{sh}$  and  $R_{sr}$  for the second round of DRCN5T/IT-M BHJ blend optimization.

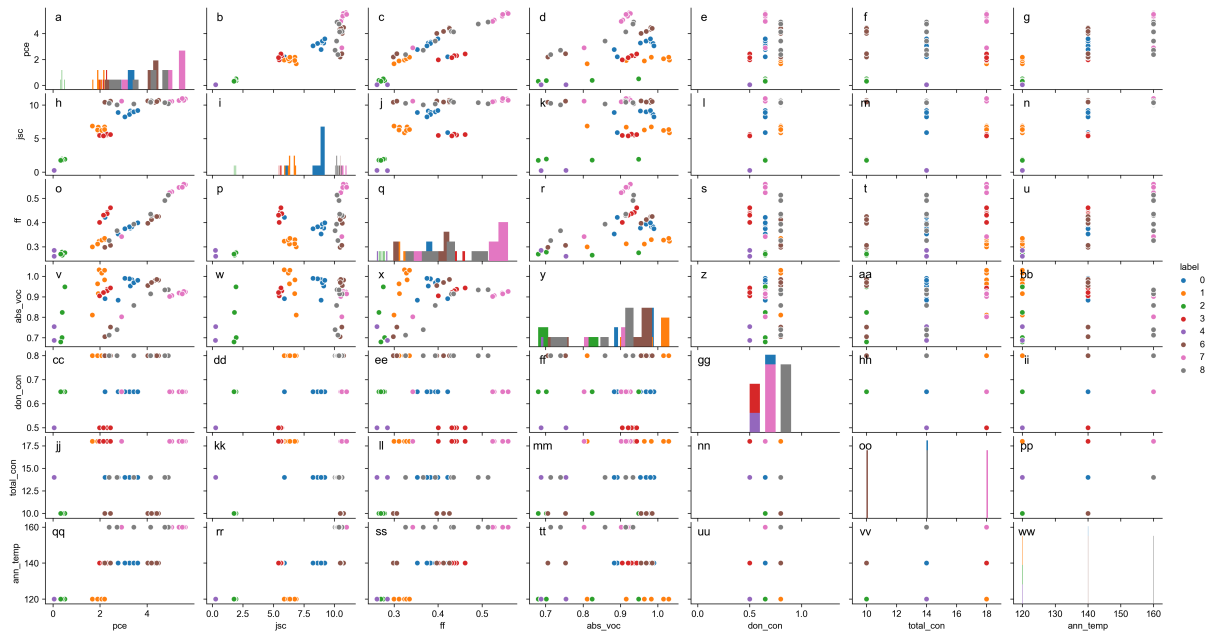


**Figure A.22:** Pair plots comparing processing parameters to PCE,  $J_{sc}$ , FF or  $V_{oc}$ , for the first round of DRCN5T/IT-M BHI blend optimization.

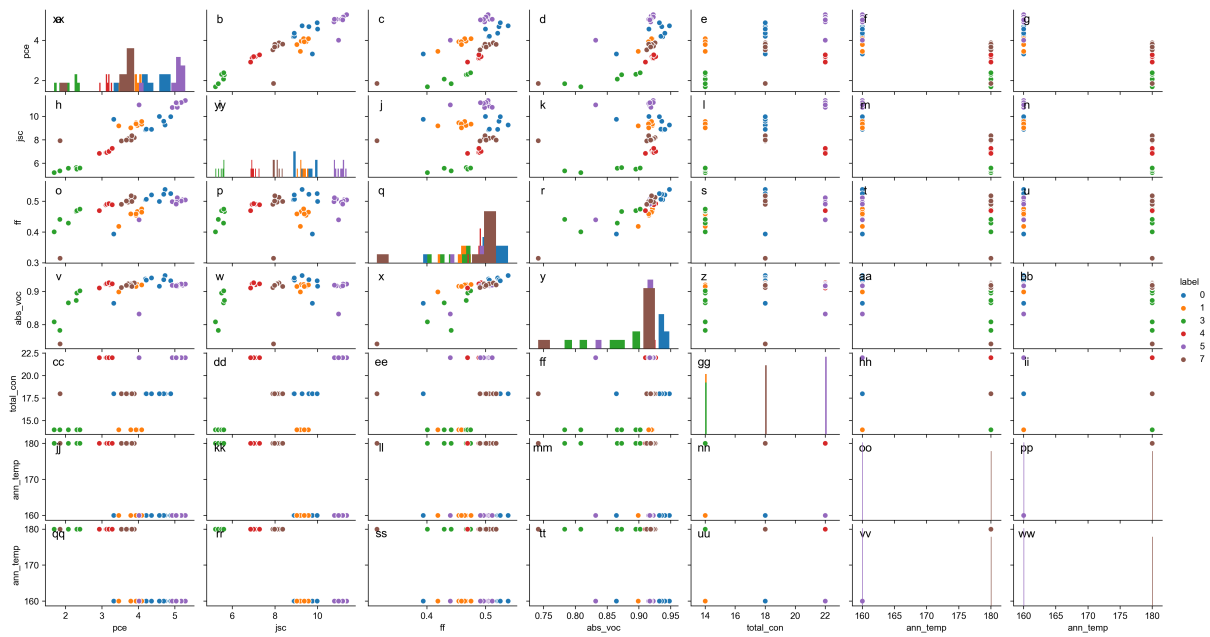


**Figure A.23:** Pair plots comparing processing parameters to PCE,  $J_{sc}$ , FF or  $V_{oc}$ , for the second round of DRCN5T/IT-M BHI blend optimization showing the low PCE of samples annealed at 180 °C, in box g) in the top right corner.

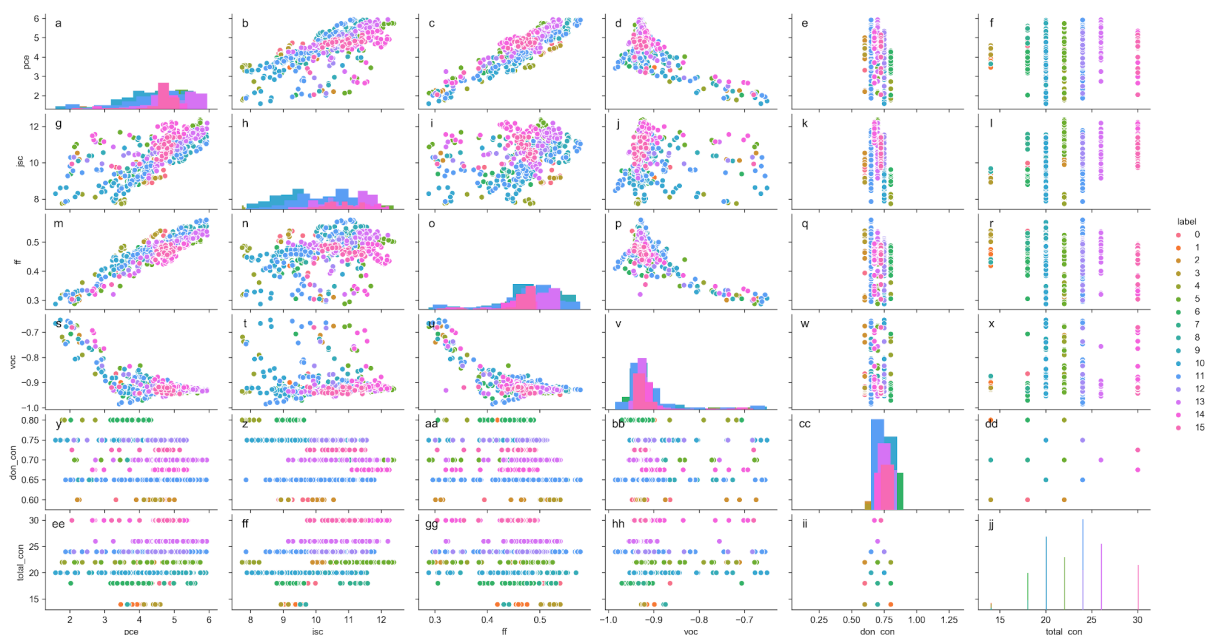


**Figure A.24:** Pair plots comparing processing parameters to PCE,  $J_{sc}$ , FF or  $V_{oc}$ , for the second (at 160 °C) and third round of DRCN5T/IT-M BHJ blend optimization.

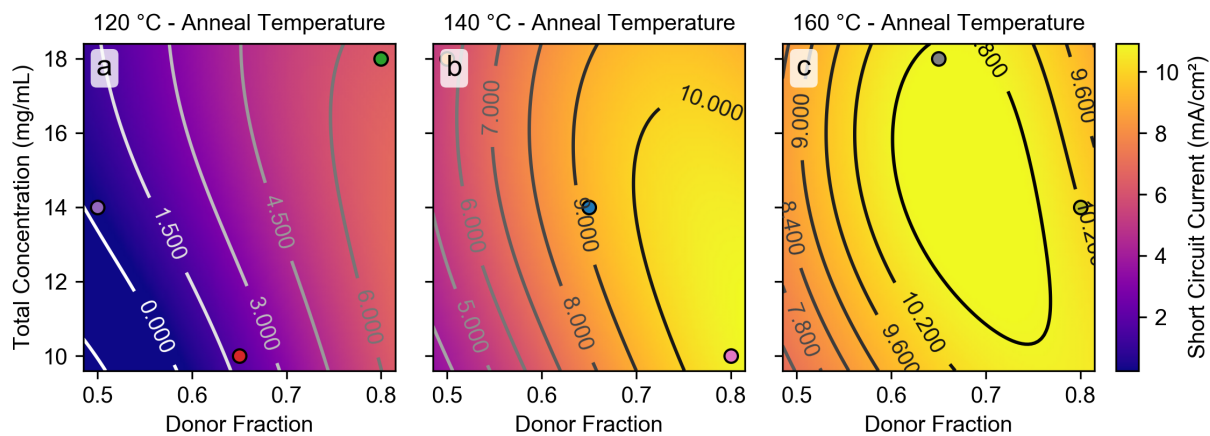


**Figure A.25:** ML-generated  $J_{sc}$  map for the first round of DRCN5T/IT-M BHJ blend optimization.

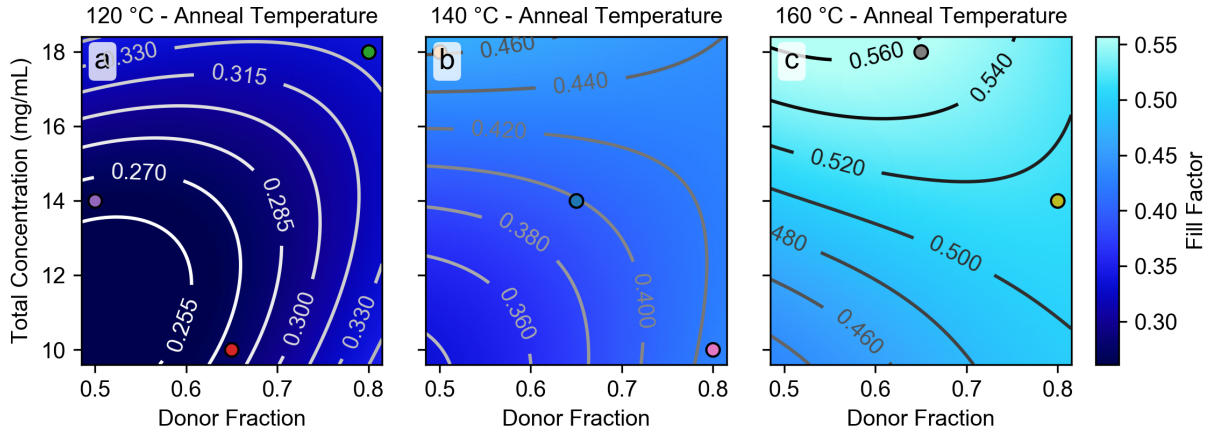


**Figure A.26:** ML-generated FF map for the first round of DRCN5T/IT-M BHJ blend optimization.

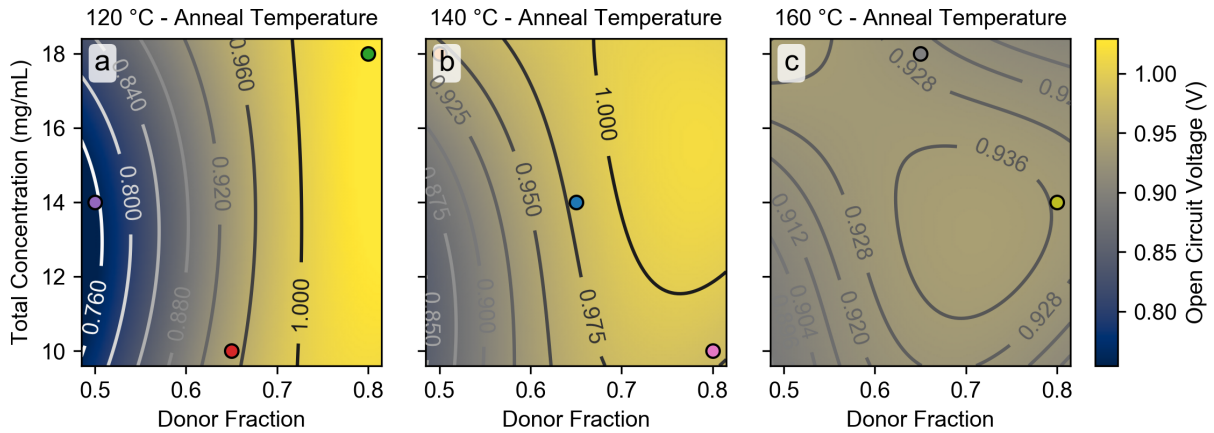


**Figure A.27:** ML-generated  $V_{oc}$  map for the first round of DRCN5T/IT-M BHJ blend optimization.

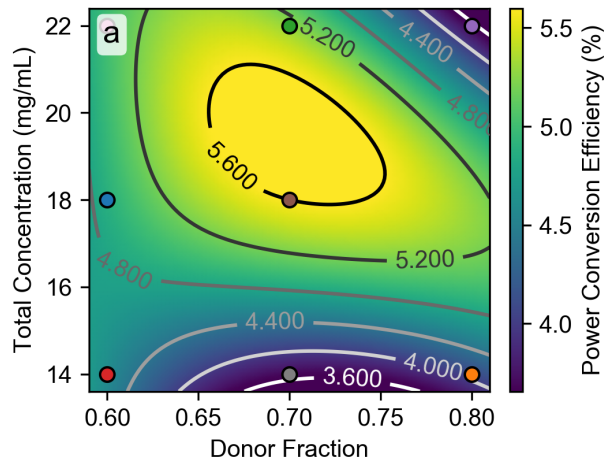


**Figure A.28:** ML-generated PCE map for the second round of DRCN5T/IT-M BHJ blend optimization. This map served as the skeleton for higher resolution sampling of the parameter space.

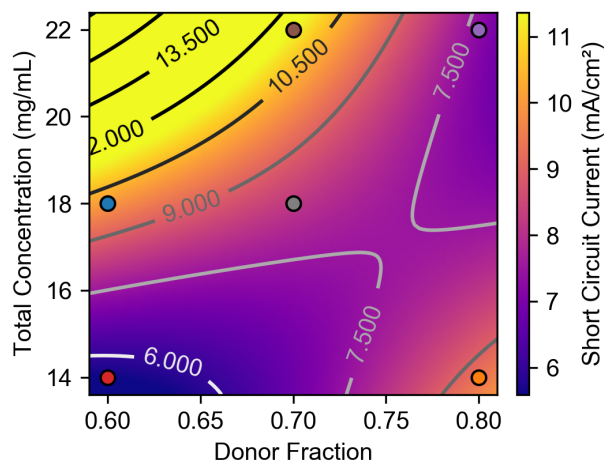


**Figure A.29:** ML-generated  $J_{sc}$  map for the second round of DRCN5T/IT-M BHJ blend optimization.

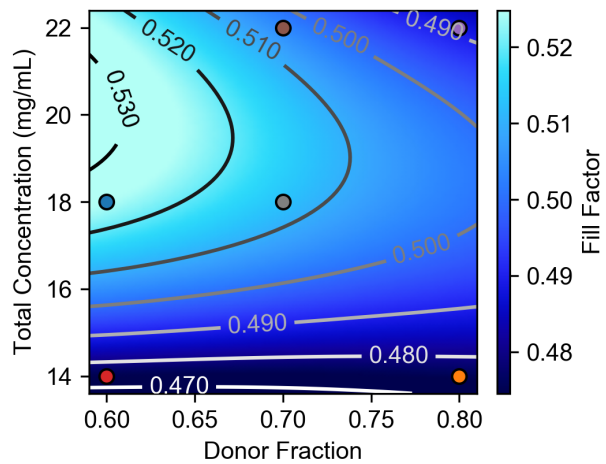


**Figure A.30:** ML-generated FF map for the second round of DRCN5T/IT-M BHJ blend optimization.

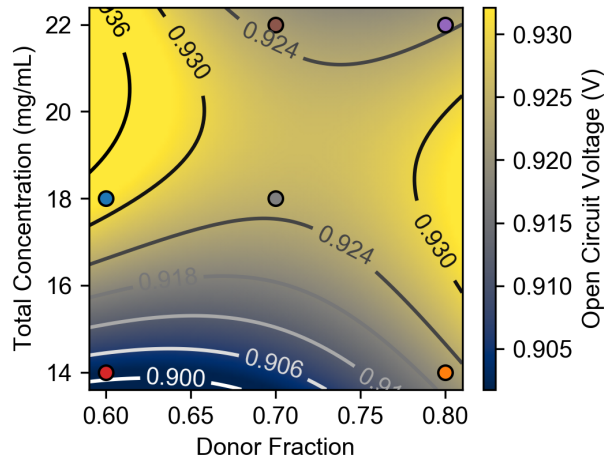


**Figure A.31:** ML-generated  $V_{oc}$  map for the second round of DRCN5T/IT-M BHI blend optimization.

IT-4F Round 1					IT-4F Round 2				
BHJ Conc. (mg/ml)	16	22	28		BHJ Conc. (mg/mL)	13	16	19	
# of exp'ts	5	4	4		# of exp'ts	2	2	2	
Donor Fraction	0.6	0.7	0.8		Annealing Temp. (°C)	130	150		
# of exp'ts	4	5	4		# of exp'ts	3	3		
Annealing Temp. (°C)	150	170			Annealing Time (Minutes)	12	20	28	
# of exp'ts	7	6			# of exp'ts	2	2	2	
Annealing Time (Minutes)	4	8	12						
# of exp'ts	5	4	4						
					Exp't #	BHJ conc. (mg/mL)	Donor Fraction	Ann. Temp (degC)	Ann. Time (minutes)
Exp't #	BHJ conc. mg/mL	Donor Fraction	Temperature °C	Time	0	19	0.7	150	20
0	16	0.6	150	8	1	16	0.7	130	12
1	16	0.8	150	4	2	19	0.7	130	28
2	16	0.7	170	8	3	13	0.7	150	12
3	22	0.7	150	8	4	13	0.7	130	20
4	22	0.7	170	4	5	16	0.7	150	28
5	22	0.6	150	4					
6	28	0.8	150	12					
7	28	0.7	150	4					
8	16	0.6	170	4					
9	22	0.8	170	12					
10	28	0.6	170	12					
11	16	0.7	150	12					
12	28	0.8	170	8					

**Figure A.32:** Tabulation of the processing parameter levels, number of experiments at each level for the first and list of experiments for the first and second round of DRCN5T/IT-4F BHI blend optimization.

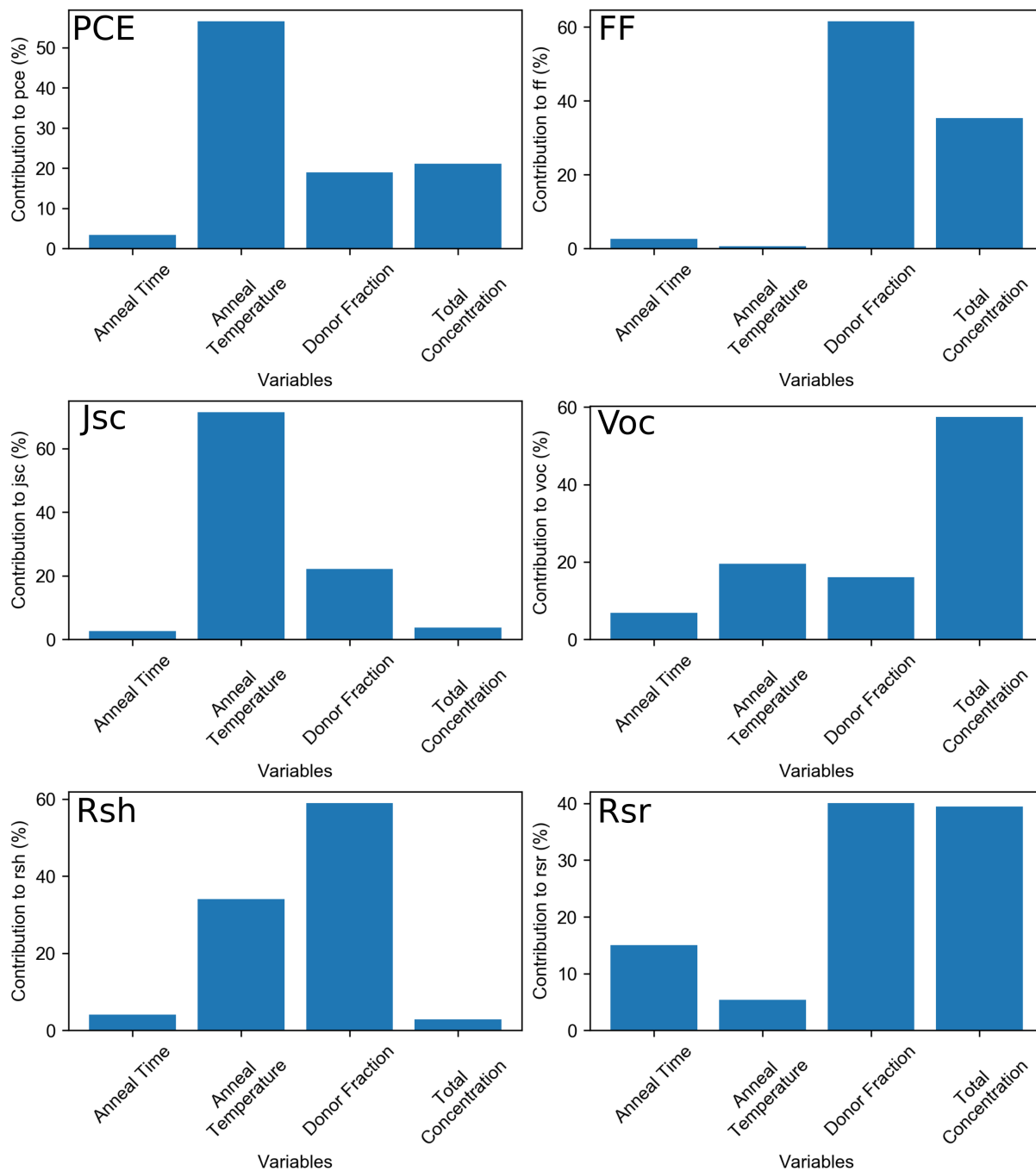


**Figure A.33:** ANOVAs of the relative contribution of the processing parameters on PCE, FF,  $J_{sc}$ ,  $V_{oc}$ ,  $R_{sh}$  and  $R_{sr}$  for the first round of DRCN5T/IT-4F BJJ blend optimization.

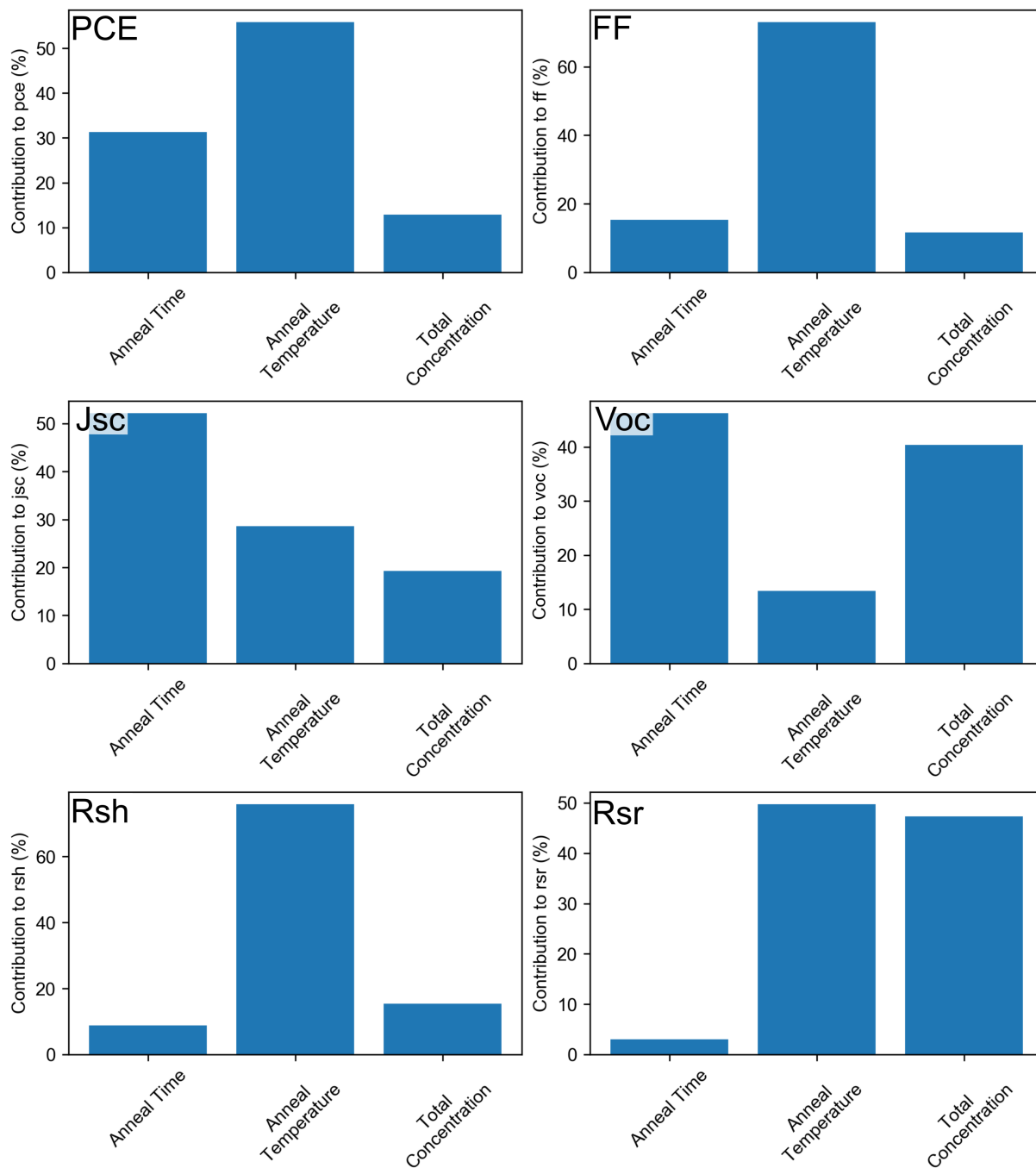


**Figure A.34:** ANOVAs of the relative contribution of the processing parameters on PCE, FF,  $J_{sc}$ ,  $V_{oc}$ ,  $R_{sh}$  and  $R_{sr}$  for the second round of DRCN5T/IT-4F BHJ blend optimization.

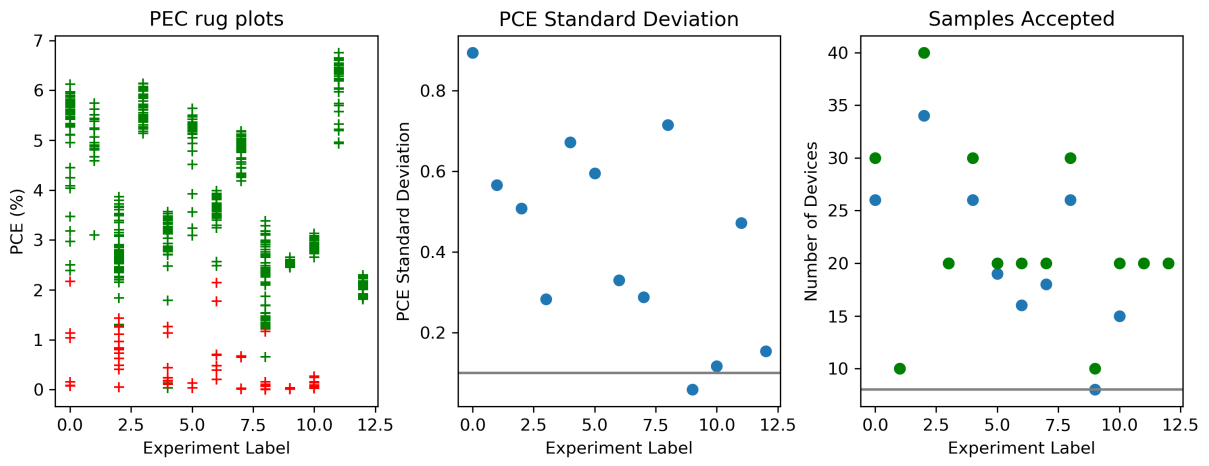


**Figure A.35:** Plots displaying the performance of devices that were accepted (green) and rejected (red), and the standard deviation of devices and the number of devices accepted for each experimental condition for the first round of DRCN5T/IT-4F BHJ blend optimization.

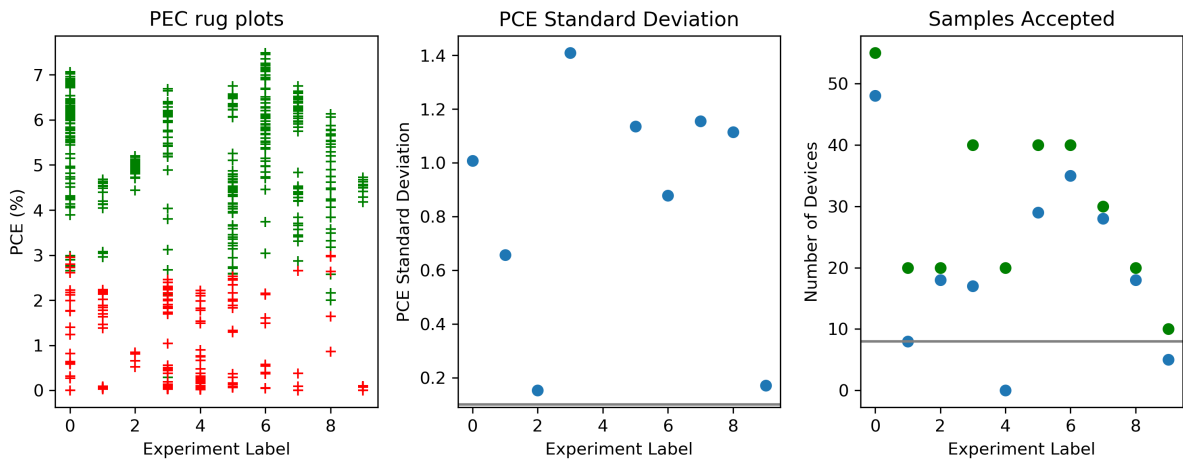


**Figure A.36:** Plots displaying the performance of devices that were accepted (green) and rejected (red), and the standard deviation of devices and the number of devices accepted for each experimental condition for the second round of DRCN5T/IT-4F BHJ blend optimization.

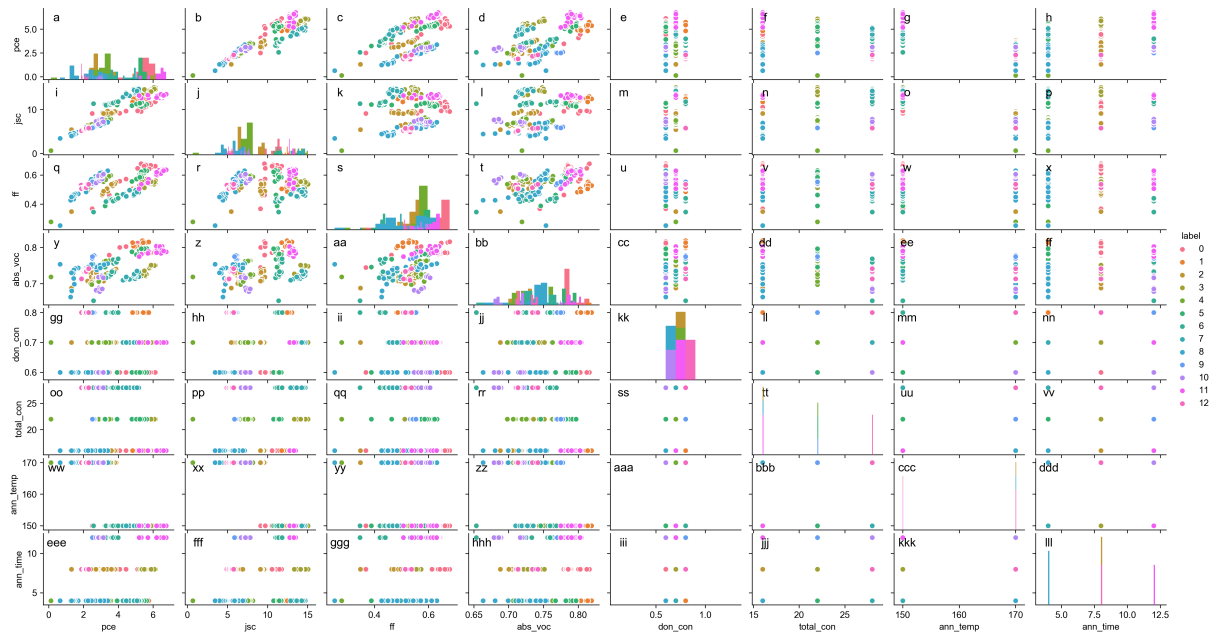


**Figure A.37:** Pair plots comparing processing parameters to PCE,  $J_{sc}$ , FF or  $V_{oc}$ , for the first round of DRCN5T/IT-4F BHJ blend optimization.

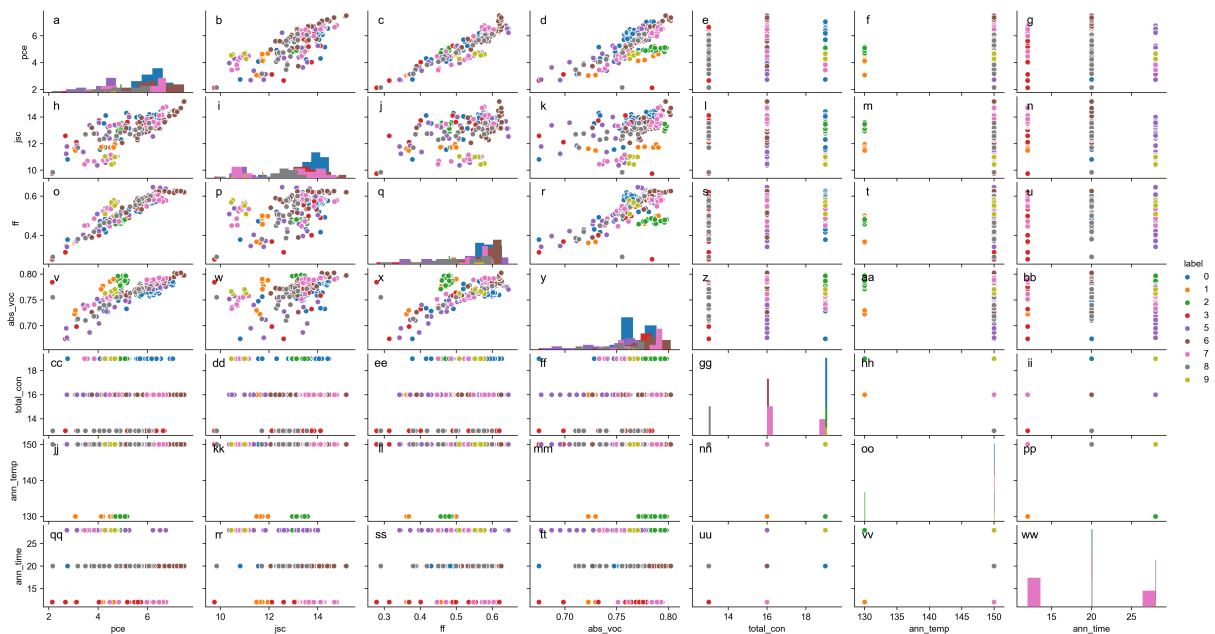


**Figure A.38:** Pair plots comparing processing parameters to PCE,  $J_{sc}$ , FF or  $V_{oc}$ , for the second round of DRCN5T/IT-4F BHJ blend optimization.

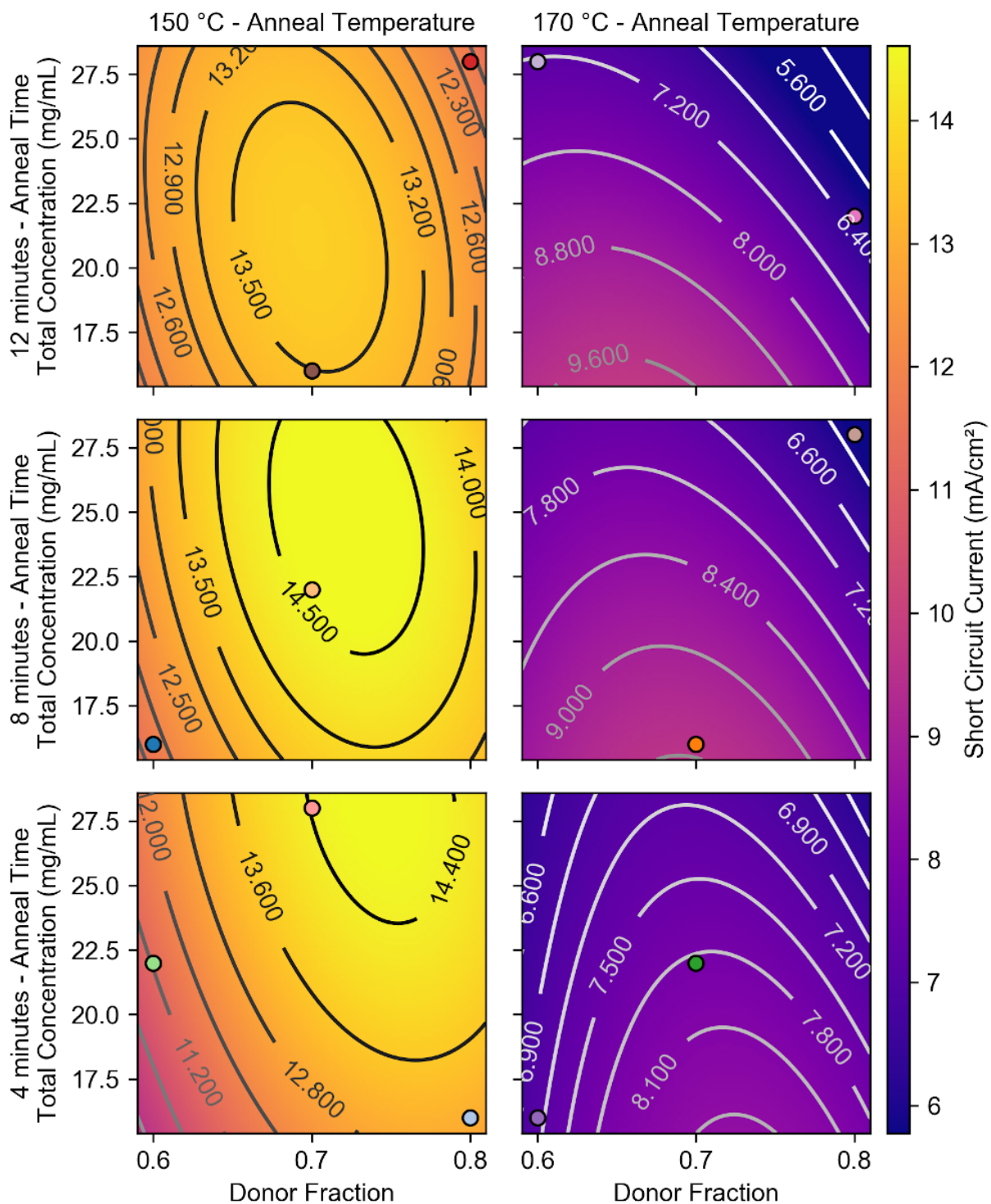


**Figure A.39:** ML-generated  $J_{sc}$  map for the first round of DRCN5T/IT-4F BHJ blend optimization.

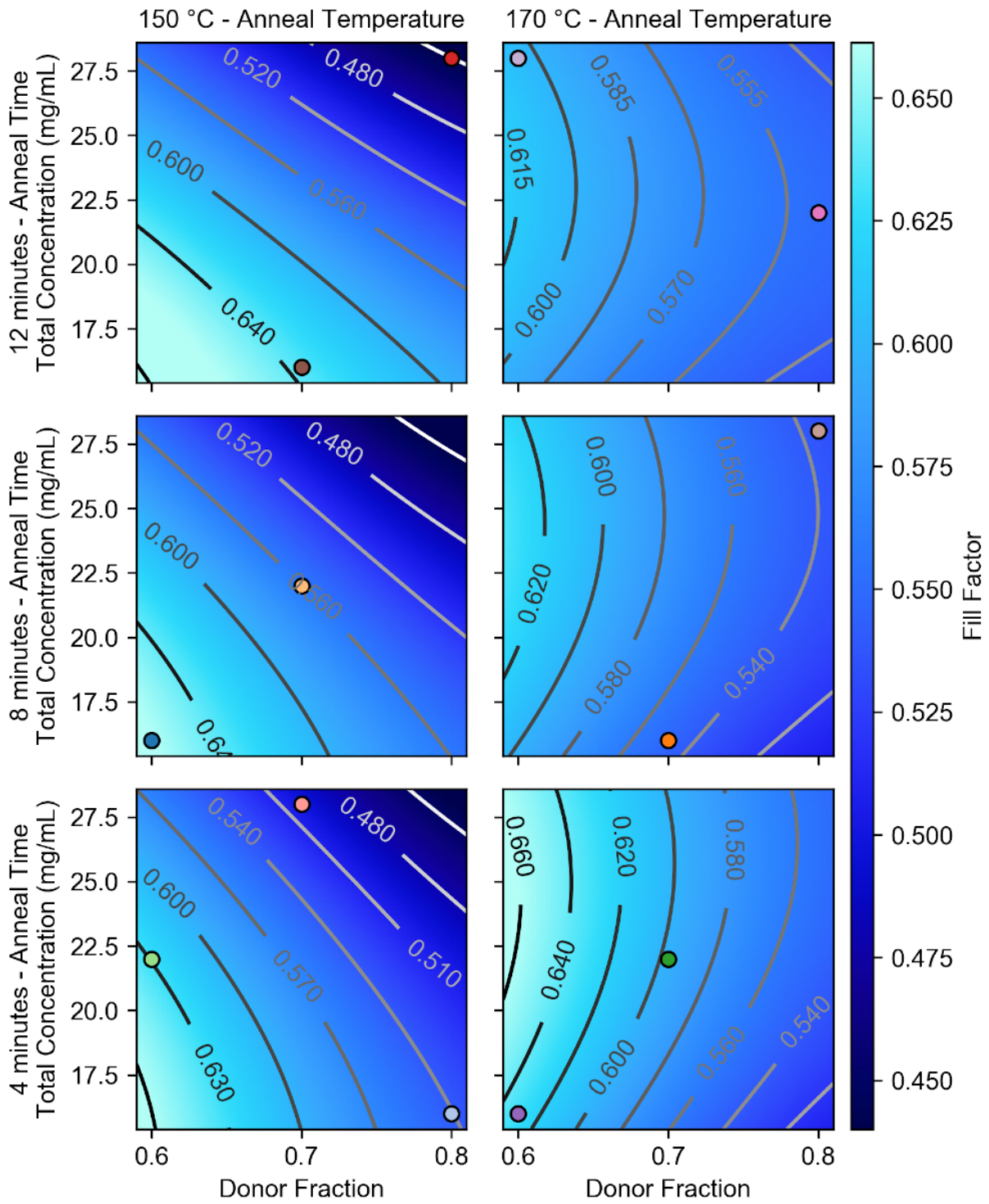


**Figure A.40:** ML-generated FF map for the first round of DRCN5T/IT-4F BHJ blend optimization.

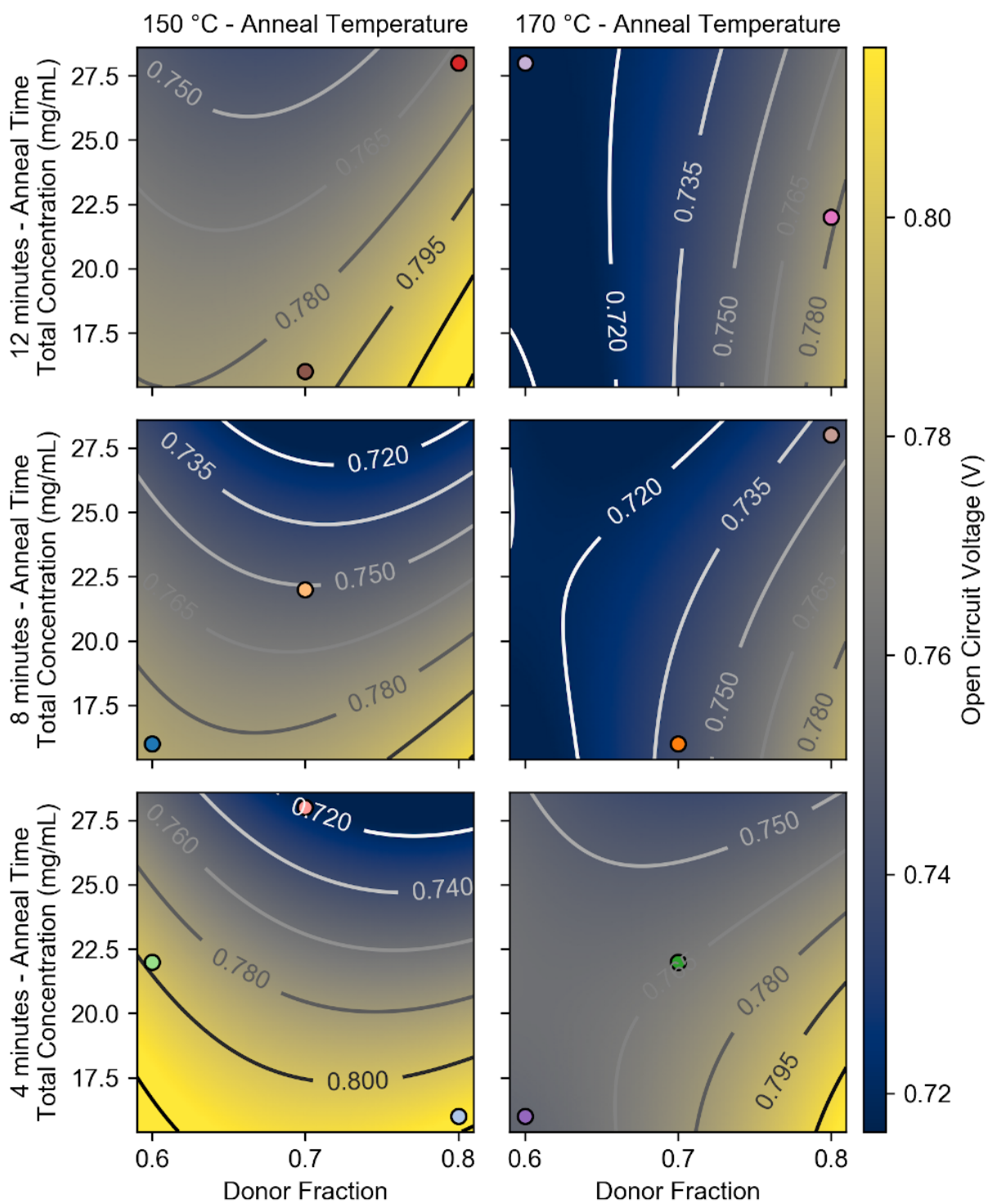


**Figure A.41:** ML-generated  $V_{oc}$  map for the first round of DRCN5T/IT-4F BHI blend optimization.

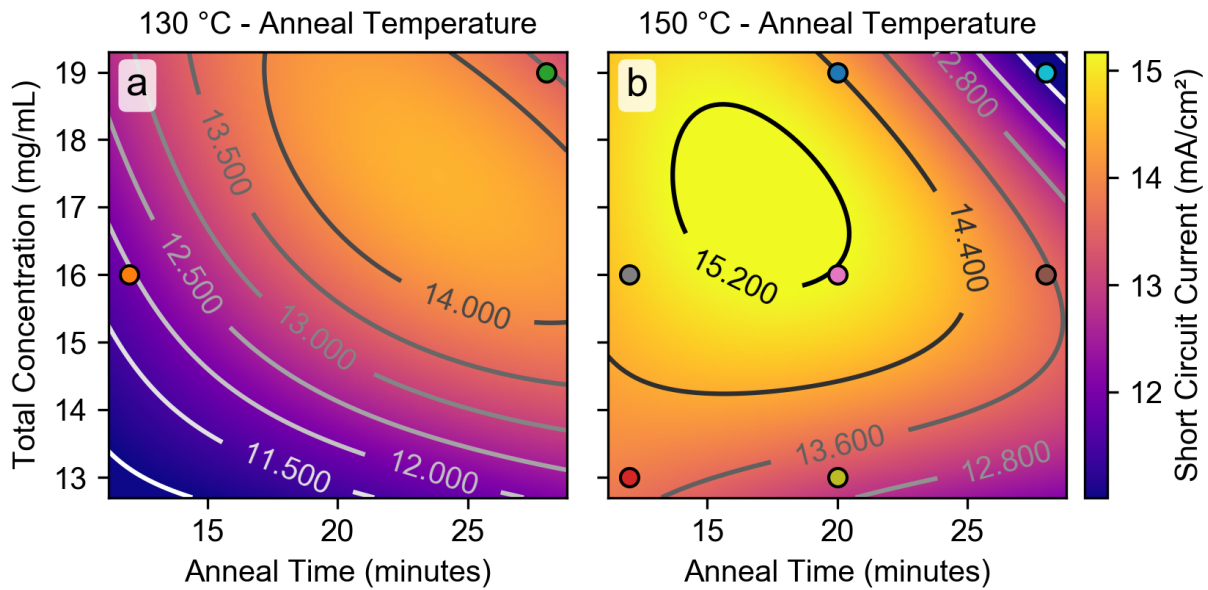


**Figure A.42:** ML-generated  $J_{sc}$  map for the second round of DRCN5T/IT-4F BHJ blend optimization.

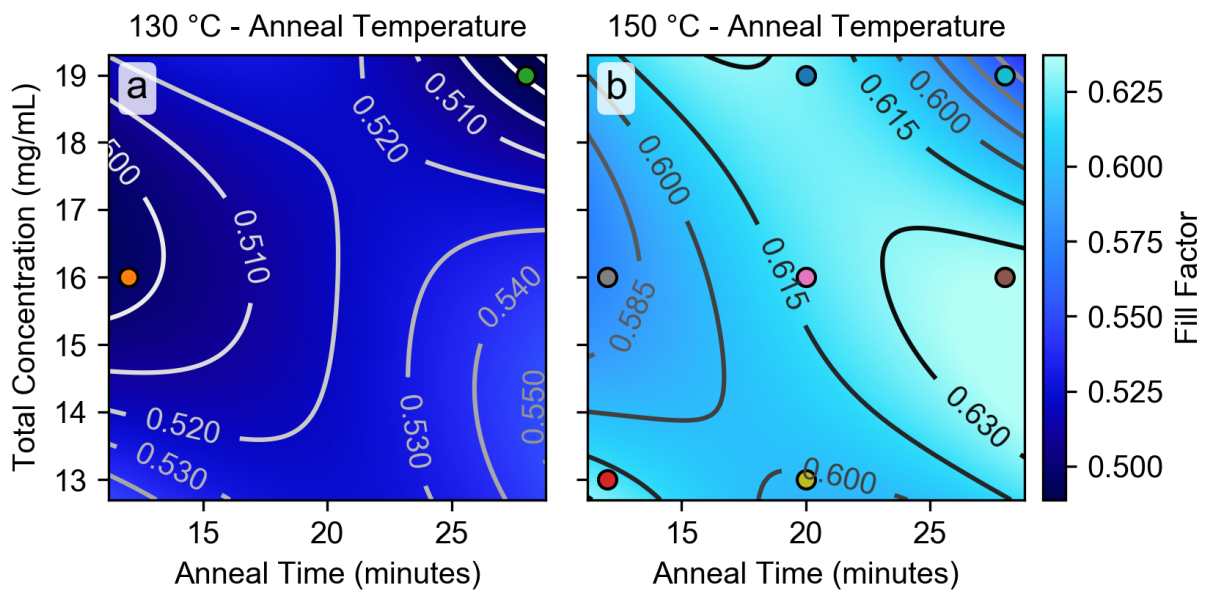


**Figure A.43:** ML-generated FF map for the second round of DRCN5T/IT-4F BHJ blend optimization.

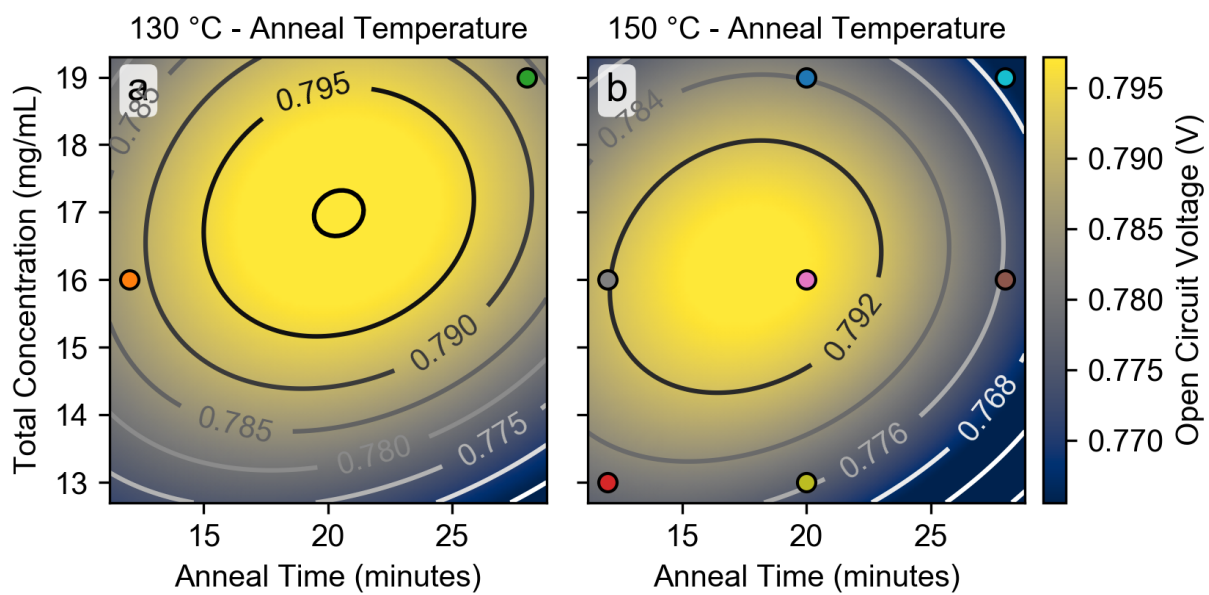


**Figure A.44:** ML-generated  $V_{oc}$  map for the second round of DRCN5T/IT-4F BHJ blend optimization.

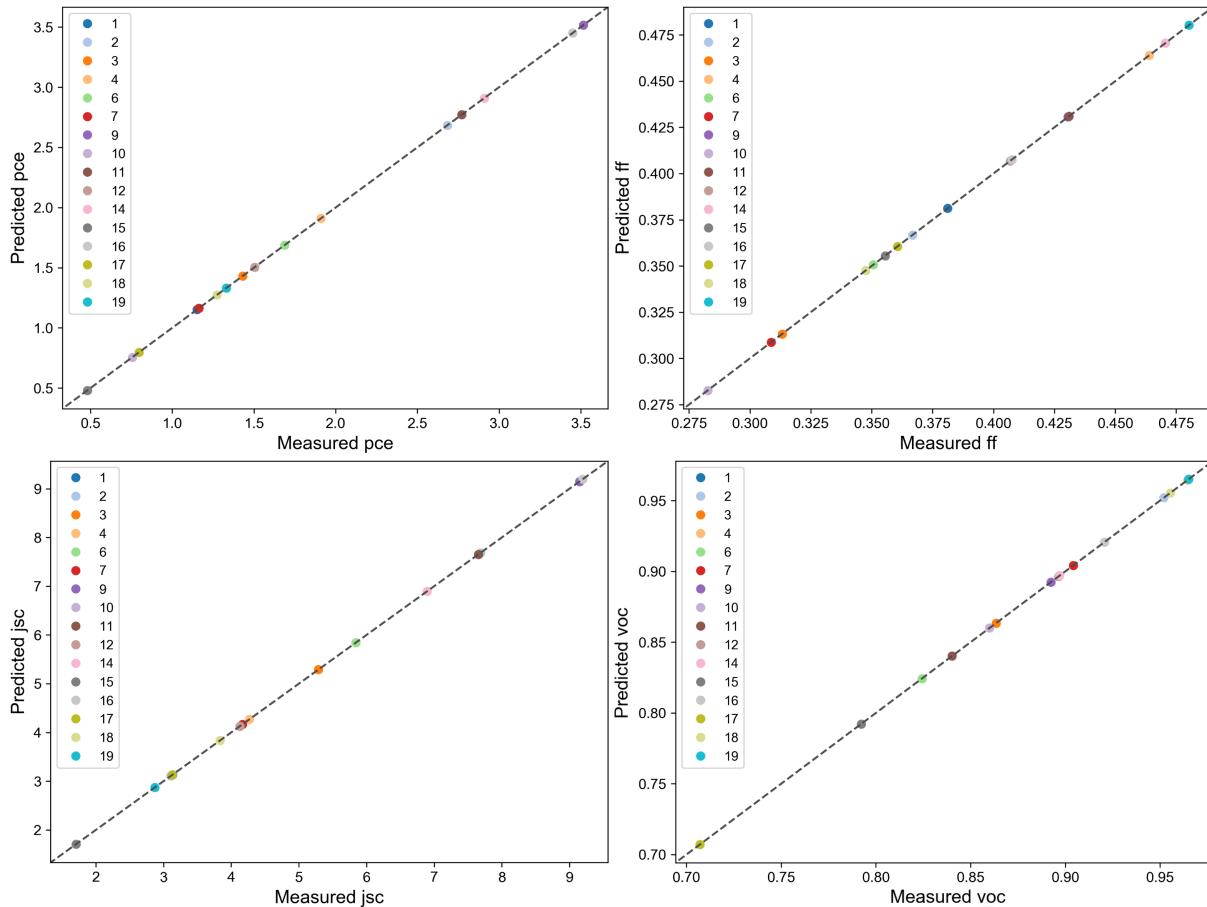


**Figure A.45:** ML-derived predictions of fit for the first round of DRCN5T/ITIC BHJ blend optimization. Gamma (or compliance) values were reduced until a device deviated from the linear trendline. This gamma value represents the least accommodating fit that is capable of producing a topology that tracks to the experimental data.

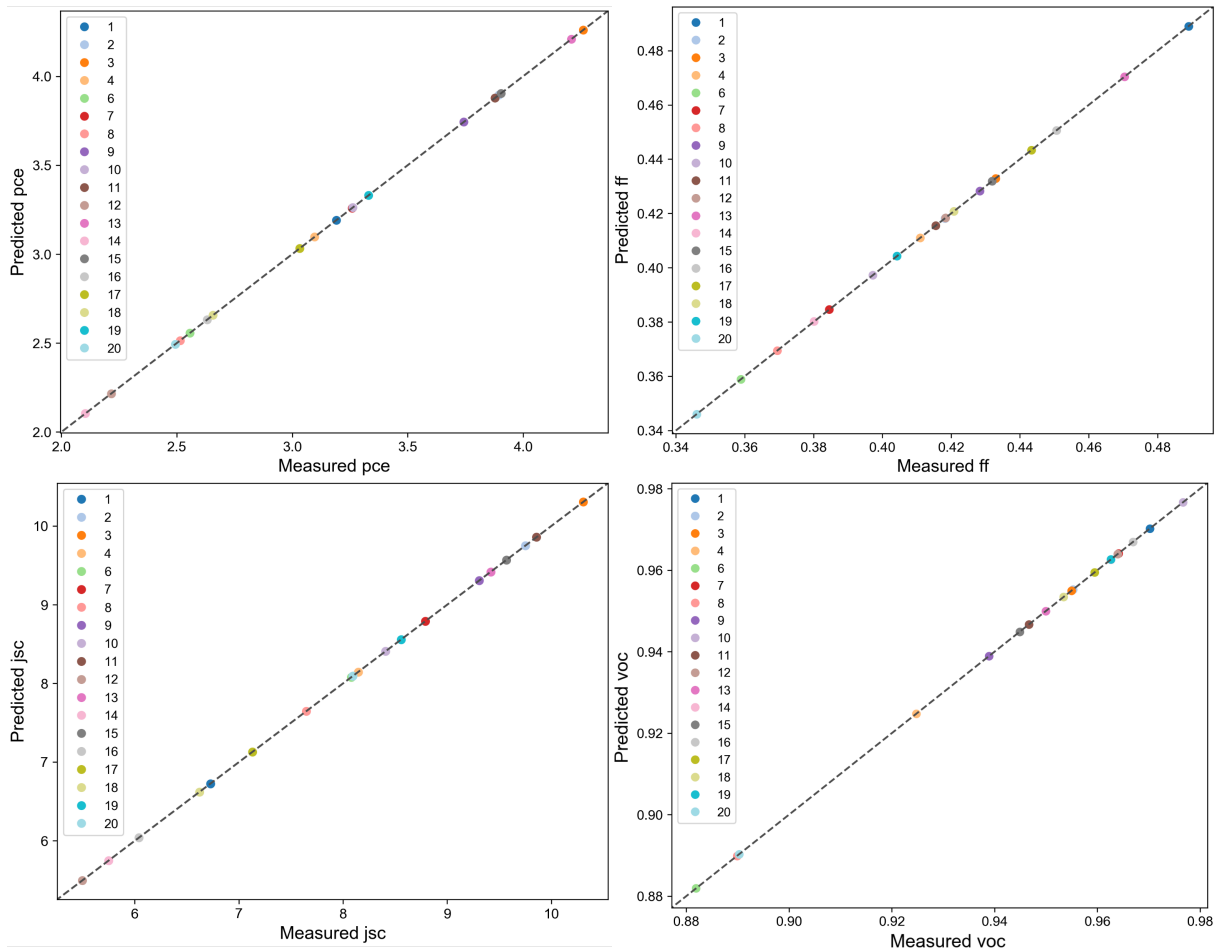


**Figure A.46:** ML-derived predictions of fit for the second round of DRCN5T/ITIC BHJ blend optimization. Gamma (or compliance) values are reduced until a device deviates from the linear trendline. This gamma value represents the least accommodating fit that is capable of producing a topology that tracks to the experimental data.

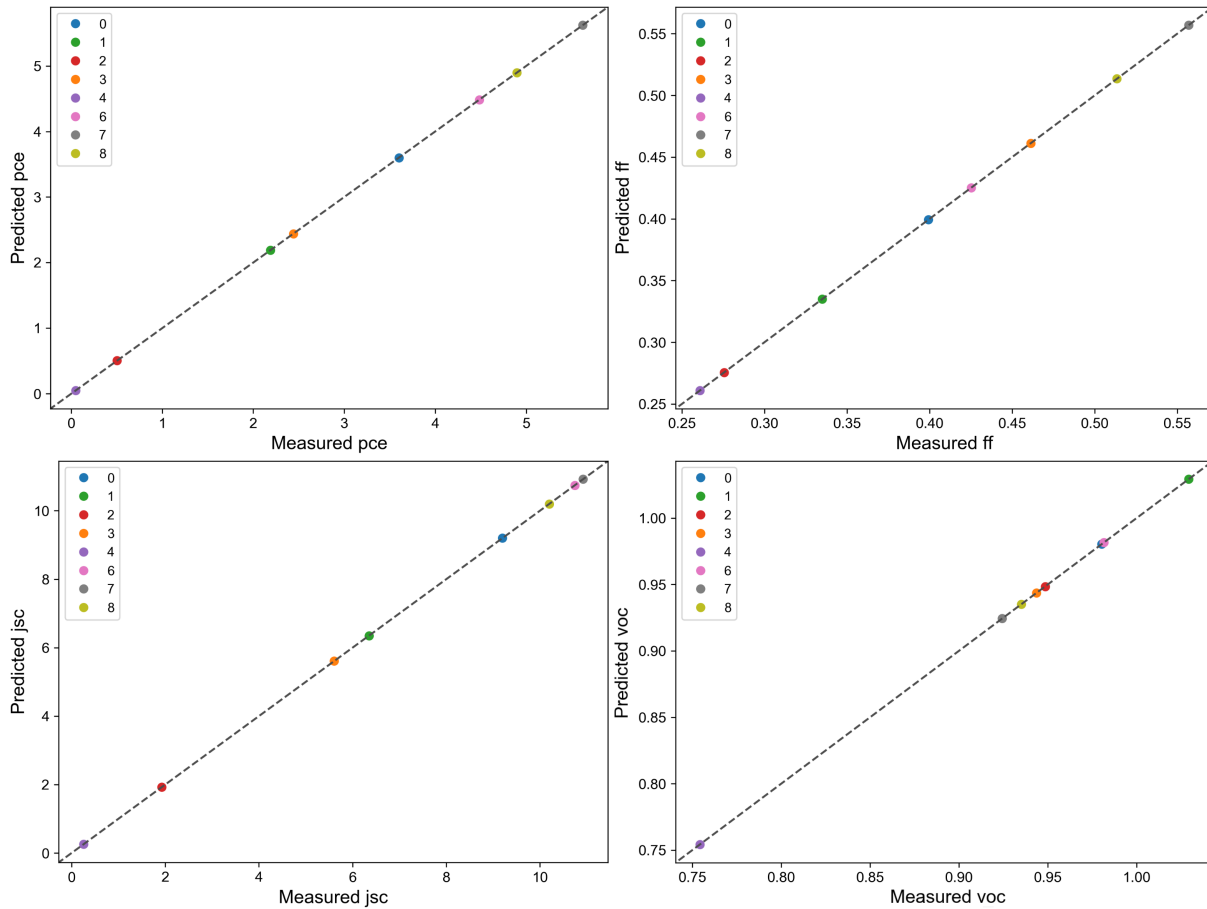


**Figure A.47:** ML-derived predictions of fit for the first round of DRCN5T/IT-M BHJ blend optimization. Gamma (or compliance) values are reduced until a device deviates from the linear trendline. This gamma value represents the least accommodating fit that is capable of producing a topology that tracks to the experimental data.

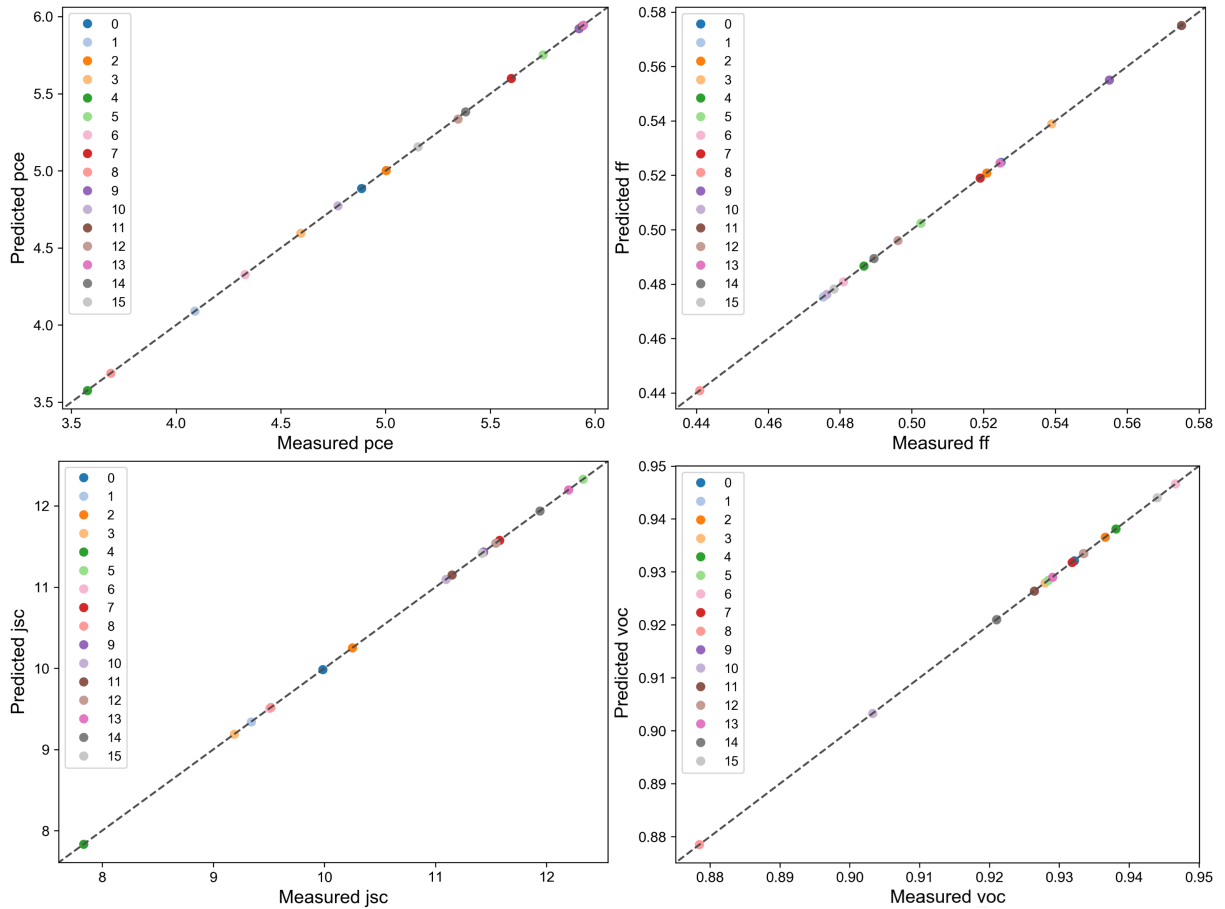


**Figure A.48:** ML-derived predictions of fit for the second round of DRCN5T/IT-M BHI blend optimization. Gamma (or compliance) values are reduced until a device deviates from the linear trendline. This gamma value represents the least accommodating fit that is capable of producing a topology that tracks to the experimental data.

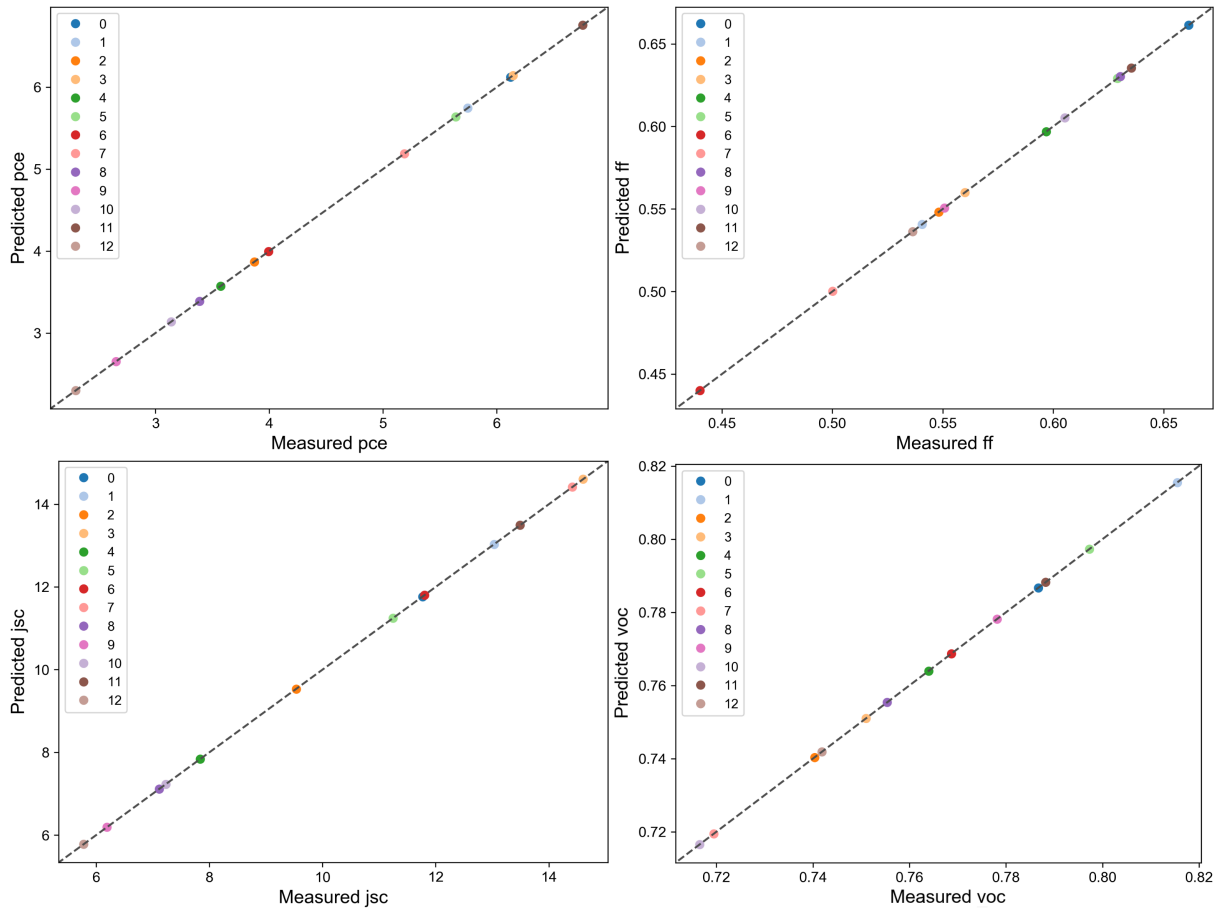


**Figure A.49:** ML-derived predictions of fit for the first round of DRCN5T/IT-4F BHI blend optimization. Gamma (or compliance) values are reduced until a device deviates from the linear trendline. This gamma value represents the least accommodating fit that is capable of producing a topology that tracks to the experimental data.

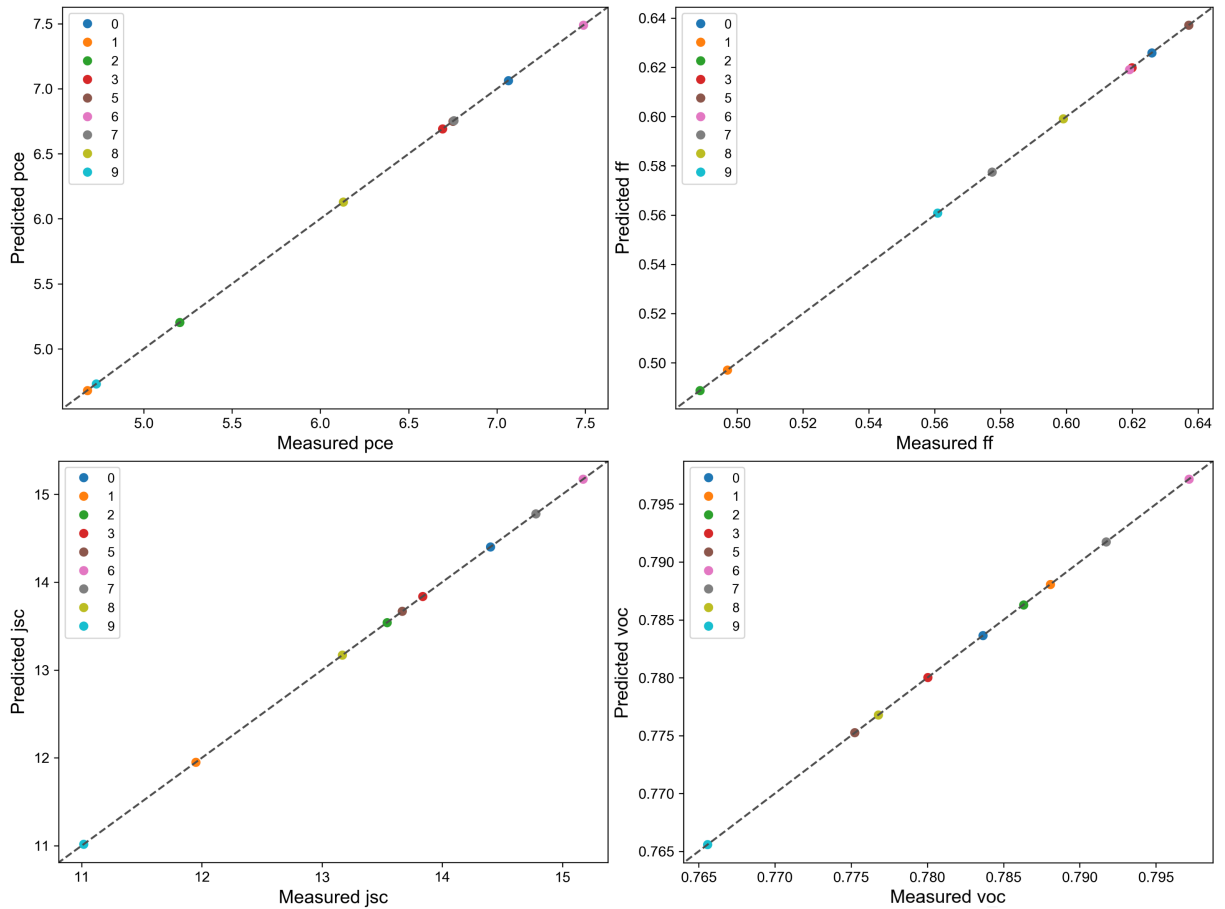


**Figure A.50:** ML-derived predictions of fit for the second round of DRCN5T/IT-4F BHJ blend optimization. Gamma (or compliance) values are reduced until a device deviates from the linear trendline. This gamma value represents the least accommodating fit that is capable of producing a topology that tracks to the experimental data.